7. Appendices

Publication No. 1

RESEARCH PAPER

Antibacterial Silver-Conjugated Magnetic Nanoparticles: Design, Synthesis and Bactericidal Effect

Anastasiia B. Shatan[1] · Kristýna Venclíková[1] · Beata A. Zasońska[1] · Vitalii Patsula[1] ·
Ognen Pop-Georgievski[1] · Eduard Petrovský[2] · Daniel Horák[1] (iD)

ABSTRACT

Purpose The aim was to design and thoroughly characterize monodisperse Fe_3O_4@SiO_2-Ag nanoparticles with strong antibacterial properties, which makes them a candidate for targeting bacterial infections.

Methods The monodisperse Fe_3O_4 nanoparticles were prepared by oleic acid-stabilized thermal decomposition of Fe(III) oleate; the particles were coated with silica shell using a water-in-oil reverse microemulsion, involving hydrolysis and condensation of tetramethyl orthosilicate. Resulting Fe_3O_4@SiO_2 particles were modified by (3-mercaptopropyl)trimethoxysilane to introduce 1.1 mmol SH/g. Finally, the Fe_3O_4@SiO_2-SH nanoparticles were decorated with silver nanoclusters formed by reduction of silver nitrate with $NaBH_4$. The particles were analyzed by FTIR, X-ray photoelectron and atomic absorption spectroscopy, dynamic light scattering and vibrating sample magnetometry. The antibacterial activity of the Fe_3O_4@SiO_2 and Fe_3O_4@SiO_2-Ag nanoparticles was tested against Gram-positive *Staphylococcus aureus* and Gram-negative *Escherichia coli* bacteria cultivated on Luria agar plates or in Luria broth.

Results The superparamagnetic Fe_3O_4@SiO_2-Ag nanoparticles (21 nm in diameter; saturation magnetization 26 A·m^2/kg) were successfully obtained and characterized. Inhibitory and toxic effects against bacteria were documented by incubation of the Fe_3O_4@SiO_2-Ag nanoparticles with *Staphylococcus aureus* and *Escherichia coli*.

Conclusions The combination of magnetic properties together with bactericidal effects is suitable for the disinfection of medical instruments, water purification, food packaging, etc.

ABBREVIATIONS

AAS	Atomic absorption spectrometer
Amp	Ampicillin
CFU	Colony forming units
Đ	Dispersity
D_h	Hydrodynamic diameter
DLS	Dynamic light scattering
D_n	Number-average diameter
DT	1-Dodecanethiol
D_w	Weight-average diameter
E. coli	*Escherichia coli*
Igepal CO-520	Polyoxyethylene(5) nonylphenylether
IS	Icosane
LA	Luria agar plates
LB	Luria broth
MPTMS	(3-Mercaptopropyl)trimethoxysilane
NT	No treatment controls
OA	Oleic acid
OD	Octadec-1-ene
PBS	Phosphate buffered saline
PI	Polydispersity index
S. aureus	*Staphylococcus aureus*
SAM	Self-assembled monolayer
SBH	Sodium borohydride
TEM	Transmission electron microscope
TMOS	Tetramethyl orthosilicate
XPS	X-ray photoelectron spectroscopy

✉ Daniel Horák
    horak@imc.cas.cz

[1] Institute of Macromolecular Chemistry
     Czech Academy of Sciences
     Heyrovského nám. 2, 162 06 Prague 6, Czech Republic

[2] Institute of Geophysics
     Czech Academy of Sciences
     Boční II/1401, 141 31 Prague 4, Czech Republic

INTRODUCTION

The emergence and dissemination of antibiotic-resistant pathogenic bacteria, which are associated with antibiotic abuse, on contaminated surfaces is becoming one of the major global public health threats, especially in hospitals, tissue engineering applications, etc. [1, 2]. Thus, there is a significant interest in the development of novel antimicrobial nanostructures to modify the surfaces of medical implants and other devices. Such agents should possess not only high antibacterial activity but also must be environmentally friendly, have relatively low general toxicity, and be easy to prepare [3].

There are several classes of antimicrobial materials, including polymers, inorganic/polymer nano- and microparticles, quaternary ammonium cationic surfactants (didodecyl dimethylammonium bromide), aminoglycosides, and antimicrobial peptides [4–7]. Nanoparticles, which can mimic biological protein inhibitors by matching their sizes, geometries, and surface chemistry, seem to be especially promising antimicrobial agents. They are exemplified by silver particles, which are exploited in medicine for biocidal therapy owing to their antifungal, antibacterial, anti-inflammatory, and antiviral properties [8–10]. Silver-containing compounds have been extensively used in electronics, cosmetics, materials in contact with food, water disinfectants, wound dressings, dental materials, and implants [11]. To incorporate silver in various systems, numerous approaches have been applied, such as wet chemical methods, thermal or plasma deposition, and green techniques using plants, bacteria, or fungi [12, 13].

Also magnetic nanoparticles, such as magnetite (Fe_3O_4) or maghemite (γ-Fe_2O_3), have received considerable attention due to their small size, large surface area, strong magnetic properties, and low toxicity [14, 15]. Their biggest advantage is their easy manipulability and targetability by a magnetic field, which substantially simplifies the separation of various biomolecules. However, uncoated iron oxide particles show a tendency to aggregate and have high nonspecific adsorption of proteins and cells. To avoid these shortcomings, surface modifications are necessary, such as the introduction of coating, grafting and/or encapsulation by various polymers, e.g., poly(methyl methacrylate), poly(vinyl alcohol), poly(ethylene glycol), or silica [16]. The latter is often used due to its noncytotoxicity, high chemical stability, reasonable price, simple synthesis, and ability to be easily modified with various functional groups [17, 18]. Even though magnetic

nanoparticles are known to exhibit some antibacterial activity damaging DNA, lipids, and proteins through the Fenton reaction [19, 20], it is important to boost microbicidal action to combat bacterial resistance. Therefore gentamicin was conjugated to iron oxide nanoparticles [21], and silver was coated on ethanediylbis(isonicotinate)-adsorbed carboxyl dextran-coated iron oxide [22], poly(acrylic acid)-coated iron oxide [23], magnetite [24], maghemite [25], poly(acrylic acid)/poly-acrylamide-coated magnetic COMPEL™ microspheres [26], etc. Also, a Fe_3O_4-SiO_2-Ag composite was prepared for water disinfection, however, Ag was not firmly bound to the particle surface [27].

The aim of this report was to design, prepare, and characterize biocompatible monodisperse silica-coated magnetite nanoparticles (Fe_3O_4@SiO_2) and to functionalize them with thiol groups to enable decoration with silver nanoclusters (Fig. 1). This new multifunctional colloid exhibited strong antibacterial properties, which makes it a candidate for targeting bacterial infections.

EXPERIMENTAL

Chemicals and Materials

Octadec-1-ene (OD), Igepal CO-520 [polyoxyethylene(5) nonylphenylether], tetramethyl orthosilicate (TMOS), (3-mercaptopropyl)trimethoxysilane (MPTMS), silver nitrate ($AgNO_3$; 99.8%), sodium borohydride (SBH; ≥98.0%), 1-dodecanethiol (DT), and phosphate buffered saline (PBS) were purchased from Sigma-Aldrich (St. Louis, MO, USA). Oleic acid (OA), ammonium fluoride, acetone, dichloromethane, and ethanol were obtained from Lachema (Brno, Czech Republic). Cellulose membrane (14 kDa) for dialysis was obtained from Spectrum Europe (Breda, Netherlands). Fe(III) oleate was prepared according to an earlier report [28]. All other chemicals were purchased from Sigma-Aldrich. Ultrapure Q-water ultrafiltered on a Milli-Q Gradient A10 system (Millipore; Molsheim, France) was used in the experiments.

Synthesis of Fe_3O_4 Nanoparticles

OA-stabilized Fe_3O_4 nanoparticles were obtained by thermal decomposition of Fe(III) oleate [28, 29]. Briefly, Fe(III) oleate
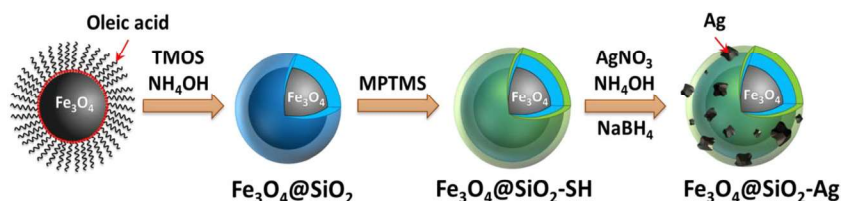

Fig. 1 Schematic preparation of Fe_3O_4@SiO_2-Ag nanoparticles. TMOS - tetramethyl orthosilicate (TMOS), MPTMS - (3-mercaptopropyl)trimethoxysilane.

(5.76 g; 8 mmol) was dissolved in a mixture of OD (40 ml) and OA (0.3 mmol/ml). The reaction mixture was preheated at 120°C for 60 min under nitrogen flow and was then heated at 320°C for 30 min. After cooling the mixture to room temperature (RT), ethanol (100 ml) was added to the reaction mixture, and the particles were separated by a magnet and washed with hot ethanol (60–70°C; 50 ml each) three times to remove residual solvents and OA. Finally, the Fe_3O_4 nanoparticles were dispersed in hexane and stored.

Synthesis of $Fe_3O_4@SiO_2$ and $Fe_3O_4@SiO_2$-SH Nanoparticles

$Fe_3O_4@SiO_2$ and $Fe_3O_4@SiO_2$-SH nanoparticles were obtained by the water-in-oil (w/o) reverse microemulsion technique [28, 30, 31]. To a dispersion of Fe_3O_4 (40 mg) in hexane (38.4 ml), Igepal CO-520 (2 ml) and 25% NH_4OH (0.32 ml) were added, and the mixture was sonicated at RT for 30 min (10% of power). After the addition of TMOS (0.04 ml), the reaction mixture was stirred (750 rpm) at RT for 48 h. To prepare $Fe_3O_4@SiO_2$-SH nanoparticles, MPTMS (0.02 ml) was added, and the reaction was continued at RT for additional 24 h.

Preparation of $Fe_3O_4@SiO_2$-Ag Nanoparticles

$Fe_3O_4@SiO_2$-SH colloid was sonicated for 3 min, and 1 M $AgNO_3$ aqueous solution (0.05 ml) and 3 M aqueous NH_3 (0.15 ml) were added dropwise at RT with stirring (750 rpm) while forming the $Ag(NH_3)_2^+$ complex. SBH aqueous solution (0.1 ml; 2 M) was then added dropwise, and the mixture was stirred for 1 h. The resulting $Fe_3O_4@SiO_2$-Ag nanoparticles were washed with ethanol and water five times each to remove residual surfactant and were finally stored at 4°C. Pristine silver nanoparticles, serving as a control, were prepared analogously, in the absence of $Fe_3O_4@SiO_2$-SH particles.

XPS Measurements and Preparation of Reference Samples

XPS measurements were performed using a K-Alpha$^+$ XPS spectrometer (ThermoFisher Scientific; East Greenstead, UK) operating at a base pressure of 1.0×10^{-7} Pa. Data acquisition and processing were performed using Thermo Avantage software. All particles were analyzed using a microfocused monochromated Al Kα X-ray radiation (400 μm spot size) with pass energy of 200 eV for survey and 50 eV for high-energy resolution core level spectra. The X-ray angle of incidence was 30° and the emission angle was normal to the surface. In the insulating samples, a K-Alpha charge dual compensation system was used with electrons and low-energy argon ions to prevent localized charge build-up. The analyzer transmission function, Scofield sensitivity factors, and

effective attenuation lengths (EALs) for photoelectrons were applied for quantification. EALs were calculated using the standard TPP-2 M formalism. The binding energy scale of the XPS spectrometer was calibrated by the well-known positions of the C—C and C—H, C—O and C(=O)—O peaks of poly(ethylene terephthalate) and Cu 2p, Ag 3d, and Au 4f peaks of metallic Cu, Ag and Au, respectively. All measured spectra were charge referenced to the C 1 s peak attributed to C—C, C—H at 285 eV binding energy. The high resolution spectra were fitted with Voigt profiles to probe the individual contributions of chemical species. The resulting binding energy uncertainty did not exceed ±0.1 eV. Reference determination of thiol binding to silver was performed on circular poly-crystalline silver metal plates (diameter ~1.2 cm), which were sonicated in ethanol and water, dried and exposed to UV ozone for 20 min. To prepare clean Ag surfaces without any surface impurities, the adventitious carbon contamination was sputtered away utilizing the MAGCIS cluster source, employing Ar^+ ion clusters composed of 75 atoms. The sputtering utilizing energy of 8000 eV per cluster proceeded for 25 min.

Additional planar Ag substrates were functionalized with DT self-assembled monolayer (SAM). Briefly, freshly activated plates were immersed in 1 mM DT ethanolic solution, and the self-assembly reaction proceeded at RT for 24 h in dark, the substrates were removed from the solution, sonicated in ethanol and water for 15 min to remove physisorbed deposits, and dried under vacuum. The resulting substrates were immediately transferred to the XPS chamber for the analysis.

Additional Physicochemical Characterization of the Nanoparticles

Particle size, morphology and size distribution were analyzed on a Tecnai G2 Spirit Twin 12 transmission electron microscope (TEM; FEI; Brno, Czech Republic). Number-average diameter (D_n), weight-average diameter (D_w) and dispersity ($Đ$) were calculated from at least 400 individual particles from the TEM micrographs using Atlas software (Tescan, Brno, Czech Republic) as follows from Eq. 1–3:

$$D_n = \frac{\sum(n_i . D_i)}{\sum n_i} \tag{1}$$

$$D_w = \frac{\sum\left(n_i . D_i^4\right)}{\sum\left(n_i . D_i^3\right)} \tag{2}$$

$$Đ = \frac{D_w}{D_n} \tag{3}$$

where n_i and D_i are the number and diameter of the nanoparticles, respectively.

Hydrodynamic diameter D_h and polydispersity index PI (characterizing size distribution) of the nanoparticle dispersions were measured at 25°C by dynamic light scattering (DLS) using a ZEN3600 Nano-ZS Zetasizer (Malvern Instruments; Malvern, UK). Starting Fe_3O_4 nanoparticles were measured in hexane, while surface-modified particles in water (0.1 mg/ml; pH 6.4).

Elemental analysis was performed using a Perkin-Elmer 2400 CHN elemental analyzer (Waltham, MA, USA).

ATR FTIR spectra were recorded on a PerkinElmer Paragon 1000PC spectrometer using a Specac MKII Golden Gate single attenuated total reflection (ATR) system with a diamond crystal; the angle of incidence was 45°.

A PerkinElmer 3110 atomic absorption spectrometer (AAS) was used to analyze the amount of iron and silver in the particles by measuring the solution obtained after their mineralization with 68% $HClO_4$/65% HNO_3 (4:1) mixture at 80°C for 20 min.

The magnetization, which was mass-normalized, was measured using an EV9 vibrating sample magnetometer (DSM Magnetics ADE; Lowell, MA, USA) at RT. Data between ±0.6 T were processed, linear fit was applied to the section above 0.4 T and was subtracted from the measured data.

Antibacterial Activity of $Fe_3O_4@SiO_2$ and $Fe_3O_4@SiO_2$-Ag Nanoparticles

The antibacterial activity of $Fe_3O_4@SiO_2$ and $Fe_3O_4@SiO_2$-Ag nanoparticles was tested against Gram-positive *Staphylococcus (S.) aureus* (clinical isolate) and Gram-negative *Escherichia (E.) coli* BL21 bacteria (kindly provided by Dr. Karel Holada, First Faculty of Medicine, Charles University, Prague, Czech Republic) cultivated on Luria agar plates (LA) or in Luria broth (LB) (Sigma Aldrich) at 37°C.

Colony Counting on Luria Agar Plates (LA)

Overnight cultures of *S. aureus* and *E. coli* were resuspended in PBS and diluted in 2 ml of LB to $1\cdot10^7$ CFU/ml. $Fe_3O_4@SiO_2$ and $Fe_3O_4@SiO_2$-Ag nanoparticles (12.5, 25, and 50 μg/ml) were added to the cultures in six-well plates (TPP; Trasadingen, Switzerland) and were incubated at 37°C on a shaker (125 rpm); the particle concentrations were selected according to earlier published reports [32, 33]. Cultures without the nanoparticles were used as no treatment controls (NT). Aliquots were taken from the wells after 0, 30, 60, and 90 min to determine the bactericidal effect, i.e., the time required for the cell wall disruption leading to bacterial death. The suspensions were diluted to 10^{-4} for both *S. aureus* and *E. coli*, seeded on LA plates, and incubated at 37°C for 24 h. Bacterial colonies were counted and colony forming units (CFU/ml) were determined. The results were calculated as a ratio of the number of living bacteria at given time point to the number of living bacteria at time point 0. The procedure was repeated in three independent experiments in duplicates.

Nanoparticle Coincubation with Bacterial Cultures in LB

Overnight cultures of *S. aureus* and *E. coli* were resuspended in PBS and diluted in 1 ml of LB broth to $1\cdot10^5$ CFU/ml; this number of bacteria was selected to prevent their overgrowth, which would induce metabolite accumulation and false positive inhibition of growth. The particles (serial dilution starting at 500 μg/ml) were added to the cultures and incubated at 37°C for 24 h on a shaker (125 rpm). Cultures without the nanoparticles were used as no treatment controls (NT). Cultures with ampicillin (150 μg/ml) were used as positive control. Sample turbidity was measured on a Synergy H1 Hybrid Reader (Biotek; Highland Park, VT, USA) at 600 nm, and bacterial growth was evaluated by calculating viability (%) compared to NT control. The procedure was repeated in three independent experiments in duplicates. Statistical analysis was conducted using GraphPad Prism5 software and one-way ANOVA test with Dunnett's Multiple Comparison Post Test; the level of $P < 0.05$ was considered significant.

RESULTS AND DISCUSSION

Magnetic Fe_3O_4 Nanoparticles

Iron oxide particles (Fe_3O_4) were obtained by the OA-stabilized thermal decomposition of Fe(III) oleate. The big advantage of this technique is that it allows preparation of monodisperse magnetic nanoparticles of the same physico-chemical and biological properties; moreover, the particles have high crystallinity and controlled size. Generally, the size of nanoparticles can be regulated by changing the synthesis conditions, such as reaction time and temperature, which is typically controlled by using different nonpolar high-boiling organic solvents, such as octadec-1-ene (OD) or icosane (IS) [28]. In OD, smaller particles were produced than in IS, since the former solvent had a lower boiling temperature then the latter one. Similarly, a shorter reaction time resulted in smaller particles. The size of iron oxide nanoparticles governs their magnetic properties. Particles <20 nm exhibited superparamagnetic properties at room temperature due to thermally induced spin flipping [34], which makes them colloidally stable and allows them to avoid magnetically driven aggregation, in contrast to ferro- and ferrimagnetic particles.

In this report, 16-nm superparamagnetic nanoparticles were selected for preparation of the magnetically driven antibacterial particles (Table I) because if modified with silica, they can be well-internalized by the cells [29]. According to the TEM micrograph, the Fe_3O_4 particles had spherical

**Table I** Physicochemical characterization of the iron oxide nanoparticles.

Particles	D_n (nm)	Đ	D_h (nm)	PI	Elements (wt.%)			M_s (A·m²/kg)
					S	Fe	Ag	
Fe_3O_4	16	1.01	24[a]	0.01	–	69.9	–	44.2
$Fe_3O_4@SiO_2$	21	1.02	191	0.25	–	56.2	–	35.5
$Fe_3O_4@SiO_2$-SH	21	1.04	210	0.14	3.6	55.3	–	32.0
$Fe_3O_4@SiO_2$-Ag	21	1.05	239	0.16	2.3	42.7	2.3	26.3

D_n number average particle diameter (TEM); Đ dispersity (TEM); D_h hydrodynamic diameter (DLS); [a] measured in hexane, PI polydispersity index (DLS); M_s magnetic saturation

morphology (Fig. 2a). The particles were monodisperse with dispersity $D < 1.05$ due to the combination of a short nucleation time and the presence of the stabilizer, which prevents nuclei aggregation and ensures uniform conditions for each particle growth [29]. The hydrodynamic diameter of the nanoparticles in hexane was slightly larger ($D_h = 24$ nm) than D_n due to the OA stabilizer adsorbed on the particle surface, which was not visible in the TEM micrographs. Additionally, the polydispersity index ($PI = 0.01$) documented a very narrow particle size distribution. The presence of OA on the

Fe_3O_4 nanoparticles was also confirmed by ATR FTIR spectroscopy (Fig. 3). The characteristic bands corresponding to asymmetric and symmetric CH_2 stretching vibrations were observed at 2920 and 2850 cm^{-1}, respectively, and the bands at 562 cm^{-1} were attributed to the Fe–O vibrations.

XPS was used to probe the chemical composition of the Fe_3O_4 nanoparticles (Table II). The high resolution core level Fe 2p spectrum showed the characteristic Fe_3O_4 contributions, indicating the presence of 41.3 wt.% of Fe. This content was lower than the amount obtained from AAS (69.9 wt.%;

Fig. 2 TEM micrographs of (**a**) Fe_3O_4, (**b**) $Fe_3O_4@SiO_2$, (**c**) $Fe_3O_4@SiO_2$-SH, and (**d**) $Fe_3O_4@SiO_2$-Ag nanoparticles.
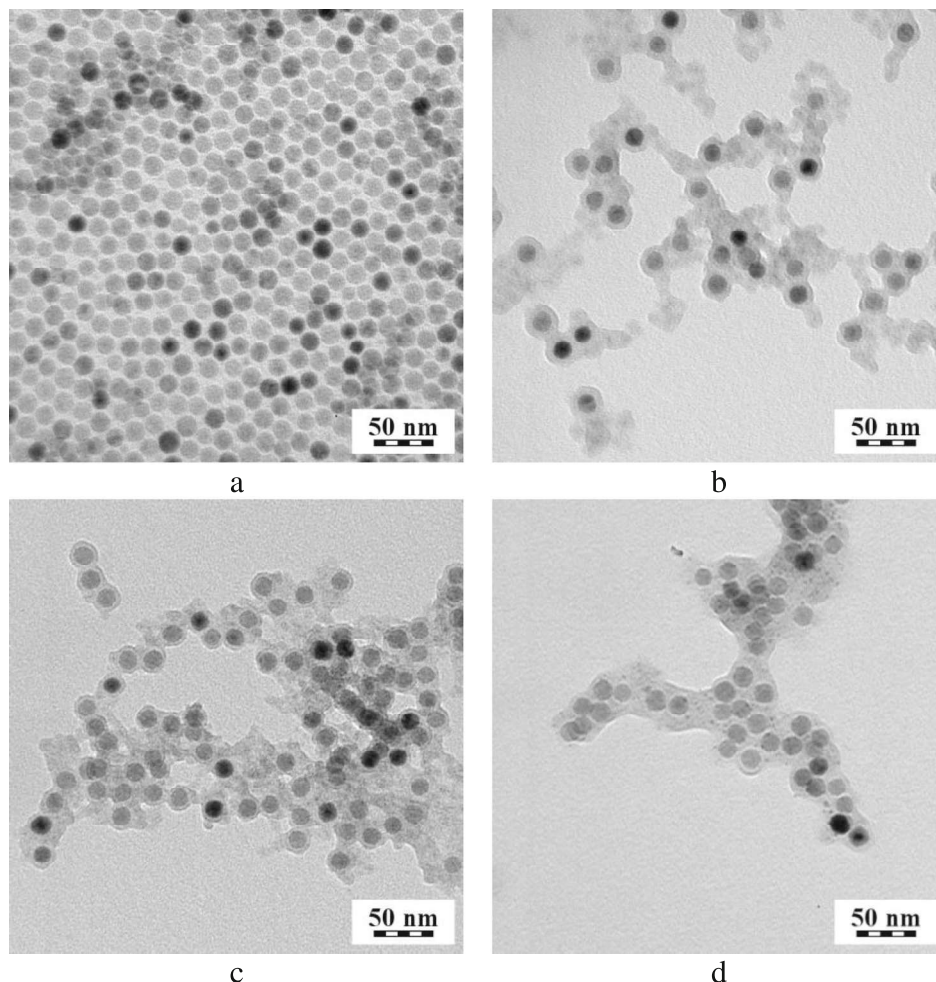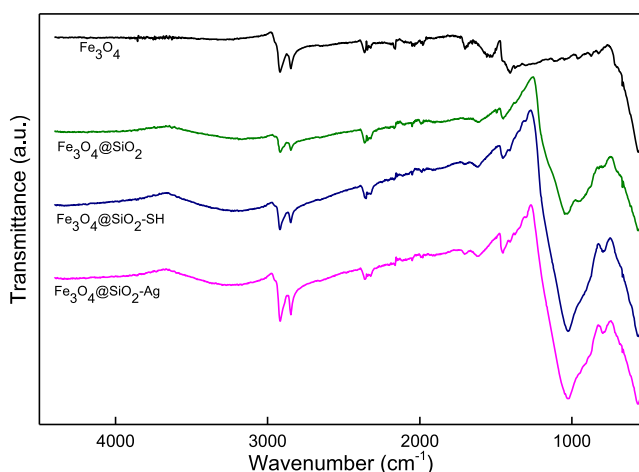
Fig. 3 FTIR spectra of Fe_3O_4, $Fe_3O_4@SiO_2$, $Fe_3O_4@SiO_2$-SH, and $Fe_3O_4@SiO_2$-Ag nanoparticles.

Table I), because nanoparticles were coated with oleic acid (chain length ~2 nm) [35] and XPS is a surface method that analyzes up to an 8-nm thick layer of the sample.

The higher contribution of organic shell, thus, led to the lower overall Fe content on the particle surface as determined by XPS. The amount of oleate shell determined from AAS was 4 wt.%, assuming that pure magnetite has 72.4 wt.% of Fe. Fe_3O_4 particles exhibited saturation magnetization $M_s = 44.2$ A·m^2/kg (Table I). With the exclusion of the contribution of the diamagnetic oleate shell, the M_s would reach 46 A·m^2/kg, which is significantly less than the saturation magnetization of bulk Fe_3O_4 ($M_s = 92$ A·m^2/kg) [36] but is comparable with reported values [37]. The difference could result from very small particle diameter, as it is well-known that saturation magnetization decreases with particle size reduction, which is explained by increased thermal fluctuation and a magnetically disordered surface that, in turn, results from increased surface-to-volume ratio [38, 39]. Magnetic measurements of the Fe_3O_4 nanoparticles did not reveal any hysteresis loop (Fig. 4). Zero coercivity confirmed the superparamagnetic behavior of the particles, which do not interact with each other.

Functional Silica-Modified Magnetic Nanoparticles

One disadvantage of the thermal decomposition method is that it provides hydrophobic Fe_3O_4 nanoparticles and hinders

their application in biology and medicine. Therefore, they have to be transferred to aqueous medium, typically by the ligand exchange technique [29]. In this report, the Fe_3O_4 particle surface was modified with hydrophilic silica (SiO_2) shell to achieve good colloidal stability in the biological media. Silica was introduced on the particles by the water-in-hexane reverse microemulsion technique involving hydrolysis and condensation of TMOS inside reverse micelles under basic catalysis; the colloid was stabilized by Igepal CO-520 surfactant (Fig. 1). The rather low TMOS-to-particle weight ratio enabled the production of core-shell nanoparticles with $D_n = 21$ nm and a thin (~3 nm) silica shell, the presence of which was clearly seen on the TEM micrograph (Fig. 2b). After the coating, the hydrodynamic particle size was large ($D_h = 191$ nm) due to the presence of silica shell and to particle clustering in water. Additionally, the FTIR spectrum of the $Fe_3O_4@SiO_2$ particles confirmed the presence of the silica on the Fe_3O_4 surface, as documented by intensive bands at 1080 and 3200 cm^{-1} attributed to the vibrations of Si–O–Si and -OH groups, respectively (Fig. 3). Moreover, the presence of silica on the $Fe_3O_4@SiO_2$ particles was proved by the XPS analysis (Table II). The amount of Fe dropped from 44.7 wt.% for the unmodified Fe_3O_4 nanoparticles to 14.5 wt.% for the $Fe_3O_4@SiO_2$ particles, which was less than that according to the magnetic measurement (27.9 wt.%). M_s of $Fe_3O_4@SiO_2$ decreased to 35.5 A·m^2/kg due to the contribution of the SiO_2 shell, which corresponds to 38.6 wt.% of Fe_3O_4. The lower amount of Fe from XPS compared to the magnetic measurement is not surprising, as the former method is a surface-sensitive technique, measuring only ~8-nm depth; as mentioned above, $Fe_3O_4@SiO_2$ particles consisted of ~3 nm silica shell and Fe_3O_4 core.

MPTMS was used to introduce thiol groups on the particle surface to prospectively affix silver (Fig. 1). Their presence was confirmed by elemental analysis, which found 3.6 wt.% of sulfur; D_h increased to 210 nm (Table I). Due to the relatively low thiol content, the corresponding band in the ATR FTIR spectrum was not distinguishable (Fig. 3). However, the presence of the SH groups on the $Fe_3O_4@SiO_2$-SH particles was documented by the XPS analysis (Fig. 5; Table II). The amount of Fe dropped from 14.5 wt.% on the $Fe_3O_4@SiO_2$ nanoparticles to 12.0 wt.% on the $Fe_3O_4@SiO_2$-SH particles, which was attributed to the formation of the second thiol-

Table II Chemical composition of the iron oxide nanoparticles determined by XPS analysis.

Particles	C 1 s (wt.%)	O 1 s	Fe 2p	Si 2p	S 2p SH	S 2p S-Ag	Ag 3d
Fe_3O_4	12.3	46.4	41.3	–[a]	–	–	–
$Fe_3O_4@SiO_2$	19.0	44.7	14.5	21.8	–	–	–
$Fe_3O_4@SiO_2$-SH	19.7	40.0	12.0	23.7	4.7	–	–
$Fe_3O_4@SiO_2$-Ag	32.3	28.9	6.4	18.9	2.9	1.3	9.3

[a] Below the detection limit of the XPS measurement
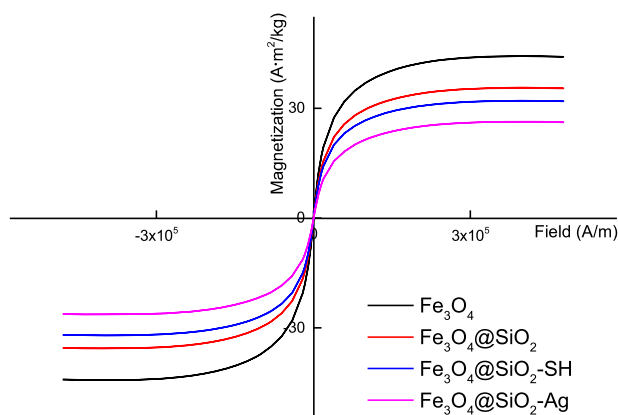
Fig. 4 Magnetization curves of Fe₃O₄, Fe₃O₄@SiO₂, Fe₃O₄@SiO₂-SH, and Fe₃O₄@SiO₂-Ag nanoparticles corrected for para- and diamagnetic contributions.

containing silica layer after the addition of MPTMS in the sol-gel process. According to the magnetization measurement of the Fe₃O₄@SiO₂-SH particles, their $M_s = 32$ A·m^2/kg, which corresponded to 25.2 wt.% of Fe (34.8 wt.% of Fe₃O₄). In the Si 2p XPS spectra of the Fe₃O₄@SiO₂ and Fe₃O₄@SiO₂-SH nanoparticles, the formation of SiO₂ and reactive thiol-containing shells around the Fe₃O₄ nanoparticles resulted in increased silicon contributions at ~103 eV. Successful incorporation of thiol groups on the Fe₃O₄@SiO₂ particle surface
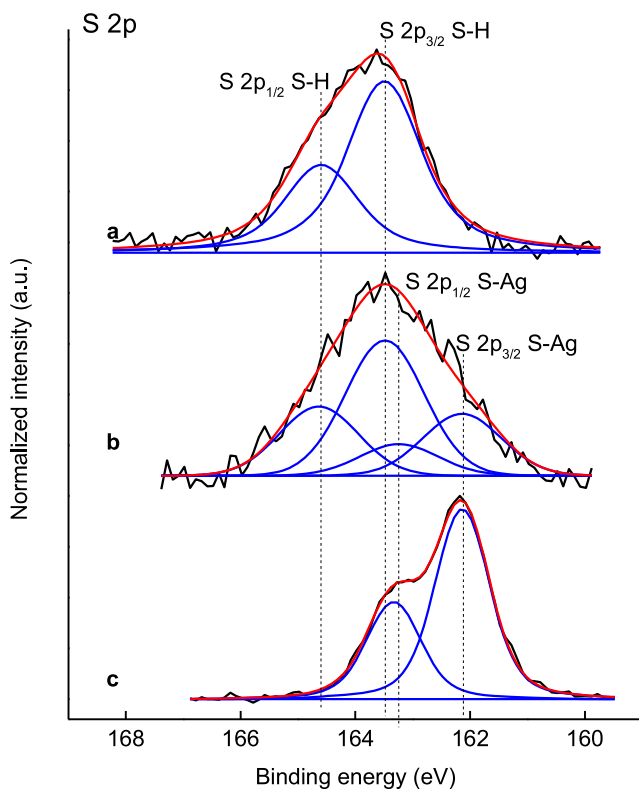
Fig. 5 High resolution core level S 2p XPS spectra of (**a**) Fe₃O₄@SiO₂-SH, (**b**) Fe₃O₄@SiO₂-Ag, and (**c**) reference DT SAM on a silver substrate. Spectra are presented with black lines, and the resulting fitted envelopes with red lines. The individual contributions of the fitted curve are presented with blue lines.

was further verified the by the appearance of 4.7 wt.% of SH at 163.5 eV (spin split $2p_{3/2}$–$2p_{1/2}$ doublet, separation of 1.3 eV) in the core level S 2p high resolution spectrum (Fig. 5; Table II).

Silver-Modified Fe₃O₄@SiO₂-SH Nanoparticles

After precipitation of AgNO₃ with SBH in the presence of Fe₃O₄@SiO₂-SH nanoparticles, silver nanoclusters were attached to their surface (Fig. 1). The diameter of Fe₃O₄@SiO₂-Ag nanoparticles ($D_n = 22$ nm) remained unchanged compared to silica-modified magnetic particles. DLS was used to determine the hydrodynamic particle size, which increased to 239 nm compared to the Fe₃O₄@SiO₂-SH particles. The difference between D_h values and diameters calculated from TEM micrographs (D_n) is expected and is obtained because direct measurement on TEM provides number-average diameters of dried particles (D_n), while DLS yields intensity average diameters of hydrated particles (D_h), which overestimates bigger particles and thus is sensitive to aggregates.

In ATR FTIR spectrum of the Fe₃O₄@SiO₂-Ag nanoparticles, no changes were detected compared to the spectrum of the Fe₃O₄@SiO₂ due to the detection limits of the ATR technique. However, XPS analysis demonstrated decoration of the Fe₃O₄@SiO₂-SH nanoparticles with silver. The amount of Fe decreased to 6.4 wt.% Fe on the Fe₃O₄@SiO₂-Ag nanoparticles due to the introduction of silica shell and silver. The incorporation of silver on the Fe₃O₄@SiO₂-SH nanoparticle surface decreased the free thiol group content to 2.9 wt.%. Moreover, 1.3 wt.% of S-Ag species appeared at ~162.1 eV in the high resolution core level S 2p XPS spectrum (Fig. 5; Table II). The peak position was verified on planar Ag substrate modified with DT SAM. Concomitantly, characteristic $3d_{5/2}$ and $3d_{3/2}$ spin split contributions of silver were observed in the high resolution Ag 3d spectrum of the Fe₃O₄@SiO₂-Ag nanoparticles at ~368.9 eV (Fig. 6). While the full width at half maximum (FWHM) of the spectra measured on monolithic silver metal plates and nanoparticles under the same conditions showed values <1 eV, the spectrum of Fe₃O₄@SiO₂-Ag nanoparticles showed a FWHM of ~1.6 eV. At the same time, the covalent binding of DT to the silver plate induced an ~0.4 eV shift of the Ag peak. The broadening of Ag peaks in the spectrum of the Fe₃O₄@SiO₂-Ag nanoparticles and the shift in the binding energy with respect to the pristine nonmodified silver nanoparticles suggested the presence of Ag⁰ and Ag¹⁺. The combination of Ag 3d and S 2p spectra of Fe₃O₄@SiO₂-Ag nanoparticles indicated the presence of ~4.5 wt.% Ag⁰ and 4.8 wt.% Ag¹⁺.

Compared to the Fe₃O₄ and Fe₃O₄@SiO₂ particles, the saturation magnetization of the Fe₃O₄@SiO₂-Ag decreased to 26.3 A·m^2/kg, reflecting the presence of diamagnetic silver on the particle surface; the amount of Fe₃O₄ was, thus,
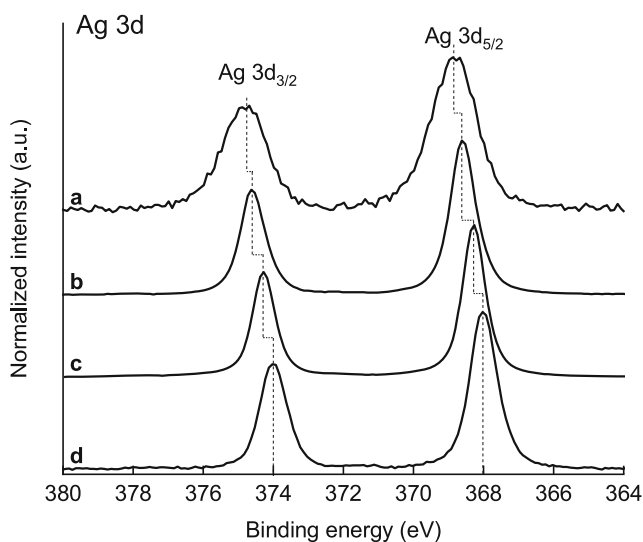
Fig. 6 (**a**) High resolution core level Ag 3d XPS spectrum of Fe₃O₄@SiO₂-Ag nanoparticles. Reference spectra of (**b**) DT SAM on Ag, (**c**) bare Ag substrate, and (**d**) Ag nanoparticles are reported for comparison.

calculated to be 28.6 wt.%, i.e., the amount of silver can be estimated to ~6 wt.%. Superparamagnetic behavior was not affected by this additional coating.

In Vitro Determination of Antibacterial Properties of Fe₃O₄@SiO₂-Ag Nanoparticles

Among different types of nanoparticles, such as ZnO, NiO, Al₂O₃, CuO, TiO₂, and Ag, used against *E. coli*, *B. subtili*, and *S. aureus*, the silver nanoparticles (<5 nm) are especially known to exhibit strong antibacterial properties [40]. Although the exact mechanism of the antimicrobial effect of silver is unknown, one of the possible impacts is induced by the accumulation of the nanoparticles on the cell surface and the formation of pits, leading to bacterial death [41]. Silver nanoparticles in contact with the bacterial surface can also produce free radicals, causing oxidative stress and subsequent membrane damage [42, 43]. Silver ions released from the nanoparticles can impair the activity of vital bacterial enzymes and can also

cause the loss of the replication ability of bacterial DNA [44, 45]. The antimicrobial activity of silver nanoparticles depends on their concentration, exposure time, charge and morphology, and, in particular, on their size and shape. Positively charged nanoparticles are considered to be more effective against both Gram-positive and negative bacterial species than the negatively charged ones [46]. In terms of the morphology, triangular silver nanoplates and/or 10–12-nm particles are more efficient than spherical or rod-like particles and/or larger particles due to higher surface area [47, 48]. To determine the antimicrobial activity of the monodisperse Fe₃O₄@SiO₂-Ag nanoparticles developed in this study, two experimental conditions were established. In both settings, Fe₃O₄@SiO₂ nanoparticles and NT served as a control.

First, bacterial colonies were incubated with the nanoparticles and counted on agar plates. Figure 7 shows selected LB agar plates with both *S. aureus* and *E. coli* after incubation for 0, 30, 60, and 90 min with 50 μg of Fe₃O₄@SiO₂-Ag particles per ml. Neither Fe₃O₄@SiO₂ or Fe₃O₄@SiO₂-Ag nanoparticles showed an antibacterial effect against *E. coli* (Fig. 8 a, b). Fe₃O₄@SiO₂-Ag nanoparticles decreased the number of viable *S. aureus* cells (Fig. 8 c, d), but due to the high standard deviation no significant antimicrobial effect was detected. When comparing the antibacterial activity of both Fe₃O₄@SiO₂ and Fe₃O₄@SiO₂-Ag nanoparticles in the presence of *S. aureus* up to 90 min, significant decrease of its viability was detected after 30 and 60 min of incubation at a concentration of 50 μg/ml ($P < 0.05$ and $P < 0.01$, respectively) and after 90 min at a concentration of 25 μg/ml ($P < 0.05$). The inhibition of bacterial growth strongly depended on the number of cells used in the experiment and on the concentration of silver ions. The antibacterial nanoparticle efficiency increased with decreasing number of bacterial cells seeded at the beginning [41, 48].

Second, bacterial liquid culture was incubated with a serial dilution of nanoparticles, starting at 500 μg/ml, at 37°C for 24 h and bacterial growth was evaluated by measuring culture turbidity. Untreated cells and cells treated with ampicillin were used as controls. No significant growth inhibition of

Fig. 7 Agar plates on Petri dishes with (**a-d**) *S. aureus* and (**e-h**) *E. coli* suspension after (**a, e**) 0, (**b, f**) 30, (**c, g**) 60, and (**d, h**) 90 min of incubation with Fe₃O₄@SiO₂-Ag nanoparticles (50 μg/ml).
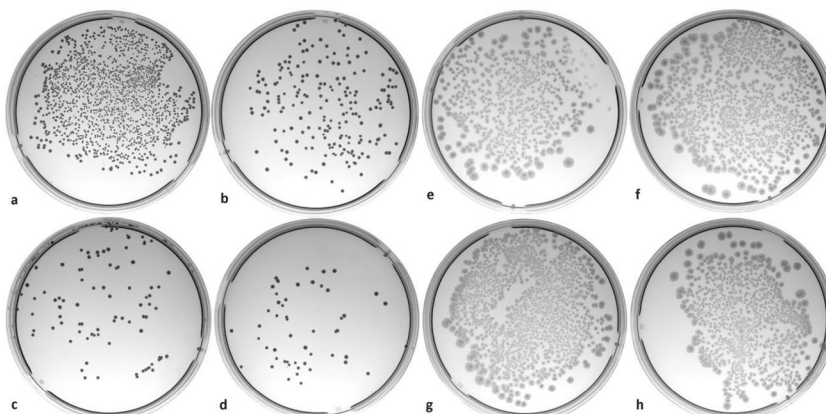
Fig. 8 (**a, b**) *E. coli* and (**c, d**) *S. aureus* colony counting on Luria agar plates after incubation with (**a, c**) Fe₃O₄@SiO₂-Ag and (**b, d**) Fe₃O₄@SiO₂ nanoparticles. Particle concentrations: 12.5 µg/ml (green), 25 µg/ml (blue), and 50 µg/ml (red). Error bars were calculated as standard deviation.
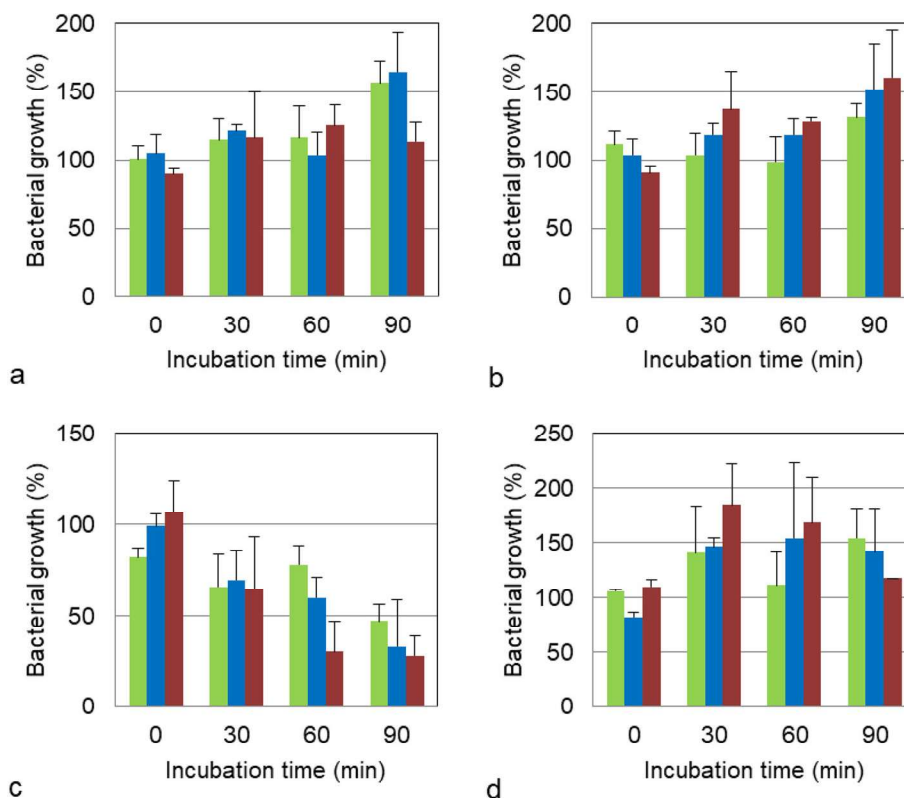
E. coli or *S. aureus* was detected after incubation with Fe_3O_4@SiO_2 particles. *E. coli* growth was significantly inhibited after incubation with the Fe_3O_4@SiO_2-Ag nanoparticles at concentrations of 500 and 250 µg/ml, and the bacteria viability dropped to 60.5 and 83.2%, respectively (Fig. 9 a, $P < 0.001$). *S. aureus* viability was significantly affected untill reaching a concentration of 31.25 µg of Fe_3O_4@SiO_2-Ag/ ml (Fig. 9 b). The viability decreased to 73.1, 76.4, 80.7, 84.1 ($P < 0.001$) and 87.9% ($P < 0.005$) with particle concentration varying from 500, to 250, 125, 62.5, and 31.3 µg/ml, respectively. This result is in agreement with previous studies implying significant *E. coli* growth inhibition can be induced by silver nanoparticles, but only mild *S. aureus* growth inhibition is found; moreover, free radical generation was accompanied by subsequent membrane damage of Gram-negative *E. coli* [42]. Inhibition of *E. coli* growth with silver nanoparticles that accumulated both on the bacteria surface and inside the cells was also reported [41].

There is still no satisfactory explanation for how nanoparticles cross the bacterial cell wall. The cell wall of Gram-negative bacteria is composed of lipopolysaccharides, lipoproteins, and phospholipids, which form a penetration barrier that allows the entrance of only macromolecules [4]. In contrast, the cell wall of Gram-positive bacteria includes a thick layer of peptidoglycan as well as teichoic acid and abundant pores that allow foreign molecules to penetrate, resulting in cell membrane damage and cell death [4]. It was suggested that 1–9 nm particles can be transported through porins and

can therefore influence bacterial metabolism (e.g., oxidative stress) [49]. Our 21-nm particles probably could not rapidly enter the bacterial cell, and the accumulation of particles on the bacterial surface caused cell wall disruption with subsequent infiltration of particles into the cytoplasm. It should be also noted that the Ag nanoparticles can induce toxicity in humans, athouth its mechanisms are still not understood. Extended exposure to Ag through oral administration and inhalation can lead to Argyria or Argyrosis, i.e., chronic disorders of skin microvessels and eyes in humans. *In vivo* rodent studies then revealed toxic effects of Ag particles by their accumulating in the liver, spleen, and lungs [50]. Some researchers proved toxic effect of Ag nanoparticles *in vitro* on cell cultures; e.g., at 3.125 µg/ml for SH-SY5Y after 48 h, at 20 µg/ml for HEK293T after 24 h, or at 10 µg/ml for HepG2 and Caco2 cells after 24 h [51–53].

CONCLUSIONS

Systems delivering an active agent to the target site, such as antibacterial/magnetic bifunctional nanoparticles, reduce side effects. Moreover, these particles can also be separated and recovered after completion of the antibacterial action by the aid of a magnet. Here, silver-conjugated superparamagnetic Fe_3O_4 nanoparticles with antibacterial properties superior to those of neat iron oxides were designed and prepared using a simple, effective, and rapid method to specifically target

Fig. 9 Inhibition of (**a**) *E. coli* and (**b**) *S. aureus* bacterial growth after 24-h incubation in liquid LB. **P < 0.005, *** P < 0.001; $Fe_3O_4@SiO_2$-Ag (blue), $Fe_3O_4@SiO_2$ (green), and Amp – ampicillin (positive control). Error bars were calculated as standard deviation.
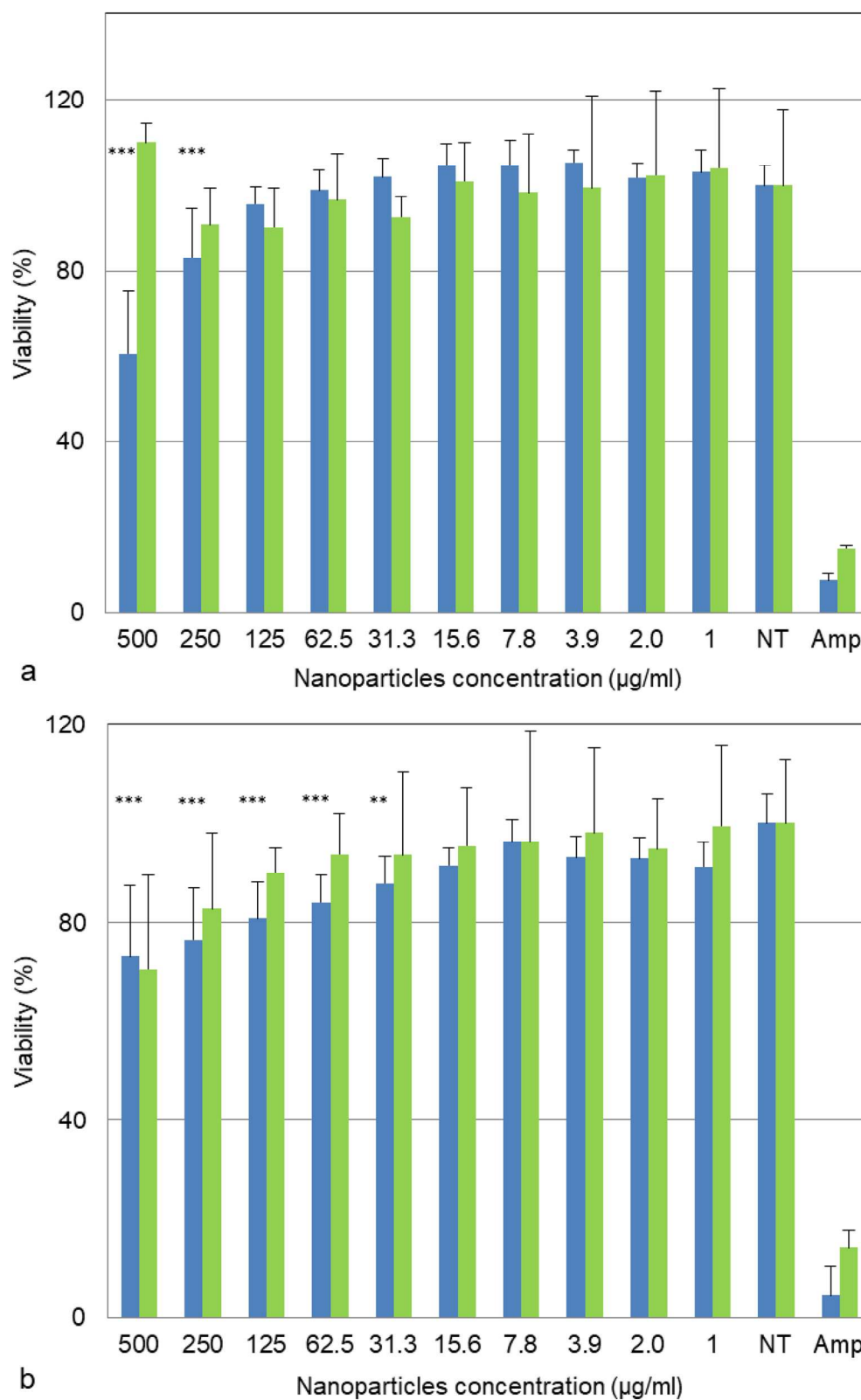
bacteria *in vivo*, which can potentially solve the resistance of pathogens against antibiotics. A key role is played by the surface characteristics of the particles in terms of their good dispersibility and colloidal stability in physiological media, their biocompatibility, and the presence of reactive groups for prospective attachment of biocides, such as silver. The surface of the magnetic iron oxide nanoparticles was modified with silica containing thiol groups by condensation of MPTMS, which

enabled the introduction of silver nanoclusters, exhibiting antibacterial properties. To the best of our knowledge, formation of silver on mercaptosilane-modified magnetite nanoparticles has not been described before. The inhibitory and toxic effects against bacteria were documented by incubation of the $Fe_3O_4@SiO_2$-Ag nanoparticles with *S. aureus* and *E. coli*. $Fe_3O_4@SiO_2$-Ag particles at low concentrations showed a direct bactericidal effect on *S. aureus*, while the viability of *E. coli* remained unaffected. After the bacteria were incubated with high $Fe_3O_4@SiO_2$-Ag concentrations, a strong effect on *E. coli* was detected. *S. aureus* growth was mildly inhibited with an even lower $Fe_3O_4@SiO_2$-Ag concentration. The combination of Ag with magnetic nanoparticles enabled easy separation of the Ag disinfectant from water and enabled repeated use. The nanoparticles, combining both magnetic separation or targetability and biocidal activity in a single entity, can potentially be used for new biological applications in the disinfection of hygienic areas, for example, when disinfecting wastewater or in the treatment of antibiotic-resistant pathogenic bacteria, which, by indirect transmission through contaminated surfaces and medical devices, are becoming a major global public health threat.

ACKNOWLEDGMENTS AND DISCLOSURES

REFERENCES

1. Spellberg B, Guidos R, Gilbert D, Bradley J, Boucher HW, Scheld WM, et al. The epidemic of antibiotic-resistant infections: a call to action for the medical community from the Infectious Diseases Society of America. Clin Infect Dis. 2008;46:155–64.
2. Roca I, Akova M, Baquero F, Carlet J, Cavaleri M, Coenen S, et al. The global threat of antimicrobial resistance: science for intervention. New Microbes New Infect. 2015;16:22–9.
3. Lam SJ, Wong EHH, Boyer C, Qiao GQ. Antimicrobial polymeric nanoparticles. Prog Polym Sci. 2018;76:40–64.
4. Wang L, Hu C, Shao L. The antimicrobial activity of nanoparticles: present situation and prospects for the future. Int J Nanomedicine. 2017;12:1227–49.
5. Jennings MC, Minbiole KPC, Wuest WM. Quaternary ammonium compounds: an antimicrobial mainstay and platform for innovation to address bacterial resistance. ACS Infect Dis. 2015;1:288–303.
6. Kim J, Pitts B, Stewart PS, Camper A, Yoon J. Comparison of the antimicrobial effects of chlorine, silver ion, and tobramycin on biofilm. Antimicrob Agents Chemother. 2008;52:1446–53.
7. Draper LA, Cotter PD, Hill C, Ross RP. Lantibiotic resistance. Microbiol Mol Biol Rev. 2015;79:171–91.
8. Clement JL, Jarrett PS. Antibacterial silver. Met Based Drugs. 1994;1:467–82.
9. Kędziora A, Speruda M, Krzyżewska E, Rybka J, Łukowiak A, Bugla-Płoskońska G. Similarities and differences between silver ions and silver in nanoforms as antibacterial agents. Int J Mol Sci. 2018;19:444.
10. Radtsig MA, Koksharova OA, Khmel IA. Antibacterial effects of silver ions: effect on gram-negative bacteria growth and biofilm formation. Mol Genet Microbiol Virol. 2009;4:194–9.
11. Gao SS, Zhao IS, Duffin S, Duangthip D, Lo ECM, Chu CH. Revitalising silver nitrate for caries management. Int J Environ Res Public Health. 2018;15:80.
12. Sun Y, Xia Y. Shape-controlled synthesis of gold and silver nanoparticles. Science. 2002;298:2176–9.
13. Panacek A, Kvítek L, Prucek R, Kolar M, Vecerova R, Pizúrova N, et al. Silver colloid nanoparticles: synthesis, characterization, and their antibacterial activity. J Phys Chem B. 2006;110:16248–53.
14. Cornell RM, Schwertmann U. The Iron oxides: structure, properties, reactions, occurrences and uses. second ed. Darmstadt, Germany: Wiley; 2000.
15. Laurent S, Forge D, Port M, Roch A, Robic C, van der Elst L, et al. Magnetic iron oxide nanoparticles: synthesis, stabilization, vectorization, physicochemical characterizations, and biological applications. Chem Rev. 2008;108:2064–110.
16. Chaudhuri GR, Paria S. Core/shell nanoparticles: classes, properties, synthesis mechanisms, characterization, and applications. Chem Rev. 2012;11:2373–433.
17. Bergna HE, Roberts WO. Colloidal silica: fundamentals and applications. Santa Barbara, USA: CRC Press; 2005.
18. Stöber W, Fink A. Controlled growth of monodisperse silica spheres in the micron size range. J Colloid Interface Sci. 1968;26:62–9.
19. Prabhu YT, Rao KV, Kumari BS, Kumar VSS, Pavani T. Synthesis of Fe_3O_4 nanoparticles and its antibacterial application. Int Nano Lett. 2015;5:85–92.
20. Ismail RA, Sulaiman GM, Abdulrahman SA, Marzoog TR. Antibacterial activity of magnetic iron oxide nanoparticles synthesized by laser ablation in liquid. Mater Sci Eng C. 2015;53:286–97.
21. Bhattacharya P, Neogi S. Gentamicin coated iron oxide nanoparticles as novel antibacterial agents. Mater Res Express. 2017;4: 095005.
22. Mahmoudi M, Serpooshan V. Silver-coated engineered magnetic nanoparticles are promising for the success in the fight against antibacterial resistance threat. ACS Nano. 2012;6:2656–64.
23. Prucek R, Tuček J, Kilianová M, Panáček A, Kvítek L, Filip J, et al. The targeted antibacterial and antifungal properties of magnetic nanocomposite of iron oxide and silver nanoparticles. Biomaterials. 2011;32:4704–13.
24. Jiang J, Gu H, Shao H, Devlin E. Bifunctional Fe_3O_4–Ag heterodimer nanoparticles for two-photon fluorescence imaging and magnetic manipulation. Adv Mater. 2008;20:4403–7.
25. Liu XM, Li YS. One-step facile fabrication of Ag/γ-Fe_2O_3 composite microspheres. Mater Sci Eng C. 2009;29:1128–32.
26. Lee D, Cohen RE, Rubner MF. Antibacterial properties of ag nanoparticle loaded multilayers and formation of magnetically directed antibacterial microparticles. Langmuir. 2005;21:9651–9.
27. Zhang X, Niu H, Yan J, Cai Y. Immobilizing silver nanoparticles onto the surface of magnetic silica composite to prepare magnetic disinfectant with enhanced stability and antibacterial activity. Colloid Surf A. 2011;375:186–92.
28. Patsula V, Petrovský E, Kovářová J, Konefal R, Horák D. Monodisperse superparamagnetic nanoparticles by thermolysis of Fe(III) oleate and mandelate complexes. Colloid Polym Sci. 2014;292:2097–110.
29. Kostiv U, Patsula V, Šlouf M, Pongrac IM, Škokić S, Dobrivojević Radmilović M, et al. Physico-chemical characteristics, biocompatibility, and MRI applicability of novel monodisperse PEG-modified

magnetic Fe_3O_4&SiO_2 core–shell nanoparticles. RSC Adv. 2017;7: 8786–97.

30. Kostiv U, Janoušková O, Šlouf M, Kotov N, Engstová H, Smolková K, et al. Silica-modified monodisperse hexagonal lanthanide nanocrystals: synthesis and biological properties. Nanoscale. 2015;7:18096–104.

31. Ding HL, Zhang YX, Wang S, Xu JM, Xu SC, Li GH. Fe_3O_4@SiO_2 core/shell nanoparticles: the silica coating regulations with a single core for different core sizes and shell thicknesses. Chem Mat. 2012;24:4572–80.

32. Li M, Wu W, Qiao R, Tan L, Li Z, Zhang Y. Ag-decorated Fe_3O_4@SiO_2 core-shell nanospheres: seed-mediated growth preparation and their antibacterial activity during the consecutive recycling. J Alloys Compd. 2016;676:113–9.

33. Cai Y, Tan F, Qiao X, Wang W, Chen J, Qiu X. Room-temperature synthesis of silica supported silver nanoparticles in basic ethanol solution and their antibacterial activity. RSC Adv. 2016;6:18407–12.

34. Baumgartner J, Bertinetti L, Widdrat M, Hirt AM, Faivre D. Formation of magnetite nanoparticles at low temperature: from superparamagnetic to stable single domain particles. PLoS One. 2013;8:e57070.

35. Garland ER, Rosen EP, Clarke LI, Baer T. Structure of submonolayer oleic acid coverages on inorganic aerosol particles: evidence of island formation. Phys Chem Chem Phys. 2008;10: 3156–61.

36. Dunlop D, Ozdemir O. Rock Magnetism: Fundamentals and Frontiers. Cambridge, UK: Cambridge University Press; 1997.

37. Demortiere A, Panissod P, Pichon BP, Pourroy G, Guillon D, Donnio B, et al. Size-dependent properties of magnetic iron oxide nanocrystals. Nanoscale. 2011;3:225–32.

38. Li Q, Kartikowati CW, Horie S, Ogi T, Iwaki T, Okuyama K. Correlation between particle size/domain structure and magnetic properties of highly crystalline Fe_3O_4 nanoparticles. Sci Rep. 2017;7:9894.

39. Iida H, Takayanagi K, Nakanishi T, Osaka T. Synthesis of Fe_3O_4 nanoparticles with various sizes and magnetic properties by controlled hydrolysis. J Colloid Interface Sci. 2007;314:274–80.

40. Hajipour MJ, Fromm KM, Ashkarran AA, Aberasturi DJ, Larramendi IR, Rojo T, et al. Antibacterial properties of nanoparticles. Trends Biotechnol. 2012;30:499–511.

41. Sondi I, Salopek-Sondi B. Silver nanoparticles as antimicrobial agent: a case study on *E. coli* as a model for gram-negative bacteria. J Colloid Interface Sci. 2004;275:177–82.

42. Kim JS, Kuk E, Yu KN, Kim JH, Park SJ, Lee HJ, et al. Antimicrobial effects of silver nanoparticles. Nanomed Nanotechnol Biol Med. 2007;3:95–101.

43. Yuan YG, Peng QL, Gurunathan S. Effects of silver nanoparticles on multiple drug-resistant strains of *Staphylococcus aureus* and *Pseudomonas aeruginosa* from mastitis-infected goats: an alternative approach for antimicrobial therapy. Int J Mol Sci. 2017;18:569.

44. Matsumura Y, Yoshikata K, Kunisaki S, Tsuchido T. Mode of bactericidal action of silver zeolite and its comparison with that of silver nitrate. Appl Environ Microbiol. 2003;69:4278–81.

45. Feng QL, Wu J, Chen GQ, Cui FZ, Kim TN, Kim JO. A mechanistic study of the antibacterial effect of silver ions on *Escherichia coli* and *Staphylococcus aureus*. J Biomed Mater Res. 2000;52:662–8.

46. Abbaszadegan A, Ghahramani Y, Gholami A, Hemmateenejad B, Dorostkar S, Nabavizadeh M, et al. The effect of charge at the surface of silver nanoparticles on antimicrobial activity against gram-positive and gram-negative bacteria: a preliminary study. J Nanomater. 2015;2015:720654.

47. Yoon SS, Barrangou-Poueys R, Breidt F, Fleming HP. Detection and characterization of a lytic *Pediococcus bacteriophage* from the fermenting cucumber brine. J Microbiol Biotechnol. 2007;17: 262–70.

48. Pal S, Tak YK, Song JM. Does the antibacterial activity of silver nanoparticles depend on the shape of the nanoparticle? A study of the gram-negative bacterium *Escherichia coli*. Appl Environ Microbiol. 2007;73:1712–20.

49. Neal AL. What can be inferred from bacterium-nanoparticle interactions about the potential consequences of environmental exposure to nanoparticles? Ecotoxicology. 2008;17:362–71.

50. Vidanapathirana AK, Thompson LC, Herco M, Odom J, Sumner SJ, Fennell TR, et al. Acute intravenous exposure to silver nanoparticles during pregnancy induces particle size and vehicle dependent changes in vascular tissue contractility in Sprague Dawley rats. Reprod Toxicol. 2018;75:10–22.

51. Li L, Cui J, Liu Z, Zhou X, Li Z, Yu Y, et al. Silver nanoparticles induce SH-SY5Y cell apoptosis via endoplasmic reticulum- and mitochondrial pathways that lengthen endoplasmic reticulum–mitochondria contact sites and alter inositol-3-phosphate receptor function. Toxicol Lett. 2018;285:156–67.

52. Jiang X, Lu C, Tang M, Yang Z, Jia W, Ma Y, et al. Nanotoxicity of silver nanoparticles on HEK293T cells: a combined study using biomechanical and biological techniques. ACS Omega. 2018;3: 6770–8.

53. Sahu SC, Zheng J, Graham L, Chen L, Ihrie J, Yourick JJ, et al. Comparative cytotoxicity of nanosilver in human liver HepG2 and colon Caco2 cells in culture. J Appl Toxicol. 2014;34:1155–66.

Publication No. 2

Cationic Polymer-Coated Magnetic Nanoparticles with Antibacterial Properties: Synthesis and In Vitro Characterization

Anastasiia B. Shatan [1,2], **Vitalii Patsula** [1], **Aneta Dydowiczová** [1], **Kristýna Gunár** [1], **Nadiia Velychkivska** [1], **Jiřina Hromádková** [1], **Eduard Petrovský** [3] **and Daniel Horák** [1,*]

[1] Institute of Macromolecular Chemistry, Czech Academy of Sciences, Heyrovského nám. 2, 162 06 Prague 6, Czech Republic; shatan@imc.cas.cz (A.B.S.); patsula@imc.cas.cz (V.P.); dydowiczova@imc.cas.cz (A.D.); gunar@imc.cas.cz (K.G.); velychkivska@imc.cas.cz (N.V.); hromadkova@imc.cas.cz (J.H.)

[2] Department of Physical and Macromolecular Chemistry, Faculty of Science, Charles University, Hlavova 8, 128 40 Prague 2, Czech Republic

[3] Institute of Geophysics, Czech Academy of Sciences, Boční II/1401, 141 31 Prague 4, Czech Republic; edp@ig.cas.cz

* Correspondence: horak@imc.cas.cz

Abstract: Uniformly sized magnetite nanoparticles (D_n = 16 nm) were prepared by a thermal decomposition of Fe(III) oleate in octadec-1-ene and stabilized by oleic acid. The particles were coated with Sipomer PAM-200 containing both phosphate and methacrylic groups available for the attachment to the iron oxide and at the same time enabling (co)polymerization of 2-(dimethylamino)ethyl methacrylate and/or 2-*tert*-butylaminoethyl methacrylate at two molar ratios. The poly[2-(dimethylamino)ethyl methacrylate] (PDMAEMA) and poly[2-(dimethylamino)ethyl methacrylate-*co*-2-*tert*-butylaminoethyl methacrylate] [P(DMAEMA-TBAEMA)] polymers and the particles were characterized by ^{1}H NMR spectroscopy, size-exclusion chromatography, transmission electron microscopy, dynamic light scattering, thermogravimetric analysis, magnetometry, and ATR FTIR and atomic absorption spectroscopy. The antimicrobial effect of cationic polymer-coated magnetite nanoparticles tested on both *Escherichia coli* and *Staphylococcus aureus* bacteria was found to be time- and dose-responsive. The P(DMAEMA-TBAEMA)-coated magnetite particles possessed superior biocidal properties compared to those of P(DMAEMA)-coated one.

Keywords: magnetic; nanoparticles; antibacterial activity; 2-(dimethylamino)ethyl methacrylate; 2-*tert*-butylaminoethyl methacrylate

1. Introduction

The invention of antibiotics in the 1940s saved millions of lives and many infectious diseases became far less deadly. However, bacteria have currently developed resistance to antibiotics, which is now a major threat for public health [1–3]. Moreover, there is a need for disinfection of drinking water in remote areas using alternative approaches to chlorination, in order to eliminate pathogens responsible for waterborne diseases. There are other physical processes to disinfect the contaminated water including filtration, thermal treatment, or UV irradiation; however, these methods suffer from limitations, such as time demand, high price, waste of resources, use of various additives and agents, etc. [4]. In a search for new, cheap, and simple solutions of these problems, a significant effort has been devoted to the development of antibacterial agents based on nanoparticles [5–7]. In contrast to conventional antibiotics, such materials possess a range of unique physicochemical and biological properties, e.g., high surface-to-volume ratio that increases contact area with microorganisms, high stability, possibility of easy modification with various functional groups, ligands, targeting agents and other biomolecules, enabling not only disinfection, but also its monitoring and targeting [8–10]. Particles possessing sterilization properties are typically based on silver, copper, various metal oxides or sulfides, or carbon nanotubes [11].

Among the different types of nanoparticles, the magnetic ones especially show a great potential for various biomedical applications, such as magnetic resonance imaging, hyperthermia, drug delivery, tissue repair, and cell and tissue targeting and transfection [9]. Due to these distinct characteristics, including response to external magnetic force, it is of great interest to also explore their applicability as a carrier of antibacterial polymers. Such nanomaterials can be highly efficient biocides that would be easily manipulatable, recyclable, and reusable by using an external magnetic field. At the same time, the functional antibacterial magnetic nanoparticles based on iron oxides could overcome pathogen's multi-drug resistibility inhibiting bacterial growth [12,13]. The antibacterial mechanism of these nanoparticles was mainly attributed to dissolved metal ions and the gene-ration of reactive oxygen species [7]. They could also electrostatically bind to the cell membrane, inducing disorder in the bacteria functions and leading to cell death [13].

Many materials and methods have been already described for iron oxide synthesis and surface modification with the aim to provide colloidal stability of the dispersions, compatibility with the living tissues, and attachment of target molecules. For example, conjugation of macromolecules to the particle surface was achieved by anchoring groups, such are aromatic vicinal diols, carboxyl, bisphosphonate, phosphate, or hydroxamate groups, capable of strong interactions with iron [14]. The strongest binding was achieved with phosphate groups present, e.g., in penta(propylene glycol) methacrylate phosphate (Sipomer PAM-200). Sipomer PAM-200 is a heterobifunctional macromonomer built of five propylene oxide units and containing a reactive methacrylic group with a double bond that allows the radical polymerization with a monomer [15,16]. Moreover, Sipomer PAM-200 is terminated with a phosphate group able to interact with the iron oxide. To confer biocidal properties to the particles and/or prevent antibiotic resistance, the particles were also modified with antimicrobial polymers that can reduce general toxicity and ensure colloidal stability [17–19]. Typical examples of such compounds included polymers with quaternary ammonium, pyridinium, and/or phosphonium cations [19–24]. Their bactericidal activity originated from the interaction of the cationic sites of the polymer with negatively charged membrane proteins of bacteria, which were ultimately disrupted. For example, mucoadhesive and thermoresponsive poly[2-(dimethylamino)ethyl metha-crylate] (PDMAEMA) was incorporated in antimicrobial copolymers to inhibit growth of *Staphylococcus aureus* [25,26] and *Escherichia coli* [27]. Other PDMAEMA applications included nonviral gene delivery [28], drug delivery [29], water purification [30], or protein separation [31]. In addition to PDMAEMA, another antimicrobial polymer, poly(2-*tert*-butylaminoethyl methacrylate) (PTBAEMA) that is hydrophobic was contained in various blends or capsules [32–34]. It displaced Ca^{2+} and/or Mg^{2+} ions from the outer bacterial membrane, which became disorganized and disrupted [33,35]. Obviously, large pendant *tert*-butylamino groups of PTBAEMA were not necessarily quaternized to become antibacterial.

The aim of this report was to anchor water-soluble antibacterial polymers prepared by free-radical polymerization of DMAEMA and TBAEMA to a magnetic carrier to make it colloidally stable, offer high surface area available for interactions with bacteria, and investigate antimicrobial activity of the particles against *E. coli* and *S. aureus*. The advantages of this new nanomaterial consist of its easy manipulation, targeting, and separation from liquid media using a magnet.

2. Experimental

2.1. Materials and Methods

Octadec-1-ene (OD), $FeCl_3·6H_2O$ (98%), 2-(dimethylamino)ethyl methacrylate (DMAEMA), *tert*-butylaminoethyl methacrylate (TBAEMA), Hank's balanced salt solution (HBSS), and Luria broth (LB) were purchased from Sigma-Aldrich (St. Louis, MO, USA). Oleic acid (OA; 95%), ethanol (99%), hexane (99%), HCl (35%), and NaOH (98.6%) were obtained from Lach-Ner (Neratovice, Czech Republic). Sipomer PAM 200 (M_w = 451 Da; acronym S) was from Rhodia (Courbevoie, France). Cellulose membrane (100 kDa) for dialysis was purchased from Spectrum Europe (Breda, Netherlands). Fe(III) oleate was prepared according to an earlier report [36].

All other chemicals were purchased from Sigma-Aldrich. Ultrapure Q-water ultrafiltered on a Milli-Q Gradient A10 system (Millipore; Molsheim, France) was used in the experiments.

Antibacterial activity of nanoparticles was evaluated using two types of cultures: Gram-positive bacteria represented by *Staphylococcus* (*S.*) *aureus* and Gram-negative bacteria *Escherichia* (*E.*) *coli*. Both bacterial strains were isolated and identified at the Institute of Immunology and Microbiology of the 1st Faculty of Medicine and General University Hospital in Prague, Czech Republic. Bacteria cultures were cultivated on Luria agar (LA) plates (Sigma-Aldrich) at 37 °C.

2.2. Preparation of Sipomer PAM-200-Coated Fe_3O_4 Nanoparticles

OA-stabilized Fe_3O_4 nanoparticles (MNP) were obtained by a thermal decomposition of Fe(III) oleate as reported earlier [37,38]. Briefly, Fe(III) oleate (5.76 g) was dissolved in a mixture of OD (31.61 g) and OA (4.51 g), the reaction mixture was preheated at 120 °C for 60 min under argon flow and then heated at 320 °C for 30 min. After cooling to room temperature (RT), ethanol (100 Ml) was added and the resulting particles were separated by a magnet and washed with hot ethanol (60–70 °C) three times (50 Ml each). Finally, oleic acid-stabilized Fe_3O_4 particles (0.2 g) and Sipomer PAM-200 (0.4 g) were dispersed in toluene (25 mL), the mixture was sonicated (20% of power) in an ice-water bath for 5 min, kept under argon atmosphere for 15 min, and stirred (900 rpm) at RT for 48 h. The resulting Sipomer PAM-200-coated Fe_3O_4 particles (denoted as MNP@S) were precipitated in hexane three times (100 mL each), separated by a magnet to remove residual solvents and OA, dispersed in tetrahydrofuran (THF), and stored at 4 °C.

2.3. Modification of MNP@S by DMAEMA-Based Polymers

DMAEMA-based homo- and copolymers were grafted on the surface of MNP@S. Briefly, DMAEMA (denoted as D) was free radically polymerized or D was copolymerized with TBAEMA (denoted as T) at 1/0, 0.75/0.25, and 0.5/0.5 molar ratios on MNP@S (50 mg) in THF (5 mL) with ACVA as an initiator (2.1 mg) at 70 °C for 18 h. The resulting poly[(2-dimethylamino)ethyl methacrylate]-, poly[2-(dimethylamino)ethyl methacrylate-*co*-2-*tert*-butylaminoethyl methacrylate] (0.75/0.25 mol/mol)-, and poly[2-(dimethylamino)ethyl methacrylate-*co*-2-*tert*-butylaminoethyl methacrylate] (0.5/0.5 mol/mol)-mo-dified MNP@S were denoted as MNP@S-D, MNP@S-D-T1, and MNP@S-D-T2, respectively. They were precipitated with hexane three times (100 mL each), separated by a magnet, redispersed in water, and dialyzed against water using a cellulose dialysis membrane (MWCO 300 kDa) for 48 h to remove excessive polymer. Finally, the particle dispersions were freeze-dried and stored. The composition and purity of PDMAEMA and its copolymers was con-firmed by ^{1}H NMR analysis; the following ratio was calculated: DMAEMA/TBAEMA = a_x/m_x: a_y/m_y, where a_x and a_y are the area under ^{1}H NMR peak of $(CH_3)_2$ and $(CH_3)_3$, respectively, and m_x and m_y are the number of $(CH_3)_2$ and $(CH_3)_3$ protons, respectively.

2.4. Physicochemical Characterization

High-resolution ^{1}H NMR spectra were acquired in deuterated water with a Bruker Avance III 600 spectrometer operating at 600.2 MHz and processed with the Topspin 4.0.5 software (both Bruker; Billerica, MA, USA). Measurements were as follows: 90° pulse width 10 μs, relaxation delay 10 s, spectral width 7211 Hz, acquisition time 4.54 s, and 32 scans. The integrated intensities were determined using the spectrometer integration software with an accuracy of ±1%. During the measurements, temperature was maintained at 25 ± 0.2 °C using a BVT 3000 temperature unit.

The size-exclusion chromatography (SEC) of the polymers was performed at 25 °C with a TSKgel SuperAW-L guard column (L × I.D. 4.6 mm × 3.5 cm, particle size 7 μm; Polymer Laboratories; Church Stretton, UK) and UVD 305 (Watrex; Prague, Czech Republic) and RI-101 (Shodex; Tokyo, Japan) detectors. Methanol/acetate buffer mixture (80/20 *v/v*) was used as a mobile phase at a flow rate of 0.5 mL/min. The molar mass was calculated us-ing Clarity software (DataApex; Prague, Czech Republic) with poly-styrene as a calibration

standard. The samples for both ^{1}H NMR and SEC analysis were prepared by dissolution of the polymer-coated MNP in 2 M HCl; pH of the solution was adjusted to 7 and the solution was dialyzed against water using a cellulose dialysis membrane (MWCO 3.5 kDa) and purified on a Sephadex^{TM} LH-20 column (Merck; Kenilworth, NJ, USA).

Morphology, size, and size distribution of the particles were analyzed with a Tecnai G2 Spirit Twin 12 transmission electron microscope (TEM; FEI; Brno, Czech Republic) [10]. Number-average diameter ($D_n = \Sigma N_i \cdot D_i / \Sigma N_i$), weight-average diameter ($D_w = \Sigma N_i \cdot D_i^4 / \Sigma N_i \cdot D_i^3$), and dispersity ($Đ = D_w / D_n$) were calculated from at least 500 individual particles from the TEM micrographs using Atlas software (Tescan, Brno, Czech Republic).

Hydrodynamic diameter (D_h), polydispersity (PD), and ζ-potential were obtained by dynamic light scattering (DLS) using a ZEN 3600 Zetasizer Nano instrument (Malvern Instruments; Malvern, UK) at RT and different pHs. The D_h was calculated from the intensity-weighted distribution function obtained by CONTIN analysis of the correlation function embedded in Malvern software as well as electrophoretic mobility of the magnetic nanoparticles, which was converted to ζ-potential using the Smoluchowski equation.

A PerkinElmer 3110 atomic absorption spectrometer (AAS) was used to analyze the amount of iron in the particles by measuring the solution obtained after their mineralization with 68% $HClO_4$/65% HNO_3 (4/1 *v/v*) mixture at 80 °C for 20 min. The amount of phosphorus was determined after the mineralization and mixing with sulfuric acid, ammonium molybdate, ascorbic acid, and antimony potassium tartrate using a PerkinElmer Lambda 20 UV-Vis spectrometer at 690 nm.

ATR FTIR spectra were recorded on a PerkinElmer Paragon 1000PC spectrometer equipped with a Specac MKII Golden Gate single attenuated total reflection system with a diamond crystal; the angle of incidence was 45°.

Thermogravimetric analysis (TGA) was performed in air at 20–650 °C with a heating rate of 10 °C/min using a PerkinElmer TGA 7 analyzer and Pyris 1 software (Shelton, CT, USA).

Magnetic properties, namely coercivity and induced remanent magnetization were measured using an EV9 vibrating sample magnetometer (MicroSense; Lowell, MA, USA) at RT and maximum magnetic field of 1 T. Hysteresis loops were determined with different field steps from 500 Oe (0.05 T) in the highest field range (300 mT–1 T) to the finest step of 5 Oe (0.5 mT) in the lowest field range (−25–25 mT) at the intersections with magnetization and field axes. This allowed reliable determination of saturation remanent magnetization M_{rs}, i.e., magnetization at zero field (the intersection with the magnetization axis), and coercive force B_c that is field necessary to induce zero magnetization (the intersection with the field axis). The two parameters were determined on both the ascending and descending branches of the hysteresis loop and resulting average values were considered. Saturation induced magnetization M_s was determined as the maximum induced magnetization after subtraction of the linear paramagnetic part of the loop at >0.5 T. Here, the ferrimagnetic response to external field was saturated and reflected by closed, reversible, and linear ascending and descending branches of the loop. Again, average M_s values were calculated, reflecting the concentration of ferrimagnetic substance in the specimen. To check its ability to acquire remanent magnetization, the measurements were performed in zero field after application of a step-wise increasing magnetic field, with 50 Oe (5 mT) field steps and 5000 Oe (0.5 T) maximum field. Remanent magnetization in true superparamagnetic particles at RT should decay rapidly to zero. Finally, after application of the maximum field, the same process was repeated, but with the field applied in the opposite direction. The field is necessary to remove M_{rs} named coercivity of remanence (B_{cr}) and, similarly like M_{rs} and coercivity B_c, it reflects magnetite particle size.

2.5. Antibacterial Activity of MNP@S-D and MNP@S-D-T

In 24-well plates (TPP; Trasadingen, Switzerland), overnight cultures of *S. aureus* and *E. coli* were resuspended in HBSS and diluted in LB (1 mL) to cultivate bacteria at 1×10^5 colony-forming units (CFU) per mL. The MNP@S-D and MNP@S-D-T nanoparticles (5.5, 44,

and 175 µg/mL) were added to the bacteria cultures and incubated at 37 °C with shaking (125 rpm). Culture without any treatment (NT) and containing ampicillin (150 µg/mL) served as a negative and positive control, respectively. After the exposure to nanoparticles, the bacteria aliquots were taken from the wells in time intervals of 0, 1, and 4 h, diluted $100\times$, $1000\times$, or $1{,}000{,}000\times$, seeded on LA plates, and incubated at 37 °C for 24 h. The procedure was repeated three times in duplicates and bacterial CFU/mL were calculated. The viability was calculated as a ratio of the number of living bacteria at given time interval to the number of living bacteria in NT. Data were analyzed by the GraphPad Prism5 software and two-way ANOVA followed by Bonferroni's test.

3. Results and Discussion

3.1. Synthesis of MNP and Their Physicochemical Characterization

OA-stabilized magnetite cores were synthesized by a thermal decomposition method in a non-polar high-boiling organic solvent (OD; Figure 1). The method allowed us to prepare magnetic nanoparticles with a very narrow size distribution, high crystallinity, and controlled diameter [39]. The synthesis proceeded in three steps: (i) formation of poly(iron oxo) clusters from an iron oleate serving as building blocks for the particle growth, (ii) short burst nucleation with formation of the particle seeds, and (iii) nanoparticle growth with increasing reaction temperature [36,40].
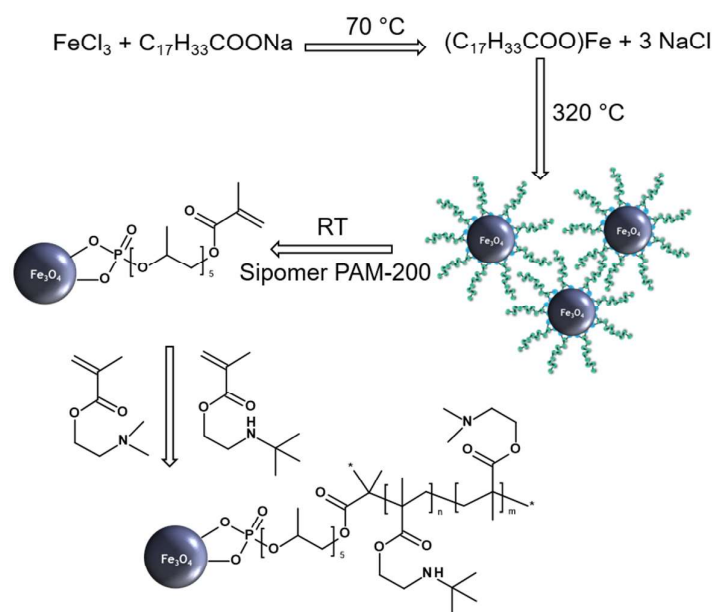

Figure 1. Synthesis of Fe_3O_4 nanoparticles, their modification with Sipomer PAM-200 and poly[2-(dimethylamino)ethyl methacrylate] or poly[2-(dimethylamino)ethyl methacrylate-*co*-2-(*tert*-butylamino)ethyl methacrylate].

Due to the combination of short nucleation time and the presence of a stabilizer that prevents the nuclei aggregation and ensures the same conditions for each particle growth the resulting particles had controlled size (D_n = 16 nm) with low dispersity ($Đ < 1.05$) according to TEM (Figure 2a). Additionally, polydispersity ($PD = 0.13$) from DLS documented a very narrow particle size distribution (Table 1). The hydrodynamic diameter of nanoparticles measured in toluene was larger (D_h = 36 nm) than D_n due to the OA adsorbed on the particle surface. The FTIR spectra of MNP exhibited three peaks at 1460, 2844, and 2919 cm^{-1} attributed to $v_d(CH)$ deformation vibration, and $v_s(CH_2)$ symmetric and $v_{as}(CH_3)$ asymmetric stretching vibration, respectively (Figure 3a). The bands at 1559 and 1703 cm^{-1} corresponded to $v_a(COO^-)$ asymmetric and $v(COOH)$ stretching vibrations,

respectively. Therefore, FTIR spectroscopy confirmed the presence of OA coating on the Fe₃O₄ nanoparticle surface. According to TGA, the amount of organic compounds on the MNP surface equaled to 84 wt.%.
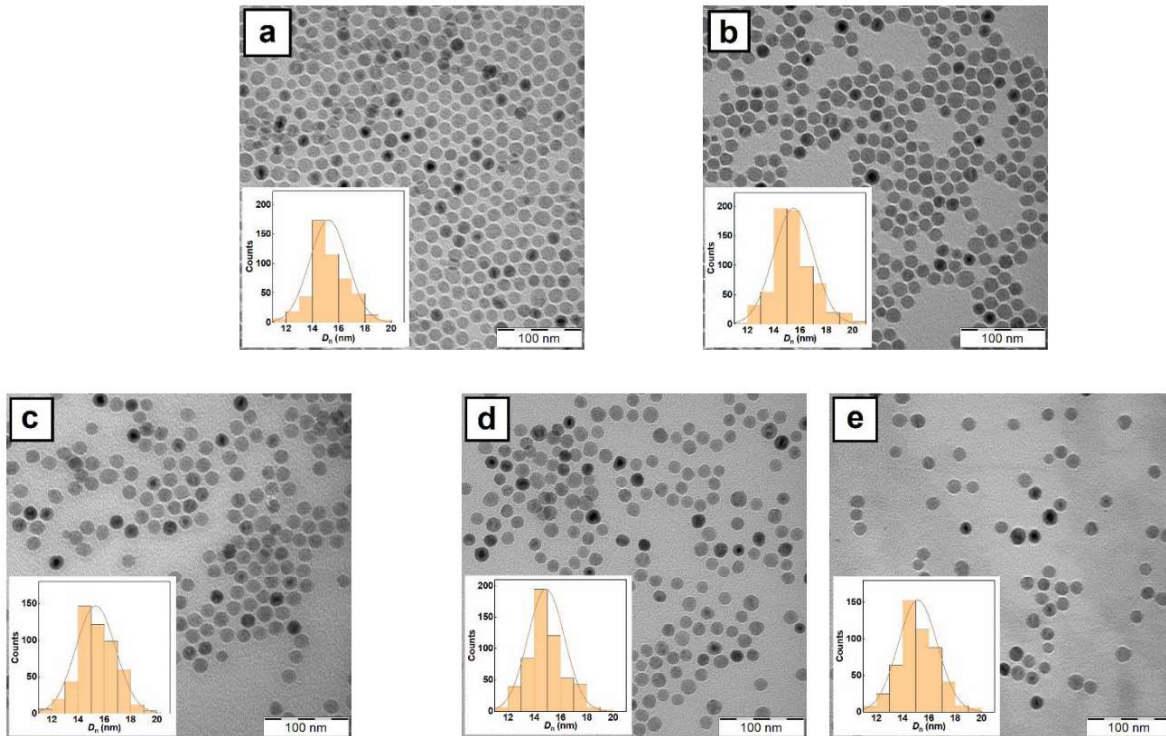

Figure 2. TEM micrographs of (**a**) MNP, (**b**) MNP@S, (**c**) MNP@S-D, (**d**) MNP@S-D-T1, and (**e**) MNP@S-D-T2.
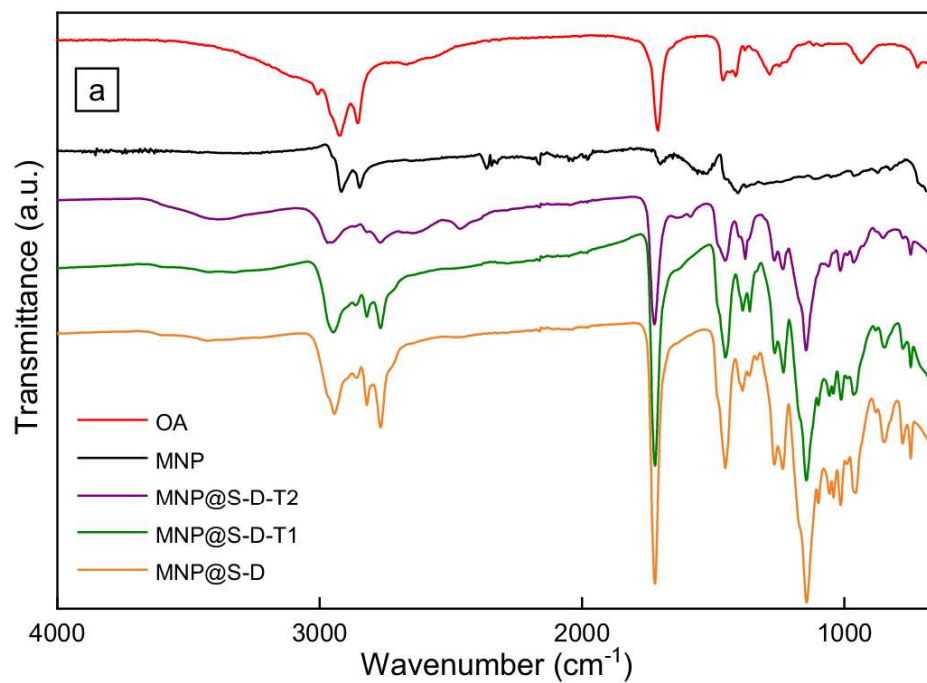

Figure 3. *Cont.*
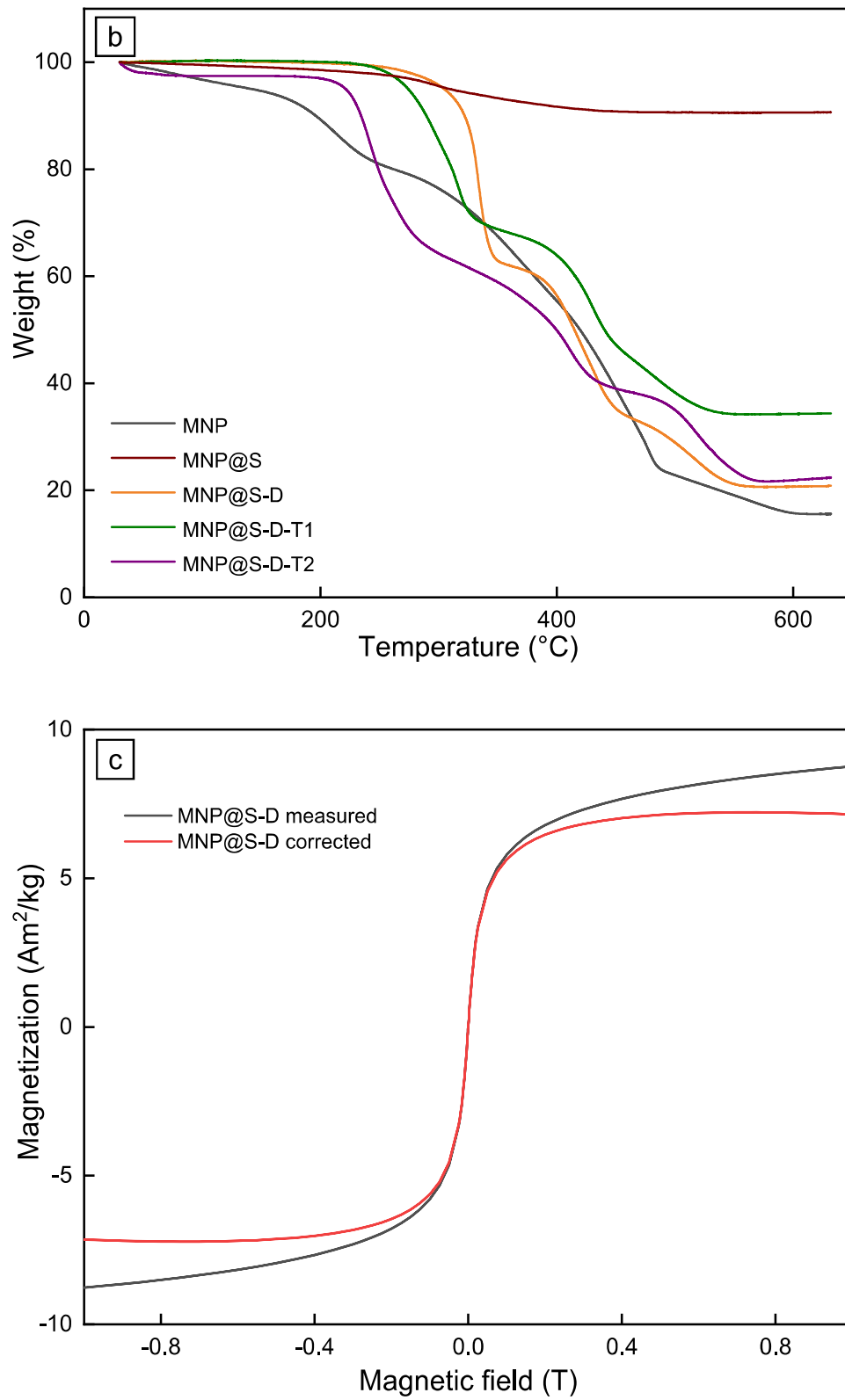
Figure 3. (**a**) FTIR and (**b**) TGA spectra of OA, MNP, MNP@S-D, MNP@S-D-T1, and MNP@S-D-T2. (**c**) Hysteresis loop of the MSP-S-D.

Table 1. Physicochemical characterization of the iron oxide nanoparticles.

Particles	D_n (nm)	$Đ$	D_h (nm)	PD	ζ-Potential (mV)	B_c (mT)	M_{rs} (10^{-3} A·m²/kg)	M_s (A·m²/kg)
MNP	16	1.02	36 [a]	0.13	-	-	-	-
MNP@-S	16	1.03	28 [a]	0.16	-	-	-	-
MNP@S-D	16	1.03	140 [b]	0.19	48	0.0292	6.584	7.190
MNP@S-D-T1	16	1.02	110 [b]	0.18	51	0.0371	8.851	11.228
MNP@S-D-T2	16	1.03	98 [b]	0.17	46	0.0469	10.395	7.163

D_n—number-average particle diameter (TEM); $Đ$—dispersity (TEM); D_h—hydrodynamic diameter (DLS; [a] in toluene or [b] in water); PD—polydispersity index (DLS); B_c—coercive force; M_{rs}—saturation remanent magnetization; M_s—saturation magnetization.

3.2. Surface Modification of MNP with Sipomer PAM-200

For the application of antibacterial MNP in disinfection of aqueous media, water-dispersible nanoparticles are required. However, the original magnetic particles contained hydrophobic OA coating and therefore they have to be modified with a hydrophilic polymer such as PDMAEMA to provide both dispersibility and colloidal stability of particles in water. To ensure efficient attachment of both PDMAEMA and its copolymers to the iron oxide surface, Sipomer PAM-200 terminated with phosphate groups was selected as a mediator. While the phosphate group enabled attachment of Sipomer PAM-200 to the iron oxide, which was superior to a mere physical adsorption, its reactive methacrylic group with a vinyl bond separated by a ten-carbon spacer from phosphate anchoring group allowed the free-radical copolymerization of DMAEMA monomer [16]. Analogously to OA, Sipomer PAM-200 due to its low contrast was not visible on the TEM micrograph (Figure 2b). The hydrodynamic diameter of MNP@S only slightly decreased to 28 nm compared to the initial nanoparticles, probably due to poorer solvation of Sipomer PAM-200 shell in toluene than that of OA (Table 1).

3.3. Modification of MNP@S with PDMAEMA and P(DMAEMA-TBAEMA)

From various antimicrobial polymers intended as a coating for the MNP, cationic PDMAEMA and PTBAEMA were selected due to their mucoadhesive, antibacterial, and stimuli-sensitive properties [25,41]. As the PTBAEMA has limited solubility in water, TBAEMA was copolymerized with a highly hydrophilic DMAEMA monomer to obtain water-dispersible antibacterial magnetic agents. At the beginning, different DMAEMA/TBAEMA molar ratios (1/0, 0.75/0.25, 0.5/0.5, 0.25/0.75) were studied in the preparation of polymers. While the MNP coated with copolymers prepared at the DMAEMA/TBAEMA ratio of 0.25/0.75 mol/mol were too hydrophobic and thus non-dispersible in water, the MNP@S-D, MNP@S-D-T1, and MNP@S-D-T2 prepared with DMAEMA/TBAEMA ratios equaling to 1/0, 0.75/0.25, and 0.5/0.5 mol/mol, respectively, were water-dispersible and therefore tested in further experiments (Table 1). The compositions of PDMAEMA and P(DMAEMA-TBAEMA) copolymers with different DMAEMA/TBAEMA molar ratios were investigated by ¹H NMR spectroscopy by comparing methyl signals of side chains from DMAEMA and TBAEMA (Figure 4). The "1" resonance found at 2.1 ppm corresponded to $(CH_3)_2$ from DMAEMA chains, while signal "1" situated at ~1 ppm was related to $(CH_3)_3$ protons from TBAEMA. Calculated monomer ratios in the (co)polymers were in good agreement with those added in the polymeri-zation feed. The weight- (M_w), number-average molar mass (M_n), and polydispersity (M_w/M_n) of the polymers determined by SEC analysis showed that with increasing DMAEMA/TBAEMA ratio M_w of S-D, S-D-T1, and S-D-T2 polymers increased from 145 to 195 and 240 kDa, respectively; polydispersity remained rather low (M_w/M_n = < 1.2) due to the purification of polymers by dialysis and/or chromatography.
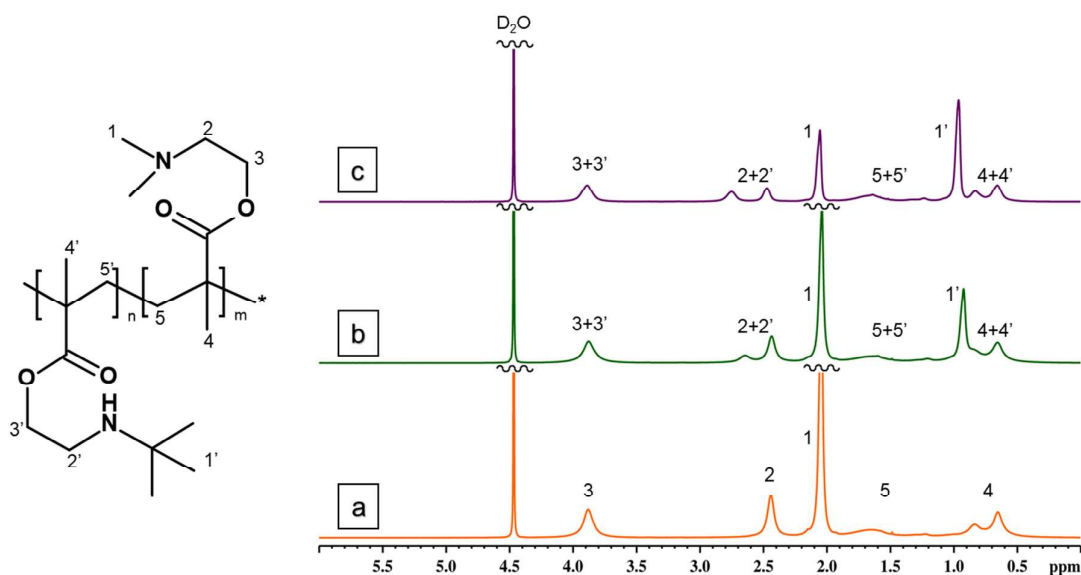
Figure 4. High-resolution ^{1}H NMR spectra of (**a**) poly[2-(dimethylamino)ethyl methacrylate], (**b**) poly[2-(dimethylamino)ethyl methacrylate-*co*-2-(*tert*-butylamino)ethyl methacrylate] (0.75/0.25 mol/mol), and (**c**) poly[2-(dimethylamino)ethyl methacrylate-*co*-2-(*tert*-butylamino)ethyl methacrylate] (0.5/0.5 mol/mol) measured in D$_2$O at 25 °C. Resonance assignment of PDMAEMA and PDMAEMA-TBAEMA copolymers is shown in the spectra.

In the next experiments, PDMAEMA- and P(DMAEMA-TBAEMA)-coated MNP were thoroughly physicochemically characterized. The TEM micrographs of MNP@S-D, MNP@S-D-T1, and MNP@S-D-T2 did not differ from those of starting Fe$_3$O$_4$ as the polymer coatings were not contrasted in the images (Figure 2c–e). The long-term colloidal stability of MNP@S-D, MNP@S-D-T1, or MNP@S-D-T2 in water (pH 6) was demonstrated by determination of D_h and ζ-potential, reaching 140, 110, or 98 nm and 48, 51, or 46 mV, respectively (Table 1). At this pH, amino groups of PDMAEMA were partially protonated and, as a result, the ξ-potential was quite high. It was typical that the hydrodynamic diameter D_h of particles measured by DLS in water was larger than the number-average diameter according to TEM due to several reasons. In DLS, the hydrodynamic diameter is determined by the autocorrelation function that compares the fluctuation of intensity of scattered light and provides z-average diameter (more sensitive to bigger particles). In contrast, TEM provides the number-average diameter that is in principle smaller than the D_h. Moreover, the DLS measures the particles in water, where the polymer coatings can be swollen, while the TEM analyzes dry specimens. Finally, last but not least, the particles form doublets, triplets, and other small aggregates in water, whereas individual particles are calculated from TEM micrographs. The presence of phosphate groups on the particles was confirmed by the UV-Vis spectroscopy that revealed 0.88, 0.69, and 0.42 wt.% of phosphorus in the MNP@S-D, MNP@S-D-T1, and MNP@S-D-T2, respectively. These values agreed with the literature data, where Sipomer PAM-200-coated γ-Fe$_2$O$_3$ nanoparticles contained 1.49 wt.% of phosphorus [16]. The content of PDMAEMA-based coatings on the particles, w(polymer), was indirectly calculated not only from the amount of phosphorus, but also from the quantity of iron determined by AAS. Since the PDMAEMA or PTBAEMA did not contain any Fe or P, the content of PDMAEMA-based polymers on the particles could be calculated from the amount of the elements w(Fe) and w(P) according to Equation (1):

$$w(\text{polymer}) = 100 - w(\text{Fe}) \times 100/72.4 - w(\text{P}) \times 100/6.8 \qquad (1)$$

where 72.4 and 6.8 are percentages of Fe and P in neat Fe$_3$O$_4$ and Sipomer PAM-200, respectively. As a result, 67, 55, and 76 wt.% of methacrylate-based polymers was determined

in the MNP@S-D, MNP@S-D-T1, and MNP@S-D-T2, respectively. It should also be noted that the MNP@S-D contained 14.4 wt.% Fe according to AAS, therefore, the calculated percentage of Fe_3O_4 and coating including Sipomer PAM-200 was 20 and 80 wt.%, respectively (Table 2). This was in agreement with the amount of coating determined by TGA (79 wt.%; Table 2). Similarly, MNP@S-D-T1 and MNP@S-D-T2 contained 65 and 82 wt.% of the P(DMAEMA-TBAEMA) copolymer according to AAS, while TGA revealed 66 and 78 wt.% of the polymer, which was again in a reasonable agreement.

Table 2. Results of UV-Vis analysis and AAS of MNP modified with poly[2-(dimethylamino)ethyl methacrylate] and poly[2-(dimethylamino)ethyl methacrylate-*co*-2-*tert*-butylaminoethyl methacrylate].

Particles	Content (wt.%)		Coating [c] (wt.%)		
	P [a]	Fe [b]	UV-Vis	Magnetometry	TGA
MNP@S-D	0.88	14.4	80	87	79
MNP@S-D-T1	0.69	25.0	65	80	66
MNP@S-D-T2	0.42	13.2	82	87	78

[a] UV-Vis analysis; [b] AAS; [c] including Sipomer PAM-200.

The surface composition of MNP@S-D, MNP@S-D-T1, and MNP@S-D-T2 was further analyzed by FTIR spectroscopy (Figure 3a). The bands at 1148, 1454, and 1720 cm^{-1} were attributed to ν_{as}(C-O-C) asymmetric stretching, δ(CH$_2$) bending, and ν(C=O) stretching vibration, respectively. The two peaks located at 2861 and 2941 cm^{-1} were ascribed to ν_s(CH$_2$) symmetric and ν_{as}(CH$_3$) asymmetric stretching vibrations respectively. The broad band at 3380 cm^{-1} was assigned to ν(OH) stretching vibration of adsorbed water. The content of polymer on the particle surface was then analyzed by TGA (Figure 3b). In the MNP@S-D-T2, the initial weight loss observed at <100 °C was assigned to dehydration of particles. In the MNP@S-D, MNP@S-D-T1, and MNP@S-D-T2, the weight loss occurred at the temperatures ranges 219–584, 210–580, and 184–594 °C, respectively, that were associated with the decomposition of the polymer shell. After considering the Sipomer PAM-200 contribution (8 wt.%; Figure 3b), the content of PDMAEMA or P(DMAEMA-TBAEMA) was 77, 63, and 76 wt.% for MNP@S-D, MNP@S-D-T1, and MNP@S-D-T2, respectively. This amount of polymer coating was enough to ensure good colloidal stability of particles even after one month of storage. In addition, with increasing proportion of TBAEMA in the coating from 0 to 50 mol.%, the thermal stability of shell decreased, i.e., the decomposition of polymer started already from 219 to 184 °C, respectively. Consequently, it can be concluded that all three types of nanoparticles were stable at temperatures < 180 °C, which is quite sufficient in terms of prospective heat sterilization needed for biological experiments.

To prove the superparamagnetic character of the particles, their magnetic properties were examined. The measurements of remanent magnetization in zero field, i.e., acquisition of remanent magnetization as well as back-field remagnetization, yielded noisy curves close to zero. The inability of material to acquire stable remanent magnetization is typical for truly superparamagnetic particles, where the collective behavior due to interparticle interactions is absent. This was supported by the shape of hysteresis loops passing virtually through the origin and yielding coercive force B_c < 1 Oe (0.1 mT). Additional-ly, determination of M_{rs} from the induced magnetization measurements was obstructed by the very narrow loops (exemplified on Figure 3c; Table 1). Moreover, the data suggested that there were no interparticle magnetic interactions which might cause collective behavior and unwanted particle clustering in the magnetic field. Despite high degree of uncertainty, both parameters (M_{rs} and B_c) suggested an increasing trend (Table 1). The only reliably determined magnetic parameter was saturation induced magnetization M_s, reflecting the concentration of ferrimagnetic particles and confirming that the particles could be removed from aqueous suspensions using a magnet [42]. Stable single-domain and coarse multi-domain magnetite and maghemite have saturation magnetization of ~92 and ~80 A·m^2/kg, respectively; however, magnetic parameters of synthetic nanosized iron oxides are known

to be size-dependent [43,44]. Coercive force and saturation remanence of our synthesized particles were well below the minimum values for nanosized magnetite, indicating that the particle size was ~10 nm [44]. Consequently, saturation magnetization of ~55 A·m^2/kg was used to estimate the upper limit of iron oxide concentration (Table 1). Hence, the content of Fe$_3$O$_4$ in MNP@S-D, MNP@S-D-T1, and MNP@S-D-T2 could be calculated, amounting to 13, 20, and 13 wt.%, respectively, that corresponded to 80 and 87 wt.% of coating (Table 2). These results approximately agreed with those from analysis of phosphorus and TGA.

3.4. Antibacterial Activity of the Particles

Cationic polymers, exemplified by thermo- and pH-responsive PDMAEMA, or hydrophobic TBAEMA are known to be promising antimicrobial agents [25,41]. Here, antimicrobial properties of MNP@S-D, MNP@S-D-T1, and MNP@S-D-T2 were investigated against two commonly used species of pathogen bacteria, namely, *S. aureus* and *E. coli*. These bacteria are Gram-negative (*E. coli*) and Gram-positive (*S. aureus*) containing structurally different cell walls. Biocidal processes involving the nanoparticle uptake by microorganisms consist of several steps, such as adsorption of the particles on bacterial cell surface, penetration through the cell wall, binding to cytoplasmic membrane and its disruption, release of cytoplasmic contents, and, finally, cell death [26,45]. The antibacterial mechanism of cationic DMAEMA and hydrophobic TBAEMA polymers might be based on a similar principle like the electrostatic interaction between a cationic compound and negatively charged constituents on the cell surface and/or hydrophobic interactions [25,26,34,46]; however, these effects can be strain-specific due to the distinct cell wall structures. In contrast to the Gram-positive bacteria, the Gram-negative ones possess an extra outer membrane composed of phospholipids, proteins, and lipopolysaccharides, which generally enable stronger protection against agents migrating to the cytoplasm [46]. In addition, Gram-negative bacteria require less charged and hydrophobic polymers to permeabilize the outer membrane [26].

Antimicrobial activity of MNP@S-D, MNP@S-D-T1, and MNP@S-D-T2 (5.5, 44, and 175 μg/mL) against *S. aureus* and *E. coli* was determined after 0, 1, and 4 h of exposition. The effects were time- and concentration-dependent (Figure 5). The highest concentration of MNP@S-D-T1 and MNP@S-D-T2 (175 μg/mL) at time point 0 h decreased viability in both bacterial species more compared to that in the presence of MNP@S-D (Figure 5a). Higher concentrations of all types of nanoparticles (175 and 44 μg/mL) at time point 0 h resulted in lower viability of *E. coli* than that of *S. aureus*. A similar trend was observed after incubation of MNP@S-D and MNP@S-D-T1 for 1 h (Figure 5b). On the other hand, the lowest concentration of nanoparticles (5.5 μg/mL) incubated for 4 h induced higher viability of *E. coli* than that of *S. aureus* (Figure 5c). Moreover, the particles exhibited stronger antimicrobial activity after 1 h of incubation than at time point 0 h, indicating a beneficial effect of longer exposition of bacteria to nanoparticles in order to damage the cell wall. All types of particles (175 and 44 μg/mL) after 4 h of incubation affected bacterial viability of both cultures that decreased almost to zero (Figure 5c). Overall, the results showed that the MNP@S-D, MNP@S-D-T1, and MNP@S-D-T2 exhibited strong antimicrobial activity against both *E. coli* and *S. aureus* and their effectiveness depended on tested microorganism, concentration of particles, and their coating. In particular, MNP@S-D-T1 possessed superior biocidal properties.
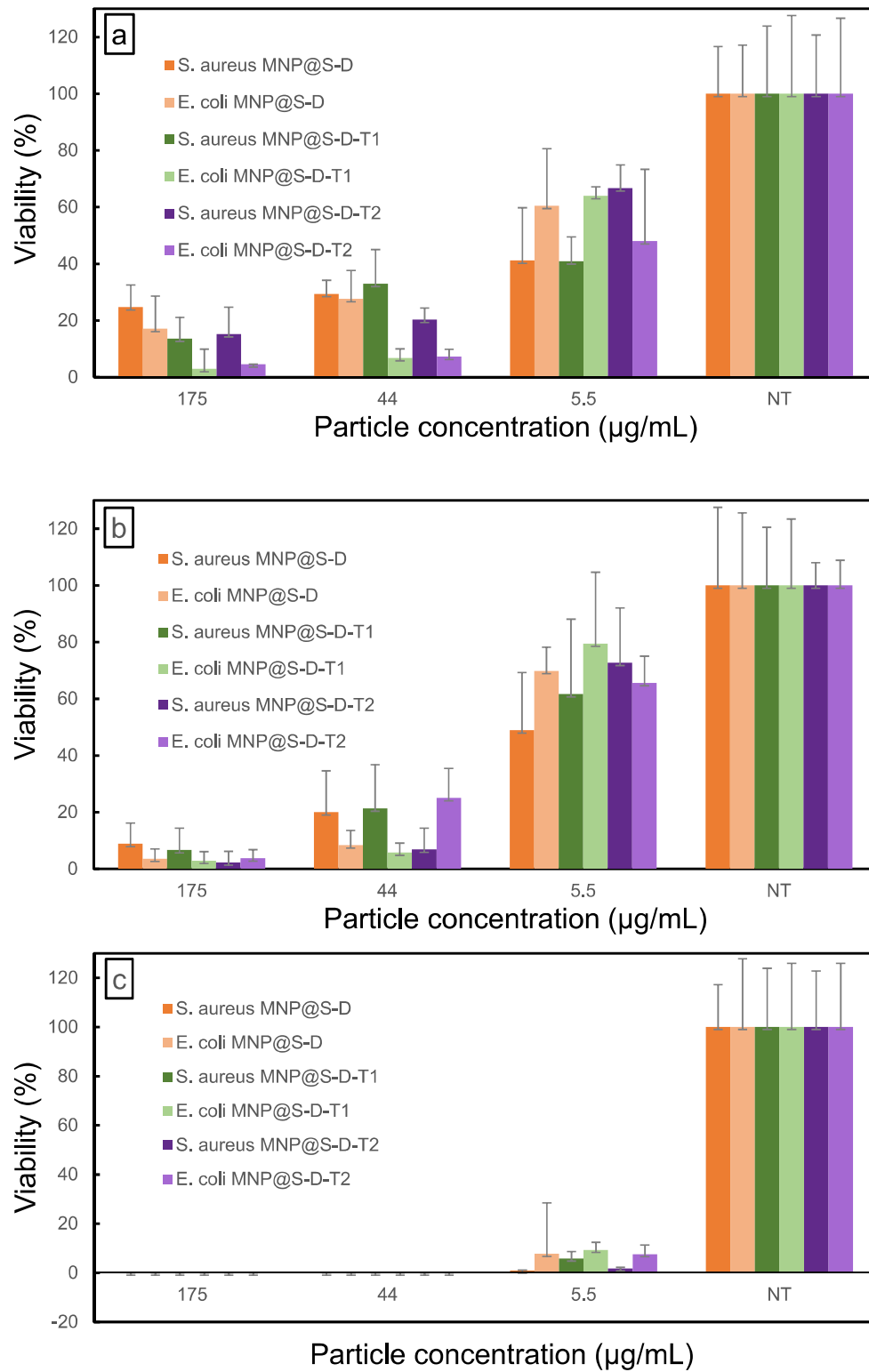
Figure 5. Viability of *S. aureus* and *E. coli* treated with MNP@S-D, MNP@S-D-T1, and MNP@S-D-T2 for (**a**) 0, (**b**) 1, and (**c**) 4 h. Culture without any treatment (NT) served as a negative control. Data are expressed as mean ± standard deviation of bacterial viability relative to control in three independent experiments. The results denoted significant differences at $p < 0.001$ (two-way ANOVA with Bonferroni's test).

4. Conclusions

Highly efficient antibacterial magnetic nanoparticles were prepared via a thermal decomposition that was followed by their modification with Sipomer PAM-200 and coating with PDMAEMA or P(DMAEMA-TBAEMA) obtained by radical (co)polymerization of 2-(dimethylamino)ethyl methacrylate and/or 2-tert-butylaminoethyl methacrylate. It is a great advantage of Sipomer PAM-200 that it consists of both phosphate group strongly interacting with iron oxide and methacrylate containing vinyl group prone to radical polymerization. The particles were uniform in size with diameters reaching 16 nm. Magnetic properties of the cationic polymer-coated nanoparticles clearly reflected their superparamagnetic character, without signs of clustering. As a result, the particles were easily attracted by even low external magnetic field. The antimicrobial effects of MNP@S-D, MNP@S-D-T1, and MNP@S-D-T2 against two different kinds of bacteria, *S. aureus* and *E. coli*, were found to be concentration- and time-dependent. Antibacterial properties were enhanced with increasing concentration of the nanoparticles and time of incubation. In particular, the MNP@S-D-T1 even at low concentrations (44 µg/mL) exhibited a strong antibacterial effect on both microbial cultures. This makes these particles suitable as an efficient and reusable antibacterial agent.

Author Contributions: Conceptualization, D.H. and A.B.S.; methodology, A.B.S.; validation, A.B.S. and D.H.; investigation, V.P., A.D., K.G., N.V. and E.P.; writing—original draft preparation, review and editing, D.H. and A.B.S.; visualization, J.H.; funding acquisition, D.H. All authors have read and agreed to the published version of the manuscript.

Data Availability Statement: All data are contained within the article.

Conflicts of Interest: The authors declare no conflict of interest.

Abbreviations

AAS	atomic absorption spectroscopy
B_c	coercive force
CFU	colony-forming units
Đ	dispersity
D_h	hydrodynamic diameter
DLS	dynamic light scattering
D_n	number-average diameter
D_w	weight-average diameter
HBSS	Hank's balanced salt solution
LA	Luria agar
LB	Luria broth
MNP	magnetic nanoparticles
MNP@S	MNP coated by Sipomer PAM-200
MNP@S-D	MNP coated by Sipomer PAM-200 and modified with poly[2-(dimethylamino)ethyl methacrylate]
MNP@S-D-T1	MNP coated by Sipomer PAM-200 and modified with 2-(dimethylamino)ethyl methacrylate and 2-*tert*-butylaminoethyl methacrylate copolymer (0.75:0.25 mol/mol)
MNP@S-D-T2	MNP coated by Sipomer PAM-200 and modified with 2-(dimethylamino)ethyl methacrylate and 2-*tert*-butylaminoethyl methacrylate copolymer (0.5:0.5 mol/mol)
M_s	saturation magnetization
M_{rs}	remanent saturation magnetization
OA	oleic acid
OD	octadec-1-ene
PD	polydispersity
PDMAEMA	poly[2-(dimethylamino)ethyl methacrylate]
PTBAEMA	poly(2-*tert*-butylaminoethyl methacrylate)
TEM	transmission electron microscope

References

1. Aslam, B.; Wang, W.; Arshad, M.I.; Khurshid, M.; Muzammil, S.; Rasool, M.H.; Nisar, M.A.; Alvi, R.F.; Aslam, M.A.; Qamar, M.U.; et al. Antibiotic resistance: A rundown of a global crisis. *Infect. Drug Resist.* **2018**, *11*, 1645–1658.
2. Fair, R.J.; Tor, Y. Antibiotics and bacterial resistance in the 21st century, perspectives in medicinal chemistry. *Perspect. Medicin. Chem.* **2014**, *6*, 25–64.
3. Hoffman, S.J.; Caleo, G.M.; Daulaire, N.; Elbe, S.; Matsoso, P.; Mossialos, E.; Rizvig, Z.; Røttingenh, J.A. Strategies for achieving global collective action on antimicrobial resistence. *Bull. World Health Organ.* **2015**, *93*, 867–876. [PubMed]
4. Guo, N.; Cang, F.; Wang, Z.; Zhao, T.; Song, X.; Farris, S.; Li, Y.; Fu, Y. Magnetism and NIR dual-response polypyrrole-coated Fe$_3$O$_4$ nanoparticles for bacteria removal and inactivation. *Mater. Sci. Eng. C Mater. Biol. Appl.* **2021**, *126*, 112143.
5. Fatima, F.; Siddiqui, S.; Khan, W.A. Nanoparticles as novel emerging therapeutic antibacterial agents in the antibiotics resistant era. *Biol. Trace Elem. Res.* **2021**, *199*, 2552–2564.
6. Raza, S.; Matuła, K.; Karoń, S.; Paczesny, J. Resistance and adaptation of bacteria to non-antibiotic antibacterial agents: Physical stressors, nanoparticles, and bacteriophages. *Antibiotics* **2021**, *10*, 435.
7. Wang, L.; Hu, C.; Shao, L. The antimicrobial activity of nanoparticles: Present situation and prospects for the future. *Int. J. Nanomed.* **2017**, *12*, 1227–1249.
8. De, M.; Ghosh, P.S.; Rotello, V.M. Applications of nanoparticles in biology. *Adv. Mater.* **2008**, *20*, 4225–4241.
9. Gupta, A.K.; Naregalkar, R.R.; Vaidya, V.D.; Gupta, M. Recent advances on surface engineering of magnetic iron oxide nanoparticles and their biomedical applications. *Nanomedicine* **2007**, *2*, 23–39. [PubMed]
10. Kostiv, U.; Farka, Z.; Mickert, M.J.; Gorris, H.H.; Velychkivska, N.; Pop-Georgievski, O.; Pastucha, M.; Odstrčilíková, E.; Skládal, P.; Horák, D. Versatile bioconjugation strategies of PEG-modified upconversion nanoparticles for bioanalytical applications. *Biomacromolecules* **2020**, *21*, 4502–4513. [PubMed]
11. Santos, S.; Ramalho, P.; Viana, A.T.; Lopes, A.R.; Gonçalves, A.G.; Nunes, O.C.; Pereira, F.R.; Soares, S. Feasibility of using magnetic nanoparticles in water disinfection. *J. Environ. Manag.* **2021**, *288*, 112410.
12. Armijo, L.M.; Jain, P.; Malagodi, A.; Fornelli, Z.; Hayat, A.; Rivera, A.C.; French, M.; Smyth, H.; Osiński, M. Inhibition of bacterial growth by iron oxide nanoparticles with and without attached drug: Have we conquered the antibiotic resistance problem? *Proc. SPIE* **2015**, *9338*, 93381Q.
13. De Toledo, L.A.S.; Rosseto, H.C.; Bruschi, M.L. Iron oxide magnetic nanoparticles as antimicrobials for therapeutics. *Pharm. Dev. Technol.* **2017**, *23*, 316–323.
14. Portet, D.; Denizot, B.; Rump, E.; Lejeune, J.-J.; Jallet, P. Nonpolymeric coatings of iron oxide colloids for biological use as magnetic resonance imaging contrast agents. *J. Colloid Interface Sci.* **2001**, *238*, 37–42. [CrossRef]
15. Konefał, M.; Černoch, P.; Patsula, V.; Pavlova, E.; Dybal, J.; Załeski, K.; Zhigunov, A. Enhanced ordering of block copolymer thin films upon addition of magnetic nanoparticles. *ACS Appl. Mater. Interfaces* **2021**, *13*, 9195–9205. [CrossRef] [PubMed]
16. Tocchio, A.; Horák, D.; Babič, M.; Trchová, M.; Veverka, M.; Beneš, M.J.; Šlouf, M.; Fojtík, A. Magnetic poly(glycidyl metha-crylate) particles prepared in the presence of surface-modified γ-Fe$_2$O$_3$. *J. Polym. Sci. A* **2009**, *47*, 4982–4994.
17. Jain, A.; Duvvuri, L.S.; Farah, S.; Beyth, N.; Domb, A.J.; Khan, W. Antimicrobial polymers. *Adv. Healthc. Mater.* **2014**, *3*, 1969–1985.
18. Milovic, N.M.; Wang, J.; Lewis, K.; Klibanov, A.M. Immobilized *N*-alkylated polyethylenimine avidly kills bacteria by rupturing cell membranes with no resistance developed. *Biotechnol. Bioeng.* **2005**, *90*, 715–722.
19. Timofeeva, L.; Kleshcheva, N. Antimicrobial polymers: Mechanism of action, factors of activity, and applications. *Appl. Microbiol. Biotechnol.* **2011**, *89*, 475–492. [PubMed]
20. Cerichelli, G.; La Mesa, C.; Luchetti, L.; Mancini, G. Role of counterions in the catalytic activity and phase equilibria of phosphonium salts in water. *Langmuir* **2000**, *16*, 166–171.
21. Hugues, C.; Bessy, C.; Bartolomeo, P.; Margaillan, A. Complexation of an acrylic resin by tertiary amines: Synthesis and chara-cterisation of new binders for antifouling paints. *Eur. Polym. J.* **2003**, *39*, 319–326. [CrossRef]
22. Kanazawa, A.; Ikeda, T. Multifunctional tetracoordinate phosphorus species with high self-organizing ability. *Coord. Chem. Rev.* **2000**, *198*, 117–131. [CrossRef]
23. Li, G.; Shen, J.; Zhu, Y. A study of pyridinium-type functional polymers. III. Preparation and characterization of insoluble pyridinium-type polymers. *J. Appl. Polym. Sci.* **2000**, *78*, 668–675. [CrossRef]
24. Nurdin, N.; Helary, G.; Sauvet, G. Biocidal polymers active by contact. III. Ageing of biocidal polyurethane coatings in water. *J. Appl. Polym. Sci.* **1993**, *50*, 671–678. [CrossRef]
25. Rawlinson, L.B.; Ryan, S.M.; Mantovani, G.; Syrett, J.A.; Haddleton, D.M.; Brayden, D.J. Antibacterial effects of poly(2-(dimethylamino ethyl)methacrylate) against selected Gram-positive and Gram-negative bacteria. *Biomacromolecules* **2010**, *11*, 443–453. [CrossRef] [PubMed]
26. Ward, M.; Sanchez, M.; Elasri, M.O.; Lowe, A.B. Antimicrobial activity of statistical polymethacrylic sulfopropylbetaines against Gram-positive and Gram-negative bacteria. *J. Appl. Polym. Sci.* **2006**, *101*, 1036–1041. [CrossRef]
27. Yancheva, E.; Paneva, D.; Maximova, V.; Mespouille, L.; Dubois, P.; Manolova, N.; Rashkov, I. Polyelectrolyte complexes between (cross-linked) *N*-carboxyethylchitosan and (quaternized) poly[2-(dimethylamino)ethyl methacrylate]: Preparation, cha-racterization, and antibacterial properties. *Biomacromolecules* **2007**, *8*, 976–984. [CrossRef] [PubMed]
28. Gu, Z.; Yuan, Y.; He, J.; Zhang, M.; Ni, P. Facile approach for DNA encapsulation in functional polyion complex for triggered intracellular gene delivery: Design, synthesis, and mechanism. *Langmuir* **2009**, *25*, 5199–5208. [CrossRef] [PubMed]

29. Keely, S.; Ryan, S.M.; Haddleton, D.M.; Limer, A.; Mantovani, G.; Murphy, E.P.; Colgan, S.P.; Brayden, D.J. Dexamethasone–pDMAEMA polymeric conjugates reduce inflammatory biomarkers in human intestinal epithelial monolayers. *J. Control. Release* **2009**, *135*, 35–43. [CrossRef]

30. Zhu, S.; Yang, N.; Zhang, D. Poly(*N,N*-dimethylaminoethyl methacrylate) modification of activated carbon for copper ions removal. *Mater. Chem. Phys.* **2009**, *113*, 784–789. [CrossRef]

31. Kusumo, A.; Bombalski, L.; Lin, Q.; Matyjaszewski, K.; Schneider, J.W.; Tilton, R.D. High capacity, charge-selective protein uptake by polyelectrolyte brushes. *Langmuir* **2007**, *23*, 4448–4454. [CrossRef]

32. Geng, Q.R.; Xiao, J.G.; Yang, B.; Wang, T.; Du, J.Z. Rationally engineering dual missions in one statistical copolymer nanocapsule: Bacterial inhibition and polycyclic aromatic hydrocarbon capturing. *ACS Macro Lett.* **2015**, *4*, 511–515. [CrossRef]

33. Lenoir, S.; Pagnoulle, C.; Galleni, M.; Compere, P.; Jerome, R.; Detrembleur, C. Polyolefin matrixes with permanent antibacterial activity: Preparation, antibacterial activity, and action mode of the active species. *Biomacromolecules* **2006**, *7*, 2291–2296. [CrossRef] [PubMed]

34. Zuo, H.; Wu, D.; Fu, R. Preparation of antibacterial poly(methyl methacrylate) by solution blending with water-insoluble antibacterial agent poly[(*tert*-buty1amino) ethyl methacrylate]. *J. Appl. Polym. Sci.* **2012**, *125*, 3537–3544. [CrossRef]

35. Huang, C.-L.; Lee, K.-M.; Liu, Z.-X.; Lai, R.-Y.; Chen, C.-K.; Chen, W.-C.; Hsu, J.-F. Antimicrobial activity of electrospun polyvinyl alcohol nanofibers filled with poly[2-(*tert*-butylaminoethyl) methacrylate]-grafted graphene oxide nanosheets. *Polymers* **2020**, *12*, 1449. [CrossRef] [PubMed]

36. Patsula, V.; Petrovský, E.; Kovářová, J.; Konefal, R.; Horák, D. Monodisperse superparamagnetic nanoparticles by thermolysis of Fe(III) oleate and mandelate complexes. *Colloid Polym. Sci.* **2014**, *292*, 2097–2110. [CrossRef]

37. Patsula, V.; Horák, D.; Kučka, J.; Macková, H.; Lobaz, V.; Francová, P.; Herynek, V.; Heizer, T.; Páral, P.; Šefc, L. Synthesis and modification of uniform PEG-neridronate-modified magnetic nanoparticles determines prolonged blood circulation and biodistribution in a mouse preclinical model. *Sci Rep.* **2019**, *9*, 10765. [CrossRef]

38. Shatan, A.B.; Venclíková, K.; Zasońska, B.A.; Patsula, V.; Pop-Georgievski, O.; Petrovský, E.; Horák, D. Antibacterial silver-conjugated magnetic nanoparticles: Design, synthesis and bactericidal effect. *Pharm. Res.* **2019**, *36*, 147. [CrossRef]

39. Patsula, V.; Moskvin, M.; Dutz, S.; Horák, D. Size-dependent magnetic properties of iron oxide nanoparticles. *J. Phys. Chem. Solids.* **2016**, *88*, 24–30. [CrossRef]

40. Patsula, V.; Kosinová, L.; Lovrić, M.; Ferhatovic Hamzić, L.; Rabyk, M.; Konefal, R.; Paruzel, A.; Šlouf, M.; Herynek, V.; Gajović, S.; et al. Superparamagnetic Fe_3O_4 nanoparticles: Synthesis by thermal decomposition of iron(III) glucuronate and application in magnetic resonance imaging. *ACS Appl. Mater. Interfaces* **2016**, *8*, 7238–7247. [CrossRef] [PubMed]

41. Thomassin, J.-M.; Lenoir, S.; Riga, J.; Jérôme, J.; Detrembleur, C. Grafting of poly[2-(*tert*-butylamino)ethyl methacrylate] onto polypropylene by reactive blending and antibacterial activity of the copolymer. *Biomacromolecules* **2007**, *8*, 1171–1177. [CrossRef] [PubMed]

42. Horák, D. Magnetic nano and microparticles in life sciences and medical imaging. In *Magnetic Nanoheterostructures: Diagnostic, Imaging and Treatment*; Sharma, S.K., Javed, Y., Eds.; Springer Nature: Cham, Switzerland, 2020; pp. 161–221.

43. Lee, J.S.; Cha, J.M.; Yoon, J.Y.; Lee, J.-K.; Kim, Y.K. Magnetic multi-granule nanoclusters: A model system that exhibits universal size effect of magnetic coercivity. *Sci. Rep.* **2015**, *5*, 12135.

44. Li, Q.; Kartikowati, C.W.; Horie, S.; Ogi, T.; Iwaki, T.; Okuyama, K. Correlation between particle size/domain structure and magnetic properties of highly crystalline Fe_3O_4 nanoparticles. *Sci. Rep.* **2017**, *7*, 9894. [CrossRef] [PubMed]

45. Chen, C.-K.; Lee, M.-C.; Lin, Z.-I.; Lee, C.-A.; Tung, Y.-C.; Lou, C.-W.; Law, W.-C.; Chen, N.-T.; Lin, K.-Y.A.; Lin, J.H. Intensifying the antimicrobial activity of poly[2-(*tert*-butylamino)ethyl methacrylate]/polylactide composites by tailoring their chemical and physical structures. *Mol. Pharm.* **2019**, *16*, 709–723. [CrossRef]

46. Fu, Y.; Wang, Y.; Huang, L.; Xiao, S.; Chen, F.; Fan, P.; Yang, J. Salt-responsive "killing and release" antibacterial surfaces of mixed polymer brushes. *Ind. Eng. Chem. Res.* **2018**, *57*, 8938–8945. [CrossRef]

Publication No. 3

Silver-Sulfamethazine-Conjugated β-Cyclodextrin/Dextran-Coated Magnetic Nanoparticles for Pathogen Inhibition

Anastasiia B. Shatan [1,2] , Vitalii Patsula [1], Hana Macková [1], Andrii Mahun [1,2], Renáta Lehotská [3], Elena Piecková [3] and Daniel Horák [1,*]

1   Institute of Macromolecular Chemistry, Czech Academy of Sciences, Heyrovského nám. 2,
     162 00 Prague 6, Czech Republic; shatan@imc.cas.cz (A.B.S.); patsula@imc.cas.cz (V.P.);
     mackova@imc.cas.cz (H.M.); mahun@imc.cas.cz (A.M.)
2   Department of Physical and Macromolecular Chemistry, Faculty of Science, Charles University, Hlavova 8,
     128 00 Prague 2, Czech Republic
3   Institute of Microbiology, Faculty of Medicine, Slovak Medical University in Bratislava, Limbová 12,
     83 303 Bratislava, Slovakia; renata.lehotska@szu.sk (R.L.); elena.pieckova@szu.sk (E.P.)
*   Correspondence: horak@imc.cas.cz

Abstract: In the fight against antibiotic resistance, which is rising to dangerously high levels worldwide, new strategies based on antibiotic-conjugated biocompatible polymers bound to magnetic nanoparticles that allow the drug to be manipulated and delivered to a specific target are being proposed. Here, we report the direct surface engineering of nontoxic iron oxide nanoparticles (IONs) using biocompatible dextran (Dex) covalently linked to β-cyclodextrin (β-CD) with the ability to form non-covalent complexes with silver-sulfamethazine (SMT-Ag). To achieve a good interaction of β-CD-modified dextran with the surface of the nanoparticles, it was functionalized with diphosphonic acid (DPA) that provides strong binding to Fe atoms. The synthesized polymers and nanoparticles were characterized by various methods, such as nuclear magnetic resonance (NMR), Fourier transform infrared (FTIR) and ultraviolet–visible (UV–Vis) spectroscopies, transmission electron microscopy (TEM), thermogravimetric analysis (TGA), atomic absorption spectroscopy (AAS), dynamic light scattering (DLS), etc. The resulting magnetic ION@DPA-Dex-β-CD-SMT-Ag nanoparticles were colloidally stable in water and contained 24 μg of antibiotic per mg of the particles. When tested for in vitro antimicrobial activity on Gram-positive (*Staphylococcus aureus*) and Gram-negative (*Escherichia coli*) bacteria and fungi (yeast *Candida albicans* and mold *Aspergillus niger*), the particles showed promising potential.

Keywords: superparamagnetic iron oxide nanoparticles; β-cyclodextrin; silver-sulfamethazine; antimicrobial activity

1. Introduction

Since the 1940s when antibiotics were first introduced to treat serious infections, they have achieved widespread use and saved millions of lives [1]. Among antibiotics, sulfonamides, such as sulfamethazine (SMT) derivatives, play an important role thanks to their broad spectrum of activity and low cost [2,3]. They are widely used in human medicine, as well as in animal production, to treat various bacterial infections of the soft tissues, urinary tract, lungs, ears and skin without noticeable toxicity to the tissues [4]. Their bacteriostatic activity is based on a competition with p-aminobenzoic acid, which is involved in the enzymatic synthesis of dihydrofolic acid. However, bacteria and other microorganisms have developed resistance to antibiotics, and this resistance is on the rise, prompting the need for new approaches using nanomedicine that can deliver antimicrobial agents precisely to a specific site, thereby minimizing their adverse effects [5].

A number of nanomaterials have been proposed for the delivery of biologically active agents to the required sites of action. In particular, superparamagnetic iron oxide nanopar-

ticles (IONs) have shown considerable potential [6]; for example, they have been used as anticancer or contrast agents in magnetic resonance imaging [7]. Their key advantage consists in magnetic field targeting, which allows high doses to be delivered, increasing the chances of successful treatment while reducing side effects. The functioning of IONs is dependent on many factors, such as shape, size, large surface-to-volume ratio, and the presence of reactive functional groups allowing the binding of various biological substances in sufficient quantities while maintaining colloidal stability. Colloidal stability in aqueous media is usually achieved by coating the IONs with various inorganic (silica) or synthetic organic polymers, such as poly(vinyl alcohol) and poly(ethylene glycol), as well as biopolymers like poly(*L*-lysin), dextran, chitosan, etc. [8]. Among these, dextran is the preferred choice for ION coating due to its biocompatibility, non-toxicity, degradability and the fact that it was FDA-approved for this purpose [9]. In addition, dextran is easily modifiable by tosylation, and various bioactive molecules can be bound by subsequent nucleophilic displacement reactions [10–12]. IONs have also been functionalized with β-cyclodextrin (β-CD), which belongs to a class of macrocycles consisting of seven glucose units, in order to remove pharmaceutical residues from water [13], remove cancer biomarkers from urine [14] or deliver hydrophobic drugs [15]. It is an advantage of β-CD that it is reactive towards biomolecules in aqueous media under mild conditions, preferably in combination with divinyl sulfone. For example, β-CD was found to form glutathione-responsive nanoparticles loaded with lonidamine for the simultaneous delivery of anticancer drugs into cancer cells [16] or to produce a complex based on silica-coated or imprinted IONs for the separation and recovery of erythromycin or doxycycline from industrial wastewater [17,18]. At the same time, the ability of β-CD as a host to form various supramolecular structures and to encapsulate guest molecules, e.g., sulfamethazine (SMT), by complexation in internal hydrophobic cavity was exploited, thus increasing the solubility and bioavailability of poorly soluble molecules [19]. However, it should be noted that SMT has rather limited biocidal activity; for example, the minimum inhibitory concentration (MIC) against *Escherichia coli* bacteria is 250 μg/mL. In this respect, metal complexes of sulfonamides with higher antibacterial activity than free sulfamethazine are more promising, e.g., silver-sulfamethazine (SMT-Ag) has MIC = 100 μg/mL [4]. In addition, silver is known to exhibit extensive biocidal effects, including antiviral and antifungal [20], for example in dentistry [21]. There are a number of methods to synthesize Ag nanoparticles, including laser ablation, irradiation, evaporation and condensation, lithography, microwave-assisted and green synthesis (from plants or microorganisms), polyol, photochemical and microemulsion methods and even electrodeposition [22].

The aim of this report was to design and synthesize new magnetic IONs coated with dextran and β-cyclodextrin as carriers of the SMT-Ag antibiotic for targeted pathogen inhibition. The in vitro antibacterial/antifungal activity of the newly synthesized nanoparticles was tested by standardized methods according to the European Committee on Antimicrobial Susceptibility Testing (EUCAST).

2. Experimental Procedures

2.1. Chemicals and Materials

FeCl$_2$·4H$_2$O, FeCl$_3$·6H$_2$O, β-cyclodextrin (β-CD), sulfamethazine (SMT), divinyl sulfone (DVS), 4-toluenesulfonyl chloride (TsCl), 4-toluenesulfonic acid monohydrate (TsOH), ethanolamine (EA), lithium chloride and dextran (M_w = 70 kDa) were purchased from Sigma-Aldrich (St. Louis, MO, USA). Hydrochloric acid (35%), sodium hydroxide, ammonium chloride, ethanol, acetone, hexane, dichloromethane (DCM) and other solvents were obtained from Lach-Ner (Neratovice, Czech Republic). Dimethylacetamide (DMAc) was purchased from Fluka (Buchs, Switzerland) and distilled before use. Vinylidene 1,1-diphosphonic acid (VDPA) was prepared as previously reported [23]. Silver-sulfamethazine (SMT-Ag) was prepared according to a previous publication [4]. Ultrapure Q-water filtered on a Milli-Q Gradient A10 system (Millipore; Molsheim, France) was used in the experiments.

Bacteria *Staphylococcus aureus* CCM 2022 and *Escherichia coli* CCM 3954 were obtained from the collection of pathogenic microorganisms at the Slovak Medical University (SMU) in Bratislava, Slovakia. Ascomycetous fungi *Candida albicans* (CCM 8186; CA) and *Aspergillus niger* (AN; environmental isolate from the fungal collection) were from the Mycological laboratory of SMU.

2.2. Synthesis of 4-Toluenesulfonic Anhydride (Ts₂O) and 6-Toluenesulfonyl-β-Cyclodextrin (β-CD-Ts)

Ts$_2$O was prepared by modification of the previous procedure [24]. Briefly, a solution of TsCl (8 g; 42 mol) and TsOH H$_2$O (2 g; 11 mol) in DCM (50 mL) was stirred (600 rpm) at room temperature (RT) for 16 h and filtered through silica gel. After drying under vacuum (133 Pa), 5.8 g of Ts$_2$O (73% yield) was obtained; its structure was confirmed by ^{1}NMR spectroscopy by comparison with TsCl and TsOH (Supplementary Material; Figure S1).

A suspension of β-CD (5.75 g; 5 mmol; ^{1}H NMR spectrum is shown in Figure S2a) and Ts$_2$O (3.3 g; 10 mmol) in water (125 mL) was stirred at RT for 2 h, an aqueous 0.125 M NaOH solution (25 mL) was added, and, after 10 min, unreacted Ts$_2$O was removed by filtration through a nylon membrane filter (0.2 μm pores). NH$_4$Cl (6.7 g) was added to the filtrate, and its pH was adjusted to ~8. The resulting β-CD-Ts solution was cooled to 4 °C for 16 h, the precipitate was separated and washed with cold water and acetone. After drying under vacuum (133 Pa), a white β-CD-Ts powder was obtained; the structure of β-CD-Ts was confirmed by ^{1}H NMR (Figure S2b).

2.3. Synthesis of 6-Deoxy-6-Hydroxylethylamino-β-Cyclodextrin (β-CD-EA) and 6-Deoxy-6-(2-Hydroxyethyl) (Vinylsulfonyl)Methylamino-β-Cyclodextrin (β-CD-VS)

β-CD-EA and β-CD-VS were also prepared by modifying the earlier procedure [25]. AE (2.72 mL; 45 mmol) was added to a solution of β-CD-Ts (1.16 g; 0.9 mmol) in dimethyl-formamide (DMF; 10 mL), and the reaction mixture was stirred (600 rpm) at 80 °C for 48 h. Tetrahydrofuran (THF; 100 mL) was then added, and the resulting β-CD-EA precipitate was filtered, washed with THF (30 mL) and dried under vacuum (133 Pa); the structure of β-CD-EA was demonstrated by ^{1}H NMR and DOSY spectra (Figure S3a,c).

To a solution of β-CD-EA (1 g; 0.83 mmol) in water (8 mL) was added divinyl sulfone (0.2 mL; 2.07 mmol), and the reaction mixture was maintained at RT for 2 h. Next, THF (80 mL) was added, and the resulting β-CD-VS precipitate was filtered off, washed with THF (10 mL) and dried in vacuum; the structure of β-CD-VS was confirmed by ^{1}H NMR and DOSY spectra (Figure S3b,d).

2.4. Tosylation of Dextran and the Reaction of Dex-Ts with Ethanolamine (EA)

6-Toluenesulfonyl dextran (Dex-Ts) was prepared by modifying an earlier procedure [12]. Briefly, dextran (5 g) and anhydrous LiCl (3.0 g; 70.8 mmol) were dissolved in DMAc (125 mL) at 80 °C with stirring (600 rpm). Next, a solution of triethylamine (25.78 mL; 184.8 mmol) in DMAc (24 mL) and a solution of TsCl (17.62 g; 92.4 mmol) in DMAc (24 mL) were added dropwise at 8 °C; the mixture was allowed to react for 36 h with stirring (400 rpm). Dex-Ts was isolated by double precipitation in water (600 mL) and dried at RT under vacuum (133 Pa). The structure of Dex-Ts was proven by ^{1}H NMR (Figure S4a).

To a solution of Dex-Ts (3 g) in DMF (30 mL) was added EA (23.95 mL; 396 mmol), and the reaction mixture was stirred (600 rpm) at 90 °C for 48 h. 6-Deoxy-6-hydroxylethylaminodextran (Dex-EA) was isolated by double precipitation in THF (100 mL), purified on a Sephadex® G-25 column and lyophilized; the structure of Dex-EA was proven by ^{1}H NMR (Figure S4b).

2.5. Functionalization of Dex-EA with β-CD-VS and Modification with VDPA

First, Dex-β-CD was obtained by reacting an aqueous solution (10 mL) of Dex-EA (0.25 g; 1.19 mmol) with an aqueous solution (15 mL) of β-CD-VS (0.78 g; 0.6 mmol) under stirring at 37 °C for 24 h. Dex-β-CD was then dialyzed (MWCO = 12–14 kDa) against water for 72 h and lyophilized. Subsequently, an aqueous solution (1 mL) of VDPA (0.07 g;

0.38 mmol), whose pH was adjusted to 10.8 with 10 M NaOH, was added to an aqueous solution (8 mL) of Dex-β-CD (0.25 g), and the mixture was stirred (800 rpm) at 50 °C for 24 h. The resulting 1,1-diphosphonic acid-terminated β-cyclodextrin/dextran (DPA-Dex-β-CD) conjugate was purified on a Sefadex G-25 column with water as eluent; the pH was adjusted to 2 by the addition of 1 M HCl, purified once more and lyophilized. The successful functionalization of Dex-EA with β-CD-VS and modification with VDPA was confirmed by ^{1}H NMR (Figure S5a), ^{13}C NMR (Figures S5b and S6) and ^{13}C NMR spectra (Figure S7).

2.6. Synthesis of Iron Oxide Nanoparticles (IONs)

The iron oxide dispersion was prepared according to a previously published coprecipitation method [26]. Briefly, an aqueous solution of 0.2 M iron(III) chloride (100 mL) and 0.2 M iron(II) chloride (50 mL) was sonicated with 0.5 M aqueous NH_4OH (100 mL) for 5 min. The solution was then added to a 0.5 M aqueous NH_4OH solution (400 mL) and stirred (200 rpm) at RT for 1 h. Afterward, the resulting precipitate was separated using a magnet and washed repeatedly with water until peptization, during which colloidal nanoparticles were formed. Subsequently, the particles were sonicated with a 5 wt.% sodium hypochlorite solution (16 mL) for 5 min, and the resulting IONs were separated and washed as described above to a concentration of 42 mg per ml.

2.7. Complexation of ION@DPA-Dex-β-CD Nanoparticles with Silver-Sulfamethazine (SMT-Ag)

ION@DPA-Dex-β-CD particles were prepared by mixing an aqueous solution (4 mL) of DPA-Dex-β-CD conjugate (40 mg) with an aqueous dispersion of IONs (6 mL; 40 mg particles) under sonication, followed by stirring (800 rpm) at RT for 3 days. The resulting ION@DPA-Dex-β-CD particles were magnetically separated and washed with water three times (10 mL each) using centrifugation. The mixture of SMT-Ag (10 mg) in 0.06% NH_4OH (10 mL) was sonicated for 5 min and added; the whole mixture was stirred (800 rpm) at RT for 3 days, and the resulting ION@DPA-Dex-β-CD-SMT-Ag particles were washed as described above. IONs, ION@DPA-Dex-β-CD and ION@DPA-Dex-β-CD-SMT-Ag particles used in biological experiments were ultrasonically sterilized (Bandelin Sonopuls; Berlin, Germany; 20% power) for 2 min and diluted with aqua pro injection to 4 mg/mL in an MSC-Advantage biological safety cabinet (Thermo Fisher Scientific; Waltham, MA, USA).

To determine the SMT-Ag content in the nanoparticles, an aqueous dispersion (0.9 mL) of ION@DPA-Dex-β-CD-SMT-Ag particles (1 mg) was dissolved in 38% aqueous hydrofluoric acid (0.1 mL) with shaking for 30 min, the precipitated Ag was removed by centrifugation (14,100 rcf) for 20 min, the solution was optionally diluted with water and the absorbance was measured at 300 nm using an Evolution™ 220 UV–Vis spectrometer (Thermo Fisher Scientific; Waltham, MA USA); the absorbance was then compared with the calibration curve of a solution of pure SMT in 2% aqueous hydrofluoric acid. The reference sample was prepared as described above but with particles without SMT-Ag. The SMT-Ag loading efficiency (*LE*) was determined from the SMT-Ag content according to the following equation:

$$LE\ (\%) = m_{SMT\ encap} / m_{carrier\ total} \times 100 \qquad (1)$$

where $m_{SMT\ encap}$ is the mass of SMT-Ag in particles and $m_{carrier\ total}$ is the mass of ION@DPA-Dex-β-CD-SMT-Ag.

The solubility of SMT-Ag with or without β-CD in 0.06% NH_4OH was determined by UV–Vis spectroscopy. SMT-Ag (20 mg), optionally with β-CD (56 mg), was added to 0.06% NH_4OH (10 mL), and the mixture was sonicated for 3 min. The resulting dispersion was stirred vigorously at RT for 2 days, then centrifuged (6850 rcf) for 60 min and filtered through a 0.45 μm filter. The solution (0.9 mL) was mixed with 38% aqueous hydrofluoric acid solution (0.1 mL), diluted five times with water, and the absorbance was measured at 300 nm. The amount of dissolved antibiotic was determined from the SMT calibration curve in 2% aqueous hydrofluoric acid.

2.8. Physicochemical Characterization of Particles and Their Coatings

Transmission electron micrographs were taken on a Tecnai Spirit G2 transmission electron microscope (TEM; FEI; Brno, Czech Republic) at 120 kV to determine the number-average diameter ($D_n = \Sigma N_i \cdot D_i / \Sigma N_i$), weight-average diameter ($D_w = \Sigma N_i \cdot D_i^4 / \Sigma N_i \cdot D_i^3$) and dispersity ($Đ = D_w / D_n$) from at least 300 particles using Atlas software (Tescan Digital Microscopy Imaging; Brno, Czech Republic). Dynamic light scattering (DLS) was measured on a Zetasizer Ultra analyzer (Malvern Panalytical; Malvern, UK) to determine the hydrodynamic diameter (D_h), polydispersity (PD) and ζ-potential of the nanoparticles in water (pH = 5.6).

^{1}H, ^{13}C and ^{31}P NMR spectra were recorded using a Bruker Avance III 600 spectrometer at Larmor frequencies of $\nu(^1\text{H})$ = 600.2 MHz, $\nu(^{13}\text{C})$ = 150.9 MHz and $\nu(^{31}\text{P})$ = 242.9 MHz, respectively, and processed with Bruker TopSpin 4.1.1 software. The samples were dissolved either in DMSO-d6 or D$_2$O at 22 °C. ^{1}H NMR spectra were obtained using a 90° pulse (18 μs length) with a 10 s recycle delay and 16–64 number of scans. ^{1}H-^{1}H 2D nuclear Overhauser effect NMR spectra (NOESY) were recorded with a spectral window of 7200 Hz in both F1 and F2 frequency dimensions and with a mixing time of 500 ms. A total of 32 scans were accumulated over 512 t_1 increments with a relaxation delay of 10 s. The diffusion of the components in the samples was investigated by pulsed-field gradient NMR using a 2D diffusion-ordered spectroscopy (DOSY) with a DiffBB diffusion probehead and 40 A gradient amplifiers. A double-stimulated echo pulse sequence was used to measure the self-diffusion coefficients D obtained by least-squares fitting of the Stejskal–Tanner equation [27] using Bruker Dynamics center 2.6.1 software. Experiments were performed with a diffusion time of 50 ms, a gradient duration of 1 ms and a gradient strength varying in 8 steps with a maximum of 2 T/m. ^{13}C NMR spectra were recorded using a 90° pulse (10 μs length) with a 10 s recycle delay and 5–20 k number of scans. ^{31}P NMR spectra were obtained using a 90° excitatory pulse (18 μs length) with a 10 s recycle delay and 1024 scans. In the case of ^{13}C and ^{31}P NMR spectra, inverse-gated decoupling was used to remove heteronuclear interactions. ^{1}H and ^{13}C chemical shifts were calibrated using hexamethyldisiloxane (0.05 ppm from tetramethylsilane in ^{1}H NMR spectra and 2 ppm in ^{13}C NMR spectra) as an external standard. ^{31}P NMR chemical shift was calibrated using H$_3$PO$_4$ in D$_2$O (0 ppm) as an external standard.

FTIR spectra were acquired on a Perkin-Elmer Paragon 1000PC spectrometer (Waltham, MA, USA) using a Specac MKII Golden Gate single attenuated total reflection (ATR) system with a diamond crystal and a 45° angle of incidence.

The C, H, N and S contents in the polymers were determined using a FlashSmart™ elemental analyzer (Thermo Fisher Scientific; Waltham, MA, USA). The phosphorus content in the polymer was determined after its digestion in a HClO$_4$/HNO$_3$ mixture in a Biotage Initiator microwave reactor (Biotage AB; Uppsala, Sweden) in the presence of sulfuric acid, ammonium molybdate, ascorbic acid and potassium antimony tartrate. Spectra were recorded on a Libra S22 UV–Vis spectrophotometer (Biochrom; Cambridge, UK) at 690 nm; calibration with KH$_2$PO$_4$.

2.9. Disc Diffusion Test (DDT) for Qualitative Antibmicrobial Evaluation

Briefly, sterile filter paper discs (5 or 10 mm diameter; Whatmann, Bio-Rad; Hercules, CA USA) were loaded with stock dispersions of IONs, ION@DPA-Dex-β-CD and ION@DPA-Dex-β-CD-SMT-Ag particles (10 or 30 μL; 4 mg/mL) to achieve the desired concentration per disc (40 or 120 μg) and dried at RT. Pure colonies of Gram-positive *S. aureus* and Gram-negative *E. coli* strains isolated from fresh growth were transferred into sterile saline and vortexed to form a homogeneous bacterial suspension according to the protocol recommended by EUCAST [28]. The optical density (OD) was then adjusted to a 0.5 McFarland standard and used as an inoculum suspension.

The same protocol was used for *C. albicans* as for bacterial strains. A 24 h yeast culture was transferred into sterile saline and vortexed to form a homogeneous suspension. The OD of suspension was then adjusted to 0.5 McFarland, and the suspension was diluted

with sterile saline 1:10 v/v and used as a standardized inoculum. For the fungal strain, a modified protocol described previously was followed [29].

A. niger was subcultured on a Sabouraud dextrose agar plate (HiMedia; Mumbai, India) at 37 °C for 7 days. After culture growth, conidia were harvested in a sterile saline solution with 0.1% Tween 80. The purity of the conidial suspension was checked under a microscope to ensure that no hyphae were present and then adjusted to OD = 0.5 McFarland. Another conidial suspension was diluted 1:10 v/v with sterile saline with 0.1% Tween 80 and used as a standardized inoculum suspension.

Standardized inoculum suspensions were swabbed evenly over Mueller–Hinton agar (MHA) plates (Oxoid; Basingstoke, UK). The prepared discs were fixed in triplicates on the surface of the inoculated agar plate within 15 min of inoculation. In the case of ION@DPA-Dex-β-CD-SMT-Ag, a 10 μL drop of undiluted solution was dropped onto the plate with each tested microorganism. Finally, inhibition zone diameters (mm) and growth in the droplet were checked after static incubation at 37 °C for 24 h for bacteria and candida or up to 72 h for *A. niger*.

2.10. Minimum Inhibitory and Minimum Bactericidal/Microbicidal Concentrations (MIC and MBC/MMC)

According to EUCAST recommendations, the international ISO 20776-1 standard was followed. A quantitative microdilution broth assay was used to investigate antimicrobial susceptibility against *S. aureus* for all three test substances—IONs, ION@DPA-Dex-β-CD and ION@DPA-Dex-β-CD-SMT-Ag. The MIC of ION@DPA-Dex-β-CD-SMT-Ag was also tested with *E. coli*, *C. albicans* and *A. niger*. Briefly, 96 flat-bottom microtiter plates for tissue cultures were used, and the tests were performed in parallel. A set of particle concentrations of 1500–2.5 μg/mL (1500, 1000, 500, 250, 125, 50, 25, 12.5, 5 and 2.5 μg/mL) was prepared by diluting the stock solution with Mueller–Hinton broth (Oxoid) and pipetted into the respective wells. Positive control (growth) consisted of culture solution in the absence of an antimicrobial agent and with microbial inoculum. Negative control (growth) consisted of dilution solutions without culture broth in the presence of microbial inoculum. After inoculation with the standardized suspension of the microorganism, the plates were incubated at 37 °C for 18 h. The microbial growth on the plates was evaluated by the naked eye, and the lowest concentration of antimicrobial agent expressed in μg/mL, which visibly inhibited the growth of the microorganism in both parallel experiments, was recorded as MIC. The viability of the inoculum was checked according to the method used.

After MIC determination, MBC/MMC was evaluated according to the following procedure. For each concentration from the MIC test for which no growth was observed in the parallel wells, 10 μL of the solution from both wells was inoculated onto MHA plates and incubated at 37 °C for an additional 24 h. If no growth was observed in both parallel drops, the corresponding concentration was read as MBC/MMC.

3. Results and Discussion

3.1. Iron Oxide Nanoparticles (IONs)

The IONs were synthesized by the precipitation of iron(II) and (III) chlorides with ammonium hydroxide, which is a frequently used method for the preparation of magnetic nanoparticles [26,30]. It is supposed that the resulting product consisted predominantly of magnetite, which is not very stable and may undergo uncontrolled oxidation to other forms of iron oxide, including non-magnetic hematite. In order to prevent the uncontrolled oxidation of magnetite, its controlled oxidation to maghemite using sodium hypochlorite was carried out. Such IONs have the advantage of superparamagnetism, which means that they respond to an external magnetic field but do not retain residual magnetism when the magnetic field is removed, and therefore do not agglomerate and are readily dispersible in aqueous media [31]. Superparamagnetism of IONs is then advantageously used in many biomedical applications [32]. The morphology of IONs in a dry state was investigated by TEM (Figure 1), which revealed particle aggregates formed during sample preparation

involving drop casting and drying. The aggregates consisted of primary particles with a shape close to spherical, with an average size of $D_n = 8 \pm 2$ nm and dispersity $Đ = 1.29$, indicating a moderately broad size distribution. In addition to TEM analysis of the dry particles, the aqueous dispersion of IONs was investigated by DLS, which revealed a hydrodynamic diameter $D_h = 108 \pm 1$ nm and a polydispersity $PD = 0.13$. A larger D_h than D_n is common for ION colloids not only because of partial aggregation but also because the particles are surrounded by an electrical double layer and DLS measures an intensity-weighted z-average diameter sensitive to large objects. DLS is also used to measure the ξ-potential, which reached -26 ± 5 mV; the negative ξ-potential is typical for particles prepared by coprecipitation of $FeCl_2$ and $FeCl_3$ with a base [33]. Such a value of the ξ-potential ensures the colloidal stability of the IONs in water [34]. According to the TGA of neat IONs, 3.1 wt.% of the total weight loss could be attributed to the evaporation of residual water.
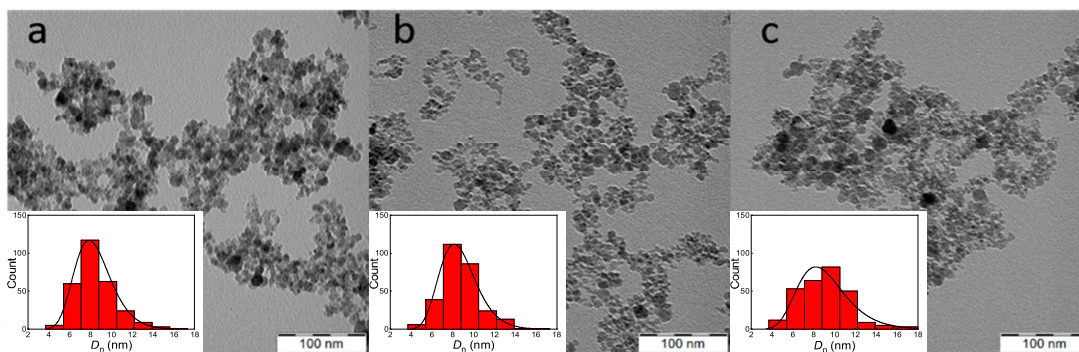
Figure 1. TEM micrographs of (**a**) IONs, (**b**) ION@DPA-Dex-β-CD and (**c**) ION@DPA-Dex-β-CD-SMT-Ag particles.

3.2. Modification of Dex and β-CD

Because SMT-Ag has limited solubility in water, it cannot be directly used in vivo, and it is necessary to incorporate it into a hydrophilic carrier suitable for bioapplications. β-CD was chosen as the carrier of SMT-Ag in this work because it has a hydrophobic pocket into which the SMT can be easily loaded. The disadvantage of this system, however, is its low molar mass and therefore possible rapid renal clearance combined with non-specific targeting. Therefore, β-CD was bound to hydrophilic Dex containing diphosphonate anchoring groups capable of complexation with IONs. Dex is a biocompatible, biodegradable, non-toxic and non-immunogenic polymer [35], making it a promising platform for the design of biosafe particles that are colloidally stable in water and body fluids.

The synthesis of a reactive β-CD derivative, 6-deoxy-6-(2-hydroxyethyl) (vinylsulfonyl) methylamino-β-cyclodextrin (β-CD-VS), proceeded by a three-step process consisting of (*i*) tosylation of β-CD with p-toluenesulfonic anhydride (Ts$_2$O) in water followed by treatment with 10% aqueous NaOH solution; (*ii*) the reaction of 6-*O*-monotosyl-6-β-cyclodextrin (β-CD-Ts) with EA (1/50 mol/mol) in DMF to form mono-6-(2-hydroxyethyl)amino-β-cyclodextrin (β-CD-EA) and (*iii*) the introduction of reactive vinyl groups by an aza-Michael reaction with DVS to form β-CD-VS (Figure 2). Simultaneously, the reaction of Dex with TsCl formed Dex-Ts, whose Ts groups were subsequently exchanged with ethanolamine to form Dex-EA, which was then reacted with the double bond of β-CD-VS, resulting in Dex-β-CD (Figure 3). Dex-β-CD finally reacted with VDPA to form DPA-Dex-β-CD.
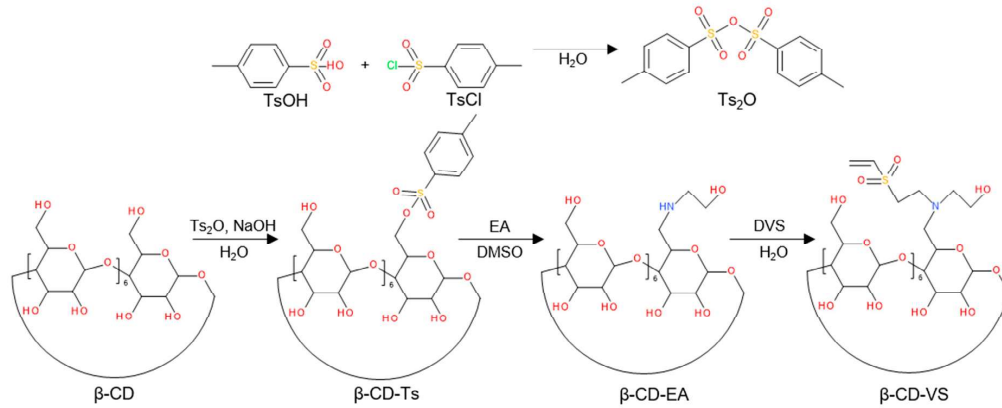
Figure 2. Synthesis of 4-toluenesulfonic anhydride (Ts₂O) and three-step modification of β-cyclodextrin (β-CD) to yield 6-deoxy-6-(2-hydroxyethyl) (vinylsulfonyl)methylamino-β-cyclodextrin (β-CD-VS); EA—ethanolamine, DMSO—dimethyl sulfoxide, DVS—divinyl sulfone.
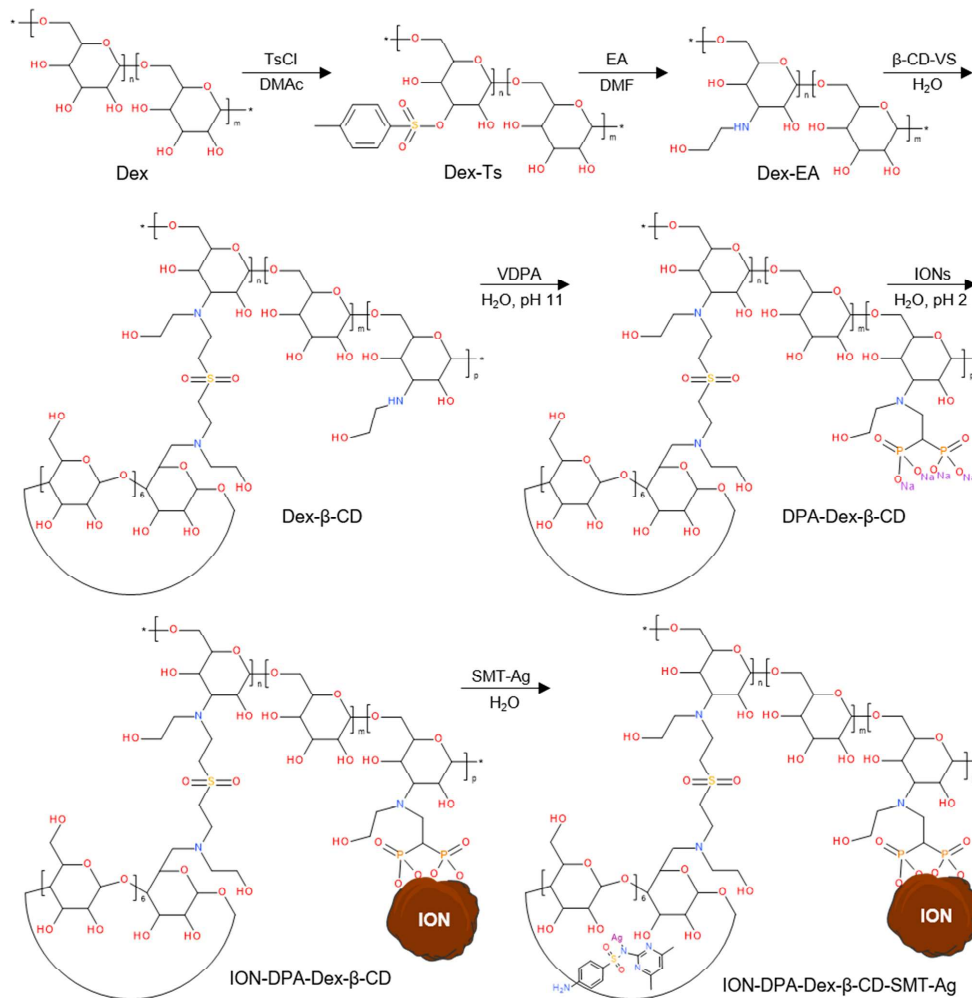

Figure 3. Modification of dextran with tosyl chloride (TsCl), ethanolamine (EA), 6-deoxy-6-(2-hydroxyethyl) (vinylsulfonyl)methylamino-β-cyclodextrin (β-CD-VS) and vinylidene 1,1-diphosphonic acid (VDPA) and conjugation of silver-sulfamethazine (SMT-Ag) to form silver-sulfamethazine-conjugated β-cyclodextrin/dextran-coated iron oxide nanoparticle (ION); DMAc—dimethylacetamide.

The structure of the individual components was confirmed by ^{1}H, ^{13}C and ^{31}P NMR spectra. For example, the ^{1}H NMR spectrum of Dex-Ts displayed signals corresponding to the α-1,6 glucose units of Dex, as well as signals of the tosyl groups bound to the Dex chains (Figure S4a). By comparing the integral signal intensity from the C1 proton of Dex with the signals from the aromatic protons of the tosyl groups, it was found that, on average, 72% of the glucose subunits of Dex have one -OH group substituted by a tosyl group. In addition, the structure of the Dex-EA was analyzed from the respective ^{1}H and ^{13}C NMR spectra (Figures S4b and S8). The almost complete substitution of Ts groups by EA was confirmed by a considerable decrease of NMR signals corresponding to Ts; only relatively small signals indicated residual Ts (~7% of glucose subunits of Dex still had adjacent Ts groups). In turn, signals from EA were clearly visible in the corresponding ^{13}C NMR spectrum (Figure S8; signals marked as "7" and "8"); based on the relative intensity of these signals, ~65% of glucose units in Dex were modified with EA. In the case of the ^{1}H NMR spectrum of β-CD, its structure was confirmed by signals typical of glucose subunits linked by α-1,4 glycosidic bonds (Figure S2a), which was in agreement with the literature [36]. The modification of β-CD by Ts$_2$O was confirmed by the presence of NMR signals corresponding to methyl and aromatic protons from Ts marked as "9", "8" and "7" (Figure S2b). In addition, the signals corresponding to the β-CD rings were broadened, which can be attributed to the change in β-CD solubility. Comparison of the integral NMR signal intensities from the C1 proton with those from Ts showed that, on average, one hydroxyl group of the β-CD ring was substituted by tosyl. To additionally confirm the chemical binding of Ts to β-CD, 2D NOESY and DOSY NMR spectra were recorded (Figure S2c,d). The NOESY spectrum showed cross-peaks (highlighted by the grey boxes in Figure S2d), indicating the close spatial proximity of the Ts groups and the β-CD rings and thus their chemical binding. In addition, diffusion NMR measurements revealed that both parts of the β-CD-Ts had similar values of the self-diffusion coefficient (D = ~1 × 10^{-10} m^2/s), further confirming that they are chemically bound (Figure S2c).

Furthermore, the substitution of Ts groups of β-CD-Ts by EA was confirmed in the same way as in the case of Dex, i.e., from ^{1}H and ^{13}C NMR spectra (Figures S3a and S9). Nevertheless, low-intensity peaks corresponding to the Ts group were still present in the ^{1}H NMR spectrum of β-CD-EA. Therefore, diffusion NMR spectra (2D DOSY) were recorded to determine whether these Ts groups were chemically bound to the β-CD rings. Since the self-diffusion coefficient of Ts moieties (3.27 × 10^{-10} m^2/s) was much higher than that of β-CD-EA (1.03 × 10^{-10} m^2/s), these groups attributed to the unwashed residual EA salt of TsOH were not bound to β-CD rings (Figure S3c). The introduction of vinyl groups by the reaction of β-CD-EA with DVS was confirmed by the presence of signals from vinyl protons marked as "9" and "10" in the ^{1}H NMR spectrum of β-CD-VS (Figure S3b). Moreover, diffusion NMR measurements showed the same self-diffusion coefficient of the VS group as that of the β-CD ring (1.01 × 10^{-10} m^2/s), indicating that VS was chemically bound to β-CD (Figure S3d).

In the case of DPA-Dex-β-CD, the analysis and accurate peak assignment of the NMR signals in the ^{1}H and ^{13}C spectra were rather complicated because the subunits in modified Dex and β-CD have similar structures and therefore provide overlapping NMR signals (Figure S5). However, the formation of DPA-Dex-β-CD by the reaction of the β-CD-VS double bond with Dex-EA could be deduced from the absence of NMR signals of the VS groups (Figure S5a). Moreover, in the ^{13}C NMR spectrum of DPA-Dex-β-CD, C1 carbon signals from both the Dex and β-CD subunits were distinguished, again suggesting that β-CD was bound with Dex (Figure S5c). In addition, by comparing the integral C1 signal intensity of the β-CD carbon rings at 102.58 ppm with the C1 signals of the Dex main chain and terminal groups at 98.77 and 101.17 ppm, respectively, the number of β-CD units in DPA-Dex-β-CD was evaluated (Figure S6); on average, ~63% of glucose units in Dex bound β-CD. Finally, the ^{31}P NMR spectrum of DPA-Dex-β-CD showed one main signal at 11.2 ppm corresponding to the diphosphonic acid groups (Figure S7).

Another technique to characterize both Dex and β-CD and their derivatives was FTIR spectroscopy (Figure 4a–c). The spectra of Dex and β-CD showed considerable similarity; the band at 3300–3330 cm^{-1} was attributed to the hydroxyl stretching vibration (νOH) of the polysaccharide [37]. The band at 2920 was ascribed to the C-H stretching vibration, while the peak at 912 cm^{-1} was due to the α-glycosidic bond of Dex. Other major characteristic bands at 1154, 1101 and 1010 cm^{-1} were ascribed to valence vibrations of C–O and C–C bonds and deformation vibrations of the CCH, COH and HCO bonds. The FTIR spectrum of the Dex-Ts showed typical Dex peaks and intense peaks at 1175 cm^{-1} ($\nu_{sym}SO_2$) and 815 cm^{-1} (δC-H$_{ar}$) characteristic of the tosyl [12]. The spectrum of β-CD-Ts showed similar bands at 1360, 1175 and 813 cm^{-1} attributed to ν_{as}, $\nu_{sym}SO_2$ stretching and δC-H$_{ar}$ rocking vibrations, respectively. In the spectra of β-CD-EA and Dex-EA, the peak at 1175 cm^{-1} assigned to the $\nu_{sym}SO_2$ vibration disappeared, confirming the replacement of the tosyl group by ethanolamine. In contrast to β-CD-EA, the intensity of the peak at 1300 cm^{-1} in the spectrum of β-CD-VS increased, which probably belonged to the νSO_2 stretching vibration due to the functionalization of β-CD by the vinyl sulfone group [38]. In the spectrum of DPA-Dex-β-CD, a new peak appeared at 887 cm^{-1}, most probably assigned to the νP-OH vibration, confirming the introduction of diphosphonic acid groups into the polymer [39].
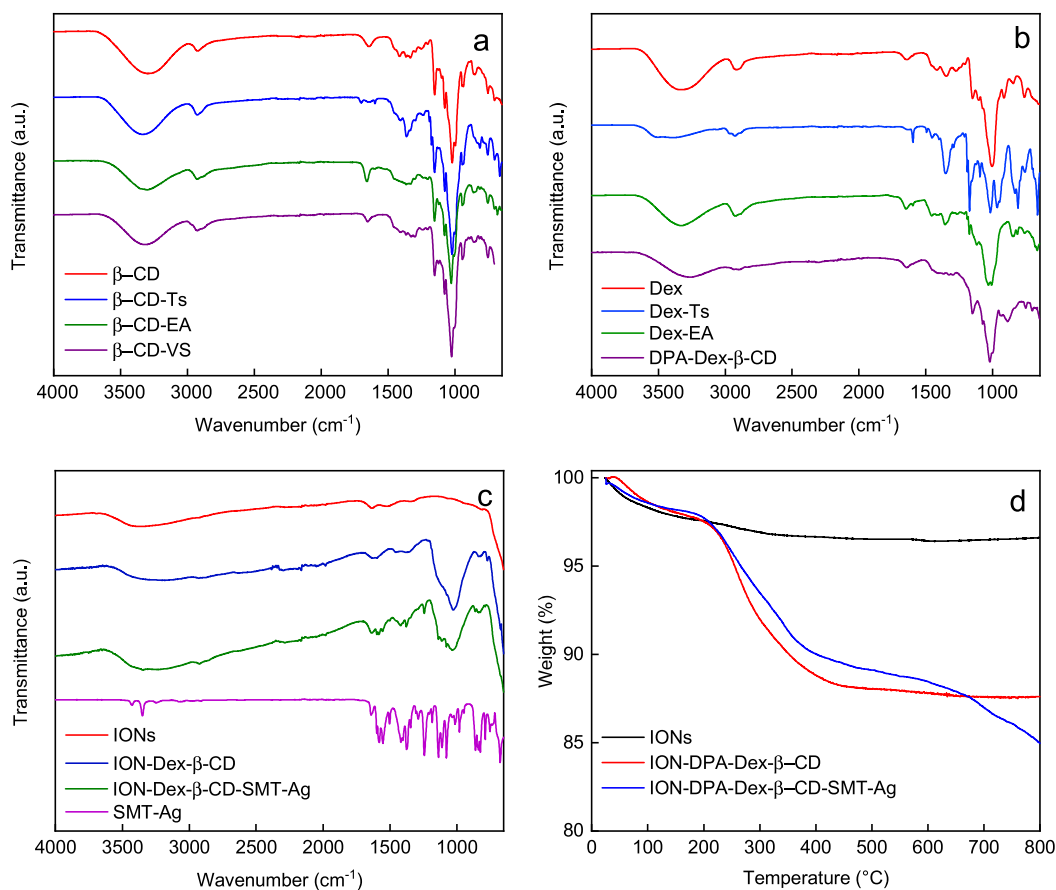
Figure 4. (**a–c**) FTIR and (**d**) TGA analysis of IONs, β-CD, β-CD-Ts, β-CD-EA, β-CD-VS, Dex, Dex-Ts, Dex-EA, SMT, DPA-Dex-β-CD, ION-DPA-Dex-β-CD and ION-DPA-Dex-β-CD-SMT.

In addition, the successful reactions of Dex-EA with β-CD-VS and Dex-β-CD with VDPA were confirmed by analysis of sulfur, phosphorus and nitrogen in both the starting β-CD and Dex derivatives and the final DPA-Dex-β-CD conjugate (Table S1). While β-CD-Ts contained 2.33 wt.% sulfur, i.e., 93% of β-CD molecules were monotosylated, β-CD-EA

had 1.2 wt.% nitrogen, indicating full substitution of Ts groups. As β-CD-VS contained 2.04 wt.% sulfur, 82% of β-CD was modified with DVS. In the case of Dex-Ts containing 10.07 wt.% sulfur, all glucose units were assumed to be tosylated (Table S1), which was ~30% more than according to the ^{1}H NMR spectrum. This may be due to the lower mobility of the side Ts groups and hence lower integral values in the spectrum. The reaction of Dex-Ts with EA was documented by nitrogen analysis; 5.04 wt.% nitrogen in Dex-EA indicated that ~80% of the glucose units were modified by EA. Finally, after the reactions of Dex-EA with β-CD-VS and Dex-β-CD with VDPA, 1.40 wt.% sulfur and 6.62 wt.% phosphorus were found in the DPA-Dex-β-CD polymer, respectively (Table S1). This suggests that ~70% of the glucose units in Dex were modified by β-CD, which is comparable to the ^{13}C NMR results.

3.3. Preparation of Silver-Sulfamethazine-Conjugated β-Cyclodextrin/Dextran-Coated IONs (ION@DPA-Dex-β-CD-SMT-Ag)

SMT-Ag was selected as an antibacterial agent in this report, as it has a substantially higher minimal inhibitory concentration than SMT alone. In order to prepare IONs conjugated with the SMT-Ag antibiotic as an efficient drug delivery platform, IONs were coated with DPA-Dex-β-CD to form ION@DPA-Dex-β-CD particles (Figure 3). As the organic coating was not contrasted in the TEM, the number-average diameter and dispersity of ION@DPA-Dex-β-CD did not differ from neat IONs (Table 1). In contrast, the hydrodynamic diameter slightly increased (D_h = 155 ± 2 nm) due to the presence of the DPA-Dex-β-CD layer on the particle surface. At the same time, the small polydispersity (PD = 0.07) indicated a narrow distribution of particle sizes. In addition, the absolute value of ζ-potential of ION@DPA-Dex-β-CD particles decreased from −26 ± 5 mV for neat IONs to −18 ± 4 mV due to the shielding of the DPA-Dex-β-CD shell. The advantage of diphosphonic acid in the DPA-Dex-β-CD conjugate consisted in its ability to complex with Fe ions of IONs to form stable water-dispersible particles [40]. Mixing the ION@DPA-Dex-β-CD particles with SMT-Ag then resulted in its complexation with β-CD to form ION@DPA-Dex-β-CD-SMT-Ag particles (Figure 3). While their D_n were almost the same as that of the ION@DPA-Dex-β-CD particles, the D_h increased to 244 ± 3 nm (PD = 0.29) and the ζ-potential decreased to −36 ± 2 mV, probably due to the adsorption of hydroxyl ions originating from NH$_4$OH.

Table 1. Physicochemical characterization of particles.

	D_n (nm)	Đ	D_h (nm)	PD	ζ-Potential (mV)	Coating (wt.%)
IONs	8 ± 2	1.29	108 ± 1	0.13	−26 ± 5	-
ION@DPA-Dex-β-CD	9 ± 2	1.28	155 ± 2	0.07	−18 ± 4	10.8
ION@DPA-Dex-β-CD-SMT-Ag	8 ± 2	1.26	244 ± 3	0.29	−36 ± 2	13.1

D_n—number-average diameter (TEM), Đ—dispersity (TEM), D_h—hydrodynamic diameter (DLS), PD—polydispersity (DLS).

The surface composition of ION@DPA-Dex-β-CD and ION@DPA-Dex-β-CD-SMT-Ag was further analyzed by FTIR spectroscopy (Figure 4c). The bands at 1025 and 1358 cm^{-1} were attributed to ν_{as}(C-O-C) asymmetric and ν_s(CH$_2$) symmetric stretching vibration, respectively, confirming the presence of DPA-Dex-β-CD on the ION surface. The new peaks at 860, 1243, 1418 and 1580 cm^{-1} in the spectrum of ION@DPA-Dex-β-CD-SMT-Ag were assigned to ν(C-H$_{ar}$), ν(C-N), δ(C-H$_{ar}$) and ν(C=C) vibrations, respectively. These bands were similar to those in the spectrum of SMT-Ag, confirming its incorporation in ION@DPA-Dex-β-CD-SMT-Ag particles. The content of the DPA-modified polysaccharide on the particle surface was then analyzed by TGA (Figure 4d). In the thermograms of ION@DPA-Dex-β-CD and ION@DPA-Dex-β-CD-SMT-Ag, the initial weight loss below 120 °C was due to the dehydration of the particles. Losses above 120 °C were attributed to the decomposition of the organic shell on the particles surface. As a result, the amount

of coating on the ION@DPA-Dex-β-CD and ION@DPA-Dex-β-CD-SMT-Ag particles was 10.8 and 13.1 wt.%, respectively (Table 1). The 2.3% increase in organic content in the ION@DPA-Dex-β-CD-SMT-Ag nanoparticles was due to the incorporation of SMT-Ag (Figure 4d). The antibiotic content in the particles was calculated to be ~29 μg per mg due to the fact that the silver in SMT-Ag is non-flammable.

SMT-Ag is highly hydrophobic, with water solubility <3 μg/mL, as determined by UV–Vis spectrophotometry, which makes the binding of SMT-Ag to the carrier by adsorption or complexation quite challenging. However, some silver sulfonamides show increased solubility in ammonia [41]. The solubility of STM-Ag in 0.06% ammonia was nine times higher than that in water, reaching 18 ± 0.2 ug/mL, which may potentially simplify drug loading. In addition, β-CD forms a complex with sulfamethazine, which promotes its solubility in water [19]. Thus, after the addition of β-CD, the solubility of SMT-Ag increased twice, reaching 38 ± 0.4 ug/mL, probably due to the formation of an inclusion complex of β-CD with SMT-Ag. All these indicate that β-CD-containing carriers based on IONs are able to encapsulate SMT-Ag. The amount of SMT-Ag incorporated in the particles was 24 ± 0.6 μg of SMT-Ag per mg, which was comparable to the TGA results (Table 2). It should be added that various organic molecules, including SMT-Ag, can adsorb on the surface of IONs due to the large and charged surface area. According to UV–Vis spectroscopy, 3 ± 0.2 μg SMT-Ag per mg was adsorbed on neat IONs, from which $LE = 0.3\%$ SMT-Ag was calculated (Equation (1)). In contrast, the LE of ION@DPA-Dex-β-CD-SMT-Ag particles was 2.1% (Table 2), indicating that the Dex-β-CD shell increased the LE for ION@DPA-Dex-β-CD-SMT-Ag seven times compared with neat particles. In contrast to other drug delivery carriers, such as hollow porous silica particles ($LE > 9\%$) or magnetic core-shell $Mn_{0.3}Fe_{2.7}O_4@SiO_2$ nanoparticles ($LE = 10.4\%$), the ION@DPA-Dex-β-CD-SMT-Ag particles had lower drug loading [42,43]. However, the loading efficiency depends on the properties of both the carrier and the drug, such as molecular weight, particle volume and surface area, affinity of the drug to the carrier, etc. [44]. While the ION@DPA-Dex-β-CD particles could adsorb the drug only on the surface and in the polymer corona, the silica particles could utilize the entire volume of the inner cavities and surface for loading. It should also be taken into account that low antibiotic content does not necessarily mean low antibacterial efficacy. For example, the nanofibers loaded with 2 μg of silver-sulfadiazine per mg showed high antibacterial activity against *E. coli* and *Acinetobacter baumannii* [45].

Table 2. Silver-sulfamethazine (SMT-Ag) loading efficiency (LE) of IONs and ION@DPA-Dex-β-CD particles.

	SMT-Ag Content (μg/mg of IONs)	LE (%)
IONs	3 ± 0.2	0.3 ± 0.02
ION@DPA-Dex-β-CD	24 ± 0.6	2.1 ± 0.03

3.4. Antimicrobial Effects

3.4.1. Qualitative DDT Evaluation

Sulfamethazine is a traditional antibiotic used to treat Gram-positive bacterial infections, including staphylococcal infections (respiratory tract, urinary tract, etc.) in humans and animals. DDT is a standardized method recommended by norm-making authorities (e.g., EUCAST, CLSI and AOAC) to evaluate the antimicrobial effects of compounds, including pharmaceuticals and disinfectants. In these trials, a screening phase is commonly performed to study newly synthesized or naturally isolated molecules for use as antimicrobials. EUCAST-based methods depend on microbial physiology, as the tested microorganisms should have reached their optimum physiological fitness at the time of DDT evaluation. Therefore, the inhibition zones for bacteria (*S. aureus* and *E. coli*) were assessed within a growth span of 24 h; the same applied to the yeast *C. albicans*, while mold (*A. niger*) needed 72 h to develop mature hyphal growth. The aim was to select the most

promising molecules to be submitted for further, more accurate but also more laborious and costly subsequent quantitative tests, such as minimum inhibitory concentration (MIC) and minimum microbicidal concentration (MMC), as well as toxicity tests, etc. Our DDT results showed only limited activity of the ION@DPA-Dex-β-CD-SMT-Ag particles against *S. aureus*, as well as against Gram-negative *E. coli* and even against the mold *A. niger*, as only fine zones with a radius of ~1–2 mm were present around the discs. The DDT method uses the free diffusion of the antimicrobial agent into the cultivation medium, and, since the tested particle dispersions were colloidal in nature, diffusion of their active ingredient was thus obviously limited (Table 3). This statement was also indirectly demonstrated in a complementary experiment with a free SMT solution in the presence of particles. This solution provided an inhibition zone around the discs due to the diffusion effect; particle dispersion with free SMT showed activity against *S. aureus* with inhibition zone diameters of 5.4 and 10.2 mm for 40 and 120 µg of particles per 5- and 10-mm disc, respectively. In contrast, neat IONs and ION@DPA-Dex-β-CD particles did not show antimicrobial activity. Thus, the observed effect of the microbial growth inhibition effect was clearly related to the active compound (SMT-Ag) encapsulated in the tested particles.

Table 3. Qualitative and quantitative evaluation of antimicrobial activity of nanoparticles.

Tested Particles	*Staphylococcus aureus* CCM 2022		*Escherichia coli* CCM 3954		*Candida albicans* CCM 8186		*Aspergillus niger*	
	DDT	MIC/MBC (µg/mL)	DDT	MIC/MBC (µg/mL)	DDT	MIC/MMC (µg/mL)	DDT	MIC/MMC (µg/mL)
IONs	Growth around the disc/NT	NE/NE	Growth around the disc/NT	NT	Growth around the disc/growth within the drop	NT	Growth around the disc/NT	NT
ION@DPA-Dex-β-CD	Growth around the disc/NT	NE/NE	Growth around the disc/NT	NT	Growth around the disc/growth within the drop	NT	Growth around the disc/NT	NT
ION@DPA-Dex-β-CD-SMT-Ag	2 mm inhibition zone/no growth within the drop	500/NE	1 mm inhibition zone/no growth within the drop	500/1000	Growth around the disc/growth within the drop	250/NE	2 mm inhibition zone/no growth within the drop	250/1000

DDT—disc diffusion test (40 µg of particles, i.e., 10 µL drop on 5 mm disc); MIC/MBC/MMC—minimum inhibitory, bactericidal and microbicidal concentrations; NT – not tested; NE – not effective within the tested range of concentration (2.5–1500 µg/mL).

3.4.2. Quantitative MIC/MBC/MMC Evaluation

Since DDT provided only a qualitative assessment of antibacterial activity, the MIC/MBC/MMC assay was selected to quantify the effect. The MIC parameter is a basic quantitative descriptor of the antimicrobial potential of compounds, indicating their lowest concentration that inhibits the growth of a specific microbe under standard test conditions according to the analytical authority (e.g., EUCAST). In any case, the value itself does not describe whether the antimicrobial effect is static—only postponing microbial growth due to reversible changes in the microbial cell—or cidal, i.e., the microbial cells are devitalized completely. It is the microbial devitalization potential that characterizes the MBC/MMC parameter. While the ION@DPA-Dex-β-CD-SMT-Ag particles showed good antibacterial effect against *S. aureus* and *E. coli* according to the MIC/MBC test, the antifungal activity against *C. albicans* and *A. niger* was even more pronounced (Figure 5).
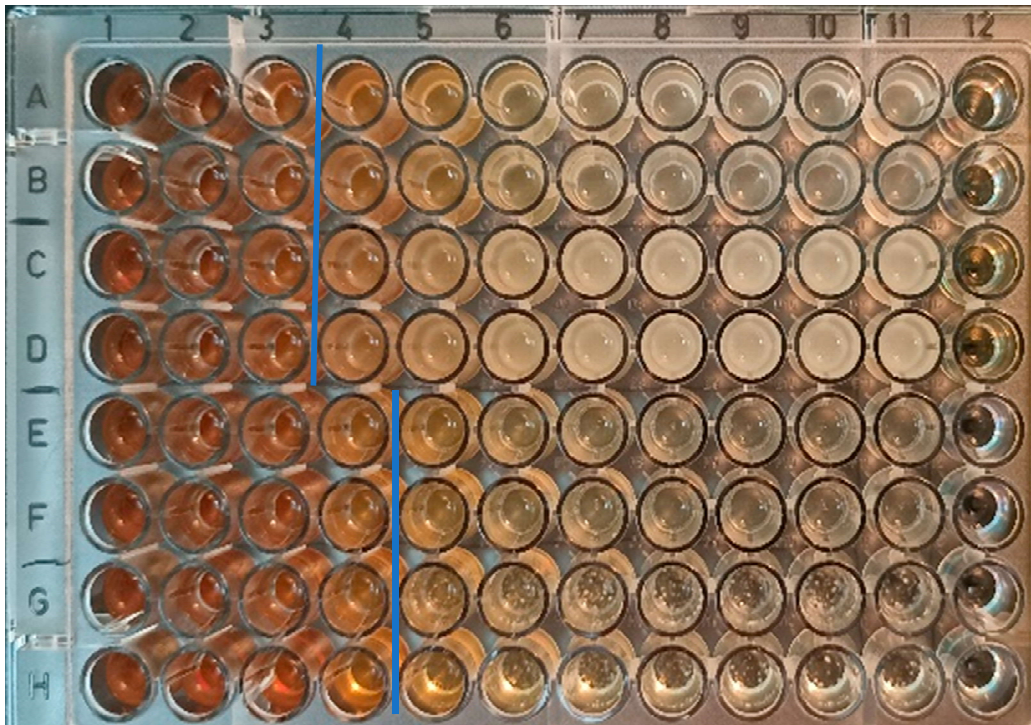
Figure 5. MIC of ION-DEX-CD-SMT-Ag; columns 1–10, concentration 1500–2.5 µg/mL; column 11, positive control; column 12, negative control. Row A, B—*S. aureus*; row C, D—*E. coli*; row E, F—*C. albicans*; row G, H—*A. niger*. The blue lines show the boundary between no growth and pathogen growth; column 3/4 is for rows A–D, and column 4/5 is for rows E–H.

This enhanced antibacterial efficiency can be advantageously used, for example, on medical tools and devices to prevent the formation of *C. albicans* biofilms, which account for the largest proportion of hospital-acquired fungal infections. For ION@DPA-Dex-β-CD-SMT-Ag particles, the lowest concentration of the antimicrobial agent, which visibly inhibited the growth of the microorganism, was quite high (500/1000 µg/mL; Table 3). Note that the above values refer to ION@DPA-Dex-β-CD-SMT-Ag particles. After recalculation, this means that the MIC/MBC for SMT-Ag was 12/24 µg/mL, which represents a higher antimicrobial activity than in previously published work [4]. In the agro-food sector, Ag nanoparticles (6–12 nm) are typically used at a concentration of 400 mg/L, which shows high antibacterial efficacy [46]; however, according to other sources, concentrations as low as 4–16 mg/L have been found to be sufficiently effective [47]. In the case of antifungal activity, MIC/MMC was at the level of 250/1000 µg/mL (Table 3). Thus, the antimicrobial effect of Ag in the particles is most likely responsible for this antifungal activity, while the antibacterial activity may be related to the presence of SMT, especially against *S. aureus*, although, as expected, no additive effect of combined SMT-Ag action was observed. This observation may be related to the steric effect of the particles. Since eukaryotic fungal cells are larger than bacteria and because both *C. albicans* and *A. niger* form hyphal structures, their surface exposed to biocide-conjugated particles is also much larger. The mechanism of the antimicrobial effect of Ag is to break down the microbial cell wall structure, allowing ions (or other agents bound to the particles) to penetrate into the cells [48]. Although the reparation mechanisms of cell damage due to antimicrobial agents are more complex in eukaryotes than in prokaryotic bacteria, with rapid penetration of the toxic substances into the cells, the toxic effect can occur even at low concentrations.

4. Conclusions

In this report, we developed an original multistep procedure for the preparation of a magnetically controlled drug delivery system. Due to their magnetic nature and non-toxicity, IONs were used as carrier particles. Dex modified with β-CD was selected as the ION coating because both substances are biocompatible and do not cause nonspecific sorption of proteins in the bloodstream. In addition, Dex provides good stabilization of the nanoparticle dispersion, while β-CD can easily capture the SMT-Ag antibiotic for future delivery to the target site due to the presence of an internal hydrophobic pocket. In this way, highly hydrophobic antibiotics such as SMT-Ag can be solubilized, which is essential for their effective functioning in the affected tissue of the organism; this also extends the range of applicability of hydrophobic drugs. The synthetic procedure involved the reaction of β-CD-Ts with EA, resulting in β-CD-EA with a secondary amino group, which required a large molar excess of EA relative to β-CD to achieve a reasonable yield. The amino group of β-CD-EA then reacted with DVS to yield vinyl sulfone-functionalized β-cyclodextrin (β-CD-VS), which combined the ability of β-CD to carry SMT-Ag antibiotic with the good reactivity of the vinyl sulfone group towards Dex-EA. This highly efficient reaction produced Dex-β-CD, in which ~70% of the glucose units reacted with β-CD. The resulting Dex-β-CD conjugate then reacted with VDPA-containing diphosphonate groups, which complexed well with the surface Fe ions of the IONs to form DPA-Dex-β-CD-coated magnetic nanoparticles. Finally, SMT-Ag was successfully incorporated into β-CD in ION@DPA-Dex-β-CD particles; the antibiotic content was 24 μg per mg. The obtained ION@DPA-Dex-β-CD-SMT-Ag nanoparticles were colloidally stable in water due to the high absolute value of ξ-potential (−36 mV). To the best of our knowledge, there are currently no papers addressing the development of such magnetic iron oxide-based carriers for targeted delivery of silver-sulfamethazine. In addition, the magnetic core of the newly developed ION@DPA-Dex-β-CD-SMT-Ag drug delivery system can be used as a contrast agent for magnetic resonance imaging, which will allow monitoring of inflammation treatment at the cellular level.

Antibacterial in vitro tests showed that the ION@DPA-Dex-β-CD-SMT-Ag nanoparticles exhibited bactericidal activity against Gram-positive *S. aureus* and Gram-negative *E. coli* bacteria (MIC/MBC = 500/1000 μg/mL). At the same time, the antifungal activity against *C. albicans* and *A. niger* was even more pronounced, with MIC/MMC of ION@DPA-Dex-β-CD-SMT-Ag particles reaching 250/1000 μg/mL. Targeted administration of antibiotics can thus overcome some of the shortcomings of systemic therapy, such as low concentrations at the site of the inflammation and antibiotic accumulation at the unwanted site. The magnetic nature of the ION@DPA-Dex-β-CD-SMT-Ag nanoparticles responding to an external magnetic field is particularly important, as magnetic targeting can increase the local concentration of the antibiotic at the affected site and thus the antimicrobial effect. Magnetically controlled ION@DPA-Dex-β-CD-SMT-Ag nanoparticles could be thus promising for the topical delivery of antimicrobials to treat bacterial or fungal infections in animals and eventually in humans; nevertheless, future research is needed to further clarify the antimicrobial mechanism.

References

1. Aslam, B.; Wang, W.; Arshad, M.I.; Khurshid, M.; Muzammil, S.; Rasool, M.H.; Nisar, M.A.; Alvi, R.F.; Aslam, M.A.; Qamar, M.U.; et al. Antibiotic resistance: A rundown of a global crisis. *Infect. Drug Resist.* **2018**, *11*, 1645–1658. [CrossRef]
2. Ovung, A.; Bhattacharyya, J. Sulfonamide drugs: Structure, antibacterial property, toxicity, and biophysical interactions. *Biophys. Rev.* **2021**, *13*, 259–272. [CrossRef]
3. Niu, Z.; Liu, Y.; Li, X.; Zhu, H.; Zhang, M.; Yan, K.; Chen, H. Colorimetric detection of sulfamethazine based on target resolved calixarene derivative stabilized gold nanoparticles aggregation. *Microchim. Acta* **2022**, *189*, 71. [CrossRef]
4. Tailor, S.M.; Patel, U.H. Synthesis, spectroscopic characterization, antimicrobial activity and crystal structure of silver and copper complexes of sulfamethazine. *J. Coord. Chem.* **2015**, *68*, 2192–2207. [CrossRef]
5. Eleraky, N.E.; Allam, A.; Hassan, S.B.; Omar, M.M. Nanomedicine fight against antibacterial resistance: An overview of the recent pharmaceutical innovations. *Pharmaceutics* **2020**, *12*, 142. [CrossRef]
6. Wahajuddin; Arora, S. Superparamagnetic iron oxide nanoparticles: Magnetic nanoplatforms as drug carriers. *Int. J. Nanomed.* **2012**, *7*, 3445–3471. [CrossRef]
7. Chang, Y.-L.; Liao, P.-B.; Wu, P.-H.; Chang, W.-J.; Lee, S.-Y.; Huang, W.-M. Cancer cytotoxicity of a hybrid hyaluronan-superparamagnetic iron oxide nanoparticle material: An *in-vitro* evaluation. *Nanomaterials* **2022**, *12*, 496. [CrossRef]
8. Mylkie, K.; Nowak, P.; Rybczynski, P.; Ziegler-Borowska, M. Polymer-coated magnetite nanoparticles for protein immobilization. *Materials* **2021**, *14*, 248. [CrossRef]
9. Tassa, C.; Shaw, S.Y.; Weissleder, R. Dextran-coated iron oxide nanoparticles: A versatile platform for targeted molecular imaging, molecular diagnostics, and therapy. *Acc. Chem. Res.* **2011**, *18*, 842–852. [CrossRef]
10. Lemechko, P.; Renard, E.; Guezennec, J.; Guezennec, C.; Langlois, V. Synthesis of dextran-graft-PHBHV amphiphilic copolymer using click chemistry approach. *Reac. Funct. Polym.* **2012**, *72*, 487–494. [CrossRef]
11. Yang, J.; Liu, Y.; Wang, H.; Liu, L.; Wang, W.; Wang, C.; Wang, Q.; Liu, W. The biocompatibility of fatty acid modified dextran-agmatine bioconjugate gene delivery vector. *Biomaterials* **2012**, *33*, 604–613. [CrossRef]
12. Heinze, T.; Michealis, N.; Hornig, S. Reactive polymeric nanoparticles based on unconventional dextran derivatives. *Eur. Polym. J.* **2007**, *43*, 697–703. [CrossRef]
13. Xu, J.; Tian, Y.; Li, Z.; Tan, B.H.; Tang, K.Y.; Tam, K.C. β-Cyclodextrin functionalized magnetic nanoparticles for the removal of pharmaceutical residues in drinking water. *J. Ind. Eng. Chem.* **2022**, *109*, 461–474. [CrossRef]
14. Ahmed, G.H.G.; Laíño, R.B.; Calzón, J.A.G.; García, M.E.D. Magnetic nanoparticles grafted with β-cyclodextrin for solid-phase extraction of 5-hydroxy-3-indole acetic acid. *Microchim Acta* **2014**, *181*, 941–948. [CrossRef]
15. Banerjee, S.S.; Chen, D.-H. Magnetic nanoparticles grafted with cyclodextrin for hydrophobic drug delivery. *Chem. Mater.* **2007**, *19*, 6345–6349. [CrossRef]
16. Tang, X.; Wen, Y.; Zhang, Z.; Zhu, J.; Song, X.; Li, J. Rationally designed multifunctional nanoparticles as GSH-responsive anticancer drug delivery systems based on host-guest polymers derived from dextran and β-cyclodextrin. *Carbohydrate Polym.* **2023**, *320*, 121207. [CrossRef]
17. Zhang, Y.; Jiang, F.; Huang, D.; Hou, S.; Wang, H.; Wang, M.; Chi, Y.; Zhao, Z. A facile route to magnetic mesoporous core–shell structured silicas containing covalently bound cyclodextrins for the removal of the antibiotic doxycycline from water. *RSC Adv.* **2018**, *8*, 31348–31357. [CrossRef]
18. Zhang, Y.; Li, J.; Wang, F.F.; Wu, G.; Qv, X.; Hong, H.; Liu, C. Recovery and separation of erythromycin from industrial wastewater by imprinted magnetic nanoparticles that exploit β-cyclodextrin as the functional monomer. *J. Sep. Sci.* **2016**, *39*, 450–459. [CrossRef]
19. Zoppi, A.; Delrivo, A.; Aiassa, V.; Longhi, M.R. Binding of sulfamethazine to β-cyclodextrin and methyl-β-cyclodextrin. *AAPS PharmSciTech* **2013**, *14*, 727–735. [CrossRef]
20. Abou-El-Sherbini, K.S.; Amer, M.H.A.; Abdel-Aziz, M.S.; Hamzawy, E.M.A.; Sharmoukh, W.; Elnagar, M.M. Encapsulation of biosynthesized nanosilver in silica composites for sustainable antimicrobial functionality. *Glob. Chall.* **2018**, *2*, 1800048. [CrossRef]
21. Wang, Q.; Zhang, Y.; Li, Q.; Chen, L.; Liu, H.; Ding, M.; Dong, H.; Mou, Y. Therapeutic applications of antimicrobial silver-based biomaterials in dentistry. *Int. J. Nanomed.* **2022**, *17*, 443–462. [CrossRef]

22. Zhang, J.; Xu, Q.; Li, H.; Zhang, S.; Hong, A.; Jiang, Y.; Hu, N.; Chen, G.; Fu, H.; Yuan, M.; et al. Self-powered electrodeposition system for sub-10-nm silver nanoparticles with high-efficiency antibacterial activity. *J. Phys. Chem. Lett.* **2022**, *13*, 6721–6730. [CrossRef]

23. Degenhardt, C.R.; Burdsall, D.C. Synthesis of ethenylidenebis(phosphonic acid) and its tetraalkyl esters. *J. Org. Chem.* **1986**, *51*, 3488–3490. [CrossRef]

24. Zhong, N.; Byun, H.-S.; Bittrnan, R. An improved synthesis of 6-*O*-monotosyl-6-deoxy-β-cyclodextrin. *Tetrahedron Lett.* **1998**, *39*, 2919–2920. [CrossRef]

25. del Castillo, T.; Marales-Sanfrutos, J.; Santoyo-González, F.; Magez, S.; Lopez-Jaramillo, F.J.; Garcia-Salcedo, J.A. Monovinyl sulfone β-cyclodextrin. A flexible drug carrier systém. *ChemMedChem* **2014**, *9*, 383–389. [CrossRef]

26. Zasońska, B.A.; Boiko, N.; Klyuchivska, O.; Trchová, M.; Petrovský, E.; Stoika, R.; Horák, D. Silica-coated γ-Fe₂O₃ nanoparticles: Preparation and engulfment by mammalian macrophages. *J. Nanopharm. Drug Deliv.* **2013**, *1*, 182–192. [CrossRef]

27. Stejskal, E.O.; Tanner, J.E. Spin diffusion measurements: Spin echoes in the presence of a time-dependent field gradient. *J. Chem. Phys.* **1965**, *42*, 288–292. [CrossRef]

28. EUCAST Disk Diffusion Method for Antimicrobial Susceptibility Testing, Version 11.0. Available online: www.eucast.org/fileadmin/src/media/PDFs/EUCAST_files/Disk_test_documents/2023_manuals/Manual_v_11.0_EUCAST_Disk_Test_2023.pdf (accessed on 1 January 2023).

29. Nweze, E.I.; Mukherjee, P.K.; Ghannoum, M.A. Agar-based disk diffusion assay for susceptibility testing of dermatophytes. *J. Clin. Microbiol.* **2010**, *48*, 3750–3752. [CrossRef]

30. Laurent, S.; Forge, D.; Port, M.; Roch, A.; Robic, C.; Vander Elst, L.; Muller, R.N. Magnetic iron oxide nanoparticles: Synthesis, stabilization, vectorization, physicochemical characterizations, and biological applications. *Chem. Rev.* **2008**, *108*, 2064–2110. [CrossRef]

31. Zasońska, B.A.; Bober, P.; Jošt, P.; Petrovský, E.; Boštík, P.; Horák, D. Magnetoconductive maghemite core/polyaniline shell nanoparticles as promising tools for biomedical applications. *Colloids Surf. B* **2016**, *141*, 382–389. [CrossRef]

32. Winkler, R.; Ciria, M.; Ahmad, M.; Plank, H.; Marcuello, C. A review of the current state of magnetic force microscopy to unravel the magnetic properties of nanomaterials applied in biological systems and future directions for quantum technologies. *Nanomaterials* **2023**, *13*, 2585. [CrossRef]

33. Babič, M.; Horák, D.; Jendelová, P.; Glogarová, K.; Herynek, V.; Trchová, M.; Likavčanová, K.; Hájek, M.; Syková, E. Poly(*N,N*-dimethylacrylamide)-coated maghemite nanoparticles for stem cell labeling. *Bioconjugate Chem.* **2009**, *20*, 283–294. [CrossRef]

34. Carone, A.; Emilsson, S.; Mariani, P.; Désert, A.; Parola, S. Gold nanoparticle shape dependence of colloidal stability domains. *Nanoscale Adv.* **2023**, *5*, 2017–2026. [CrossRef]

35. Hu, Q.; Lu, Y.; Luo, Y. Recent advances in dextran-based drug delivery systems: From fabrication strategies to applications. *Carbohydr. Polym.* **2021**, *264*, 117999. [CrossRef]

36. Schneider, H.J.; Hacket, F.; Rüdiger, V.; Ikeda, H. NMR studies of cyclodextrins and cyclodextrin complexes. *Chem. Rev.* **1998**, *98*, 1755–1785. [CrossRef]

37. Purama, R.K.; Goswami, P.; Khan, A.T.; Goyal, A. Structural analysis and properties of dextran produced by *Leuconostoc mesenteroides* NRRL B-640. *Carbohydr. Polym.* **2009**, *76*, 30–35. [CrossRef]

38. Kuniaki, F. The infrared spectrum of dimethyl sulfone. *Bull. Chem. Soc. Jpn.* **1959**, *32*, 1374–1376. [CrossRef]

39. Gong, W. A real-time *in-situ* ATR-FITIR spectroscopic study of linear phosphate on titania surfaces. *Int. J. Miner. Process.* **2001**, *63*, 147–165. [CrossRef]

40. Horwitz, E.P.; Gatrone, R.C.; Nash, K.L. Membrane Extraction with Thermodynamically Unstable Diphosphonic Acid Derivatives. US Patent 5,678,242, 1997. Available online: https://www.osti.gov/biblio/541723 (accessed on 14 October 1997).

41. Sandmann, B.J.; Nesbitt, R.U.; Sandmann, R.A. Characterization of silver sulfadiazine and related compounds. *J. Pharm. Sci.* **1974**, *63*, 948–951. [CrossRef]

42. Guo, L.; Ping, J.; Qin, J.; Yang, M.; Wu, X.; You, M.; You, F.; Peng, H.A. Comprehensive study of drug loading in hollow mesoporous silica nanoparticles: Impacting factors and loading efficiency. *Nanomaterials* **2021**, *11*, 1293. [CrossRef]

43. Wu, T.; Wang, L.; Gong, M.; Lin, Y.; Xu, Y.; Ye, L.; Yu, X.; Liu, J.; Liu, J.; He, S.; et al. Synergistic effects of nanoparticle heating and amoxicillin on *H. pylori* inhibition. *J. Magn. Magn. Mater.* **2019**, *485*, 95–104. [CrossRef]

44. Bohara, R.A.; Thorat, N. (Eds.) *Hybrid Nanostructures for Cancer Theranostics*; Elsevier: Oxford, UK, 2019. [CrossRef]

45. Mutlu-Ağardan, N.B.; Tort, S.; Aydoğduoğlu, Ş.; Kıymacı, M.E. A new insight to silver sulfadiazine antibacterial dressings: Nanoparticle-loaded nanofibers for controlled drug delivery. *AAPS PharmSciTech* **2023**, *24*, 8. [CrossRef]

46. Parzymies, M.; Pudelska, K.; Poniewozik, M. The use of nano-silver for disinfection of *Pennisetum alopecuroides* plant material for tissue culture. *Acta Sci. Pol. Hortorum Cultus* **2019**, *18*, 127–135. [CrossRef]

47. Sarmast, M.K.; Salehi, H.; Khosh-Khui, M. Nano silver treatment is effective in reducing bacterial contaminations of *Araucaria excelsa R. Br. var. glauca* explants. *Acta Biol. Hung.* **2011**, *62*, 477–484. [CrossRef] [PubMed]

48. Dibrov, P.; Dzioba, J.; Gosink, K.K.; Häse, C.C. Chemiosmotic mechanism of antimicrobial activity of Ag⁺ in *Vibrio cholerae*. *Antimicrob. Agents Chemother.* **2002**, *46*, 2668–2670. [CrossRef] [PubMed]

Silver-Sulfamethazine-Conjugated β-Cyclodextrin/Dextran-Coated Magnetic Nanoparticles for Pathogen Inhibition

Table S1. Nitrogen, sulfur and phosphorus content in Dex and β-CD derivatives.

Element \ Samples	N (wt.%)	S (wt.%)	P (wt.%)
β-CD-Ts	-	2.33	-
β-CD-EA	1.20	-	-
β-CD-VS	1.38	2.04	-
Dex-Ts	-	10.07	-
Dex-EA	5.04	2.07	-
Dex-β-CD	1.63	1.67	-
DPA-Dex-β-CD	1.18	1.40	6.62

β-CD-Ts – 6-toluenesulfonyl-β-cyclodextrin, β-CD-EA – 6-deoxy-6-hydroxylethylamino-β-cyclodextrin, β-CD-VS – 6-deoxy-6-(2-hydroxyethyl) (vinylsulfonyl)methylamino-β-cyclodextrin, Dex-Ts – 6-toluenesulfonyl-dextran, Dex-EA – 6-deoxy-6-hydroxylethylamino-dextran and DPA-Dex-β-CD – 1,1-diphosphonic acid-β-cyclodextrin/dextran.
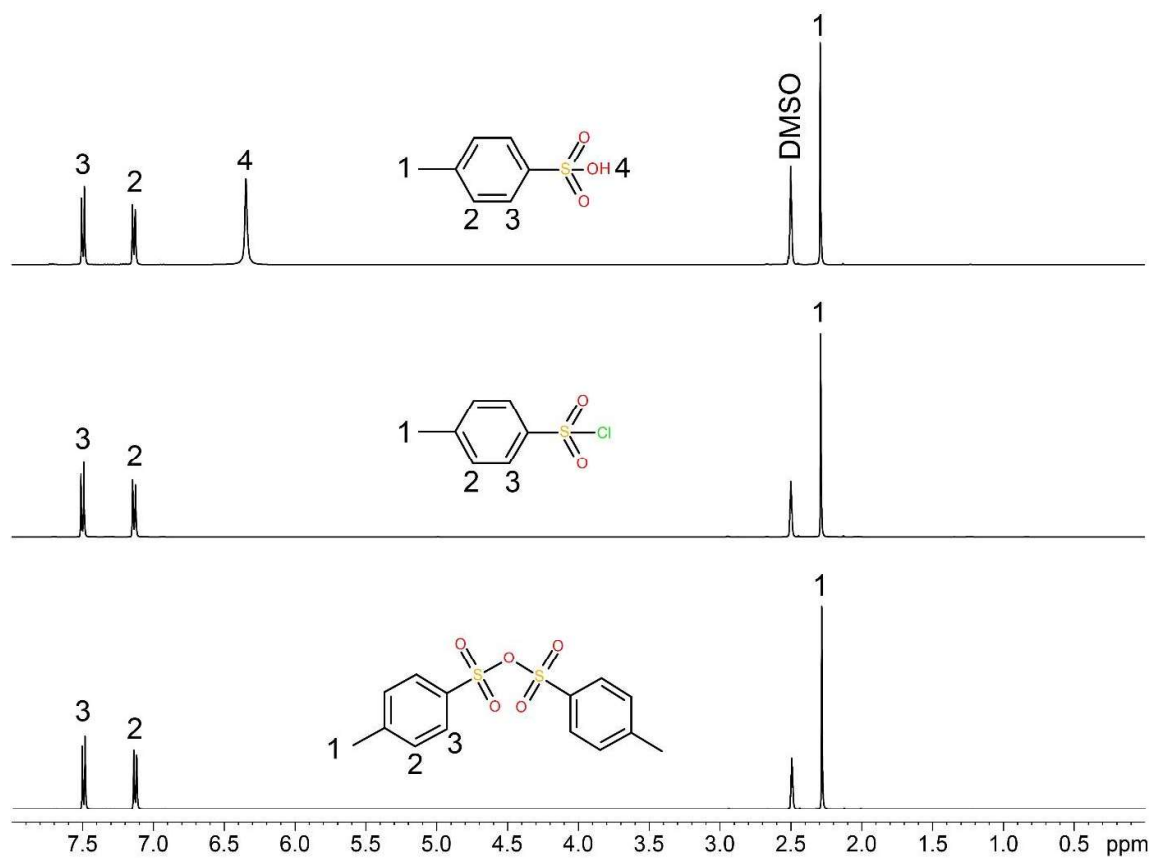
Figure S1. ^{1}H NMR spectra of 4-toluenesulfonic acid (TsOH), 4-toluenesulfonyl chloride (TsCl) and 4-toluenesulfonic anhydride (Ts$_2$O) in DMSO-d6 at 25 ℃.
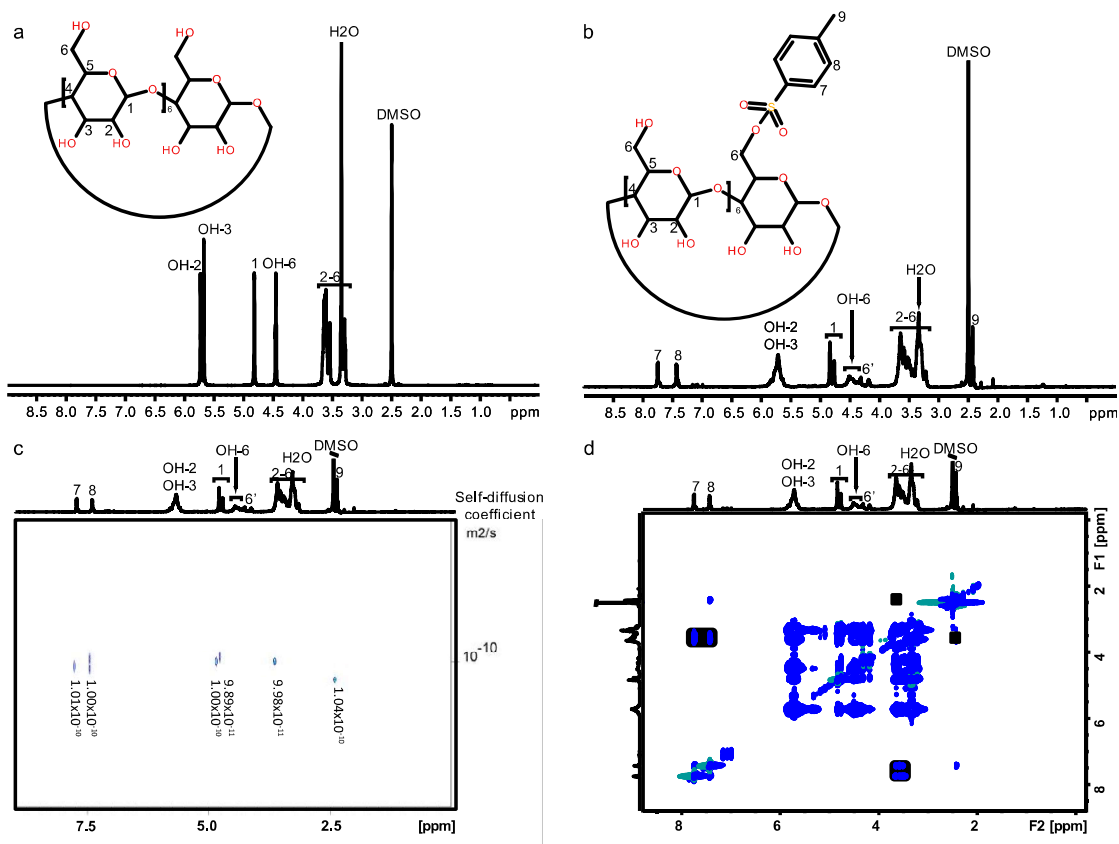
Figure S2. ^{1}H NMR spectra of (a) β-cyclodextrin and (b) β-cyclodextrin modified with tosyl groups dissolved in DMSO-d6, (c) ^{1}H-^{1}H 2D NOESY NMR and (d) 2D DOSY NMR spectra of tosyl-modified β-CD.
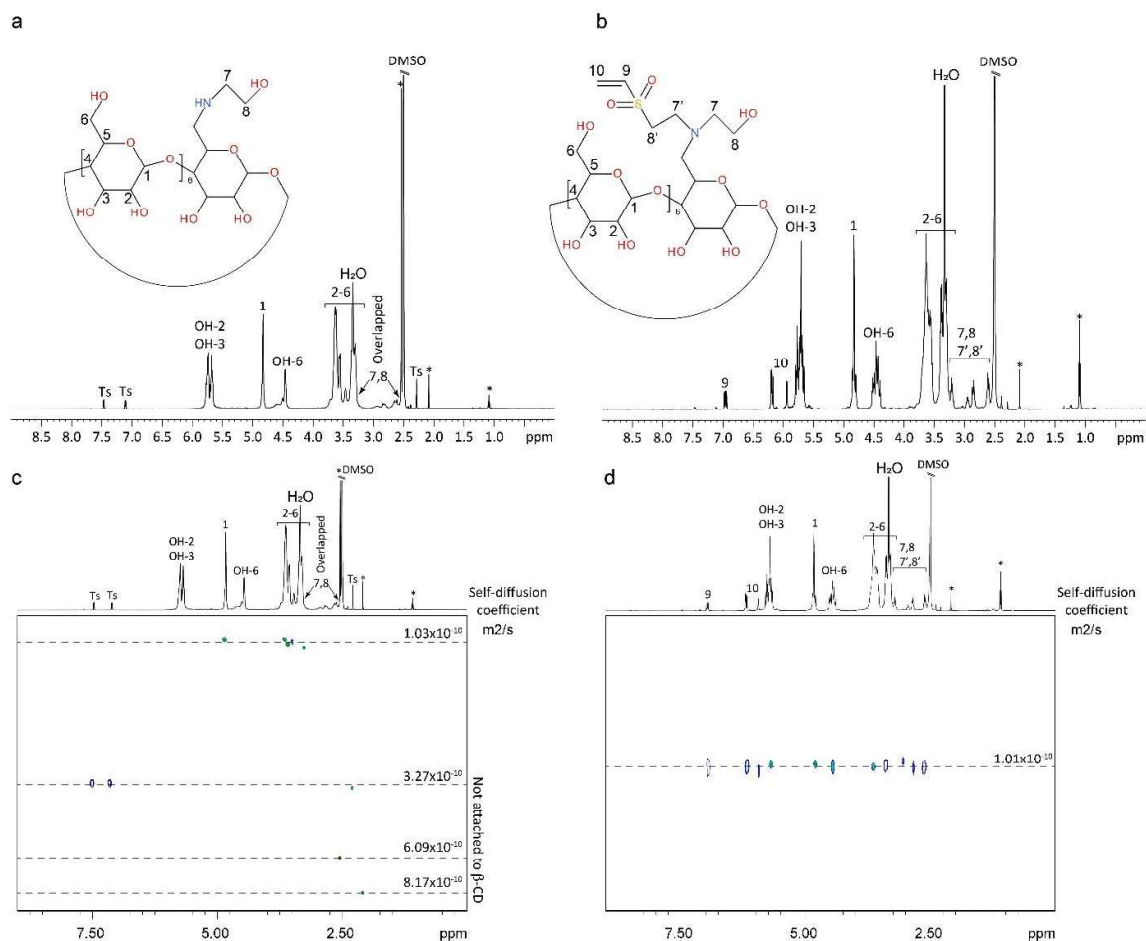
Figure S3. (a, b) ^{1}H NMR and (c, d) DOSY NMR spectra of (a, c) β-CD-EA and (b, d) β-CD-VS. Signals denoted by an asterisk (*) originate from residual solvents used in synthesis. Signals denoted as "Ts" are due to tosyl groups (not attached to β-CD ring).
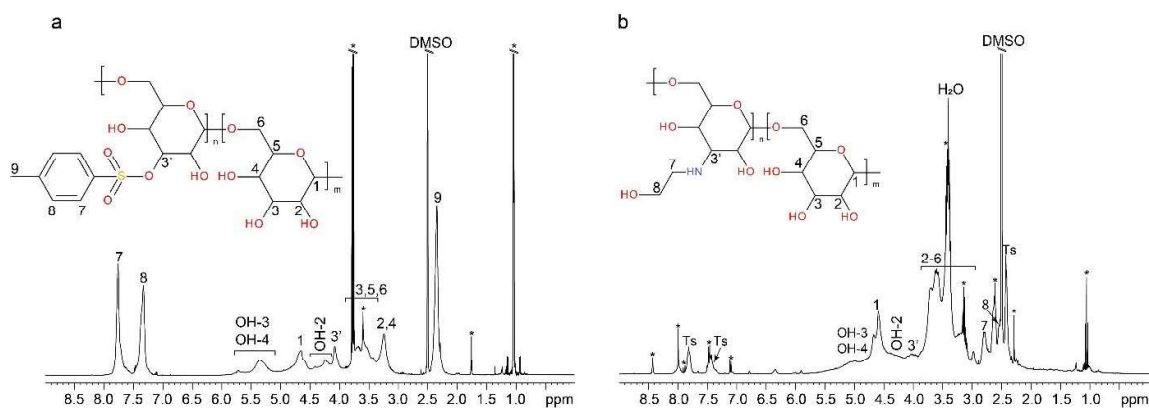
Figure S4. ^{1}H NMR spectra of (a) Dex-Ts and (b) Dex-EA. Signals denoted by an asterisk (*) originate from residual solvents used in synthesis or impurities.
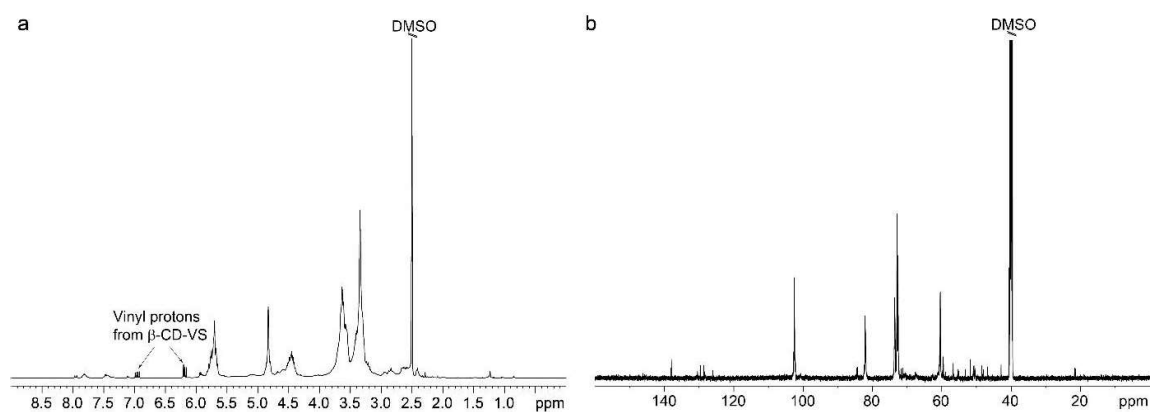
Figure S5. (a) ^{1}H NMR spectrum of DPA-Dex-β-CD and (b) ^{13}C NMR spectrum of DPA-Dex-β-CD.
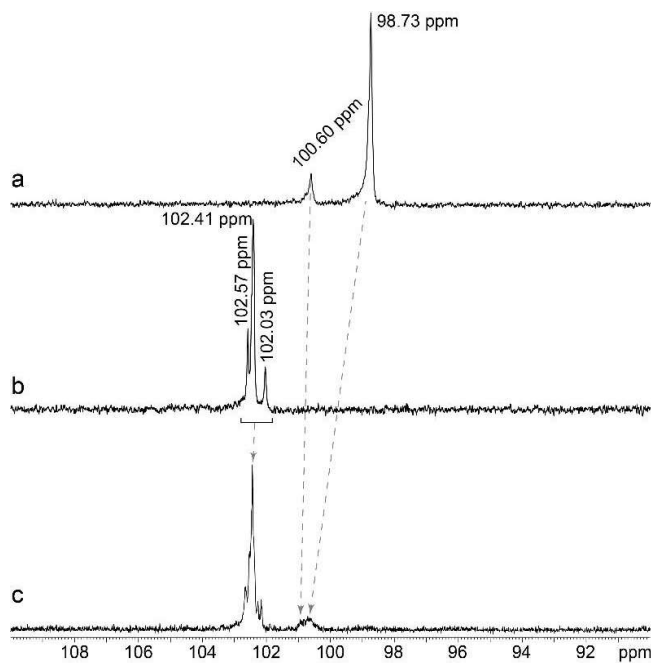
Figure S6. ^{13}C NMR spectra (90-110 ppm region) of (a) Dex-EA, (b) β-CD-EA and (c) DPA-Dex-β-CD.
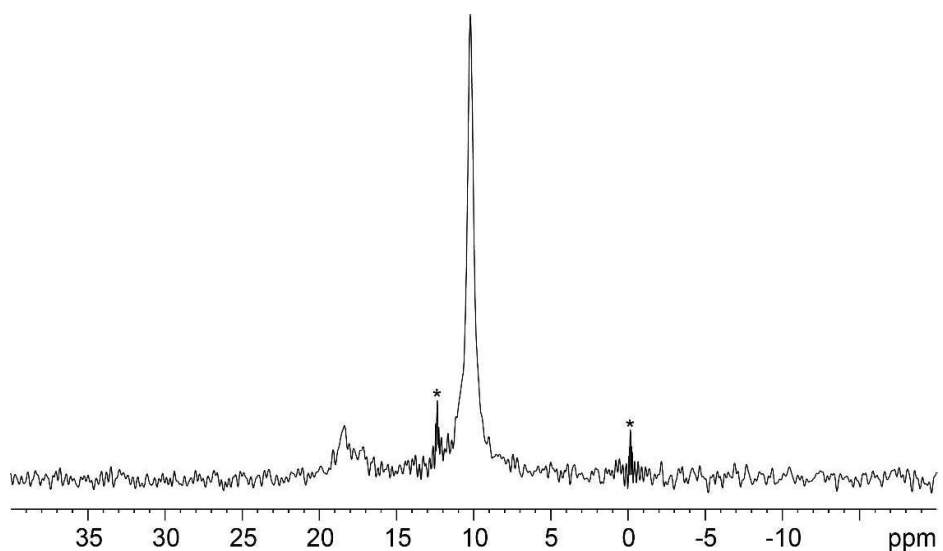
Figure S7. ^{31}P NMR spectrum of DPA-Dex-β-CD. Signals denoted by an asterisk (*) originate from impurities.
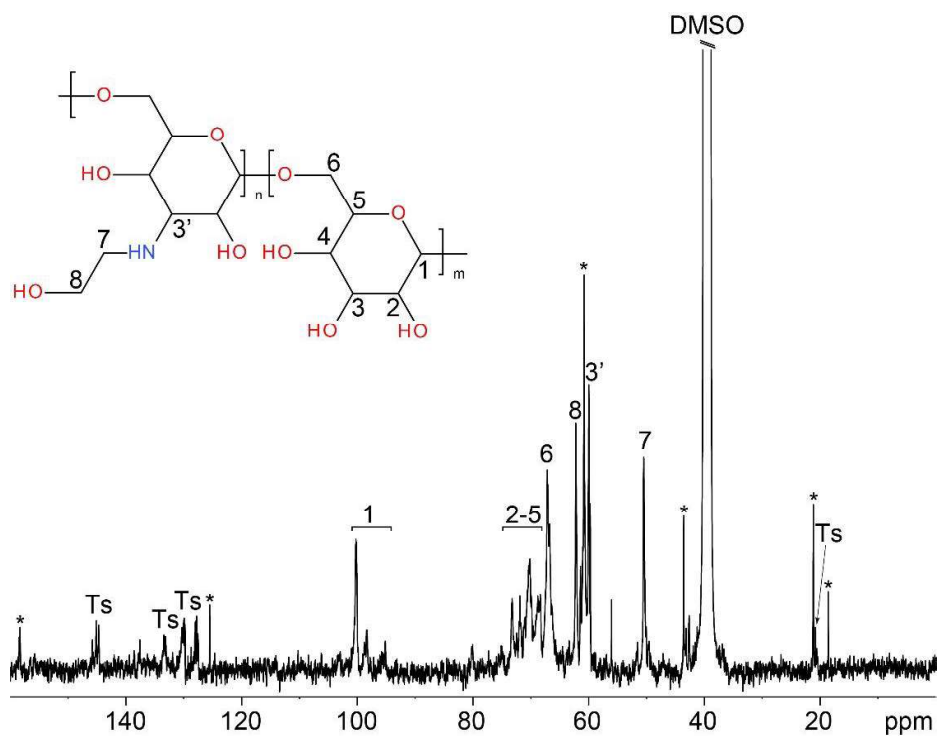

Figure S8. ^{13}C NMR spectrum of Dex-EA. Signals denoted by an asterisk (*) originate from residual solvents used in synthesis or impurities. Signals marked as "Ts" are caused by residual tosyl groups.
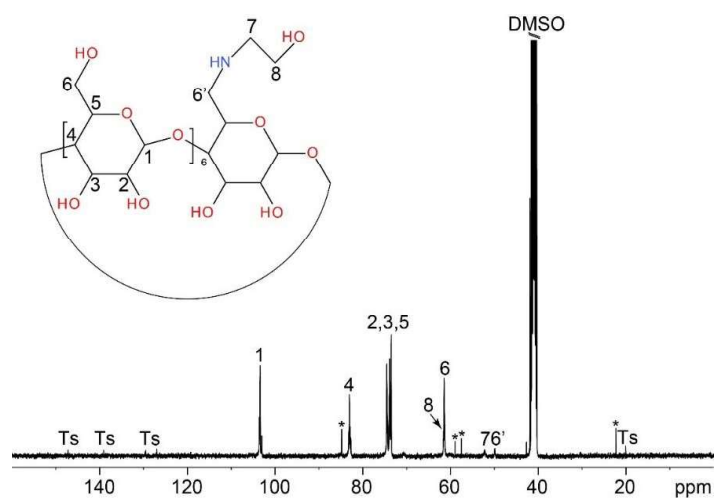
Figure S9. ^{13}C NMR spectrum of CD-EA. Signals denoted by an asterisk (*) originate from residual solvents used in synthesis or impurities. Signals marked as "Ts" are due to residual tosyl groups.